Switched-beam antenna array design for millimeter-wave applications

Switched-beam antenna array design for millimeter-wave applications

Mohadig Widha Rousstia, M.Sc.

Design report on the work carried out at the Eindhoven University of Technology, Eindhoven, The Netherlands, during the period October 2010 – August 2011.

Project Supervisors

dr. ir. M. H. A. J. Herben

A. C. F. Reniers

TU/e

Eindhoven University of Technology (TU/e)

Department of Electrical Engineering

Electromagnetics Group

Stan Ackermans Institute (SAI)

Information and Communication Technology (ICT)

August 2011

Switched-beam antenna array design for millimeter-wave applications

by Mohadig Widha Rousstia, M.Sc.

A catalogue record is available from Eindhoven University of Technology Library

ISBN: 978-90-444-1066-2

(Eindverslagen Stan Ackermans Instituut; 2011/059)

Keywords: rod antenna, polyrod antenna, dielectric antenna, tapered rod, circular rod, dielectric horn, conformal antenna, switched-beam array, multibeam, travelling wave, end-fire, antenna array, scan range, scan beam, 60 GHz antenna, millimeter-wave antenna, gigabit wireless communication, CPW, RF MEMS, MEMS switch, SP3T

Acknowledgements

This project cannot be finished successfully without many helps from people in the Electromagnetics Group at TU/e. First, I would like to express my sincere gratitude to dr. ir. Matti Herben for his numerous guidances and invaluable inputs during this project. His availability for me in daily basis is of a great importance to make this project accomplished successfully. I would like to also thank Ad Reniers for supervising me and sharing his broad experiences with me during conducting this project. Also, I would like to thank especially prof. Dr.-Ing. Leon Kaufmann for giving me the opportunity to work in the Netherlands and, particularly, in this inspiring environment. Special thanks also to prof. dr. ir. Bart Smolders and prof. dr. ir. Erik Fledderus for guiding me to find this interesting project. I am also grateful to have worked with Erwin Dekkers from GTD and Boy van Veghel from QPI, to make the antenna demonstrator realizable.

I want to also thank Imran Kazim for our many discussions, his patience as being my office mate, and his willingness to share the computer resource for my simulation, Rainier van Dommele for offering me helps for the radiation pattern measurement, and dr. Mingda Huang for sharing his knowledge. Obviously, I also thank dr. ir. Rob Mestrom for the useful information about the MEMS. I also highly appreciate the helps from Rian van Gaalen and Suzanne Kuijlaars during my stay and work period at TU/e. I profusely thank Peng Guo, Chrysoula Sismanidou, Mojtaba Zamanifekri, Shady Keyrouz, Ulf Johannsen, David Duque Guerra, and all colleagues, who cannot be mentioned here one by one, for sharing her/his interest in this project and making the Electromagnetics group a vibrant place to work.

Last but not least, I would like to dedicate special thanks for my parents and brother for their unconditional love and support.

Summary

The limited coverage of wireless communication at the millimeter-wave frequency band due to large free-space path loss, i.e. large signal attenuation, has been a major problem. Furthermore, shadowing and small-scale fading may reduce the received signal even more. An array of rod antennas is designed to tackle those problems by providing high gain, broad scan range, and a shaped beam. Each patch, which couples the electromagnetic wave to the rod, is fed by a coplanar waveguide (CPW) feedline. Each rod antenna demonstrates 18 dBi realized gain and 20° half power beamwidth (HPBW). Moreover, the 4 GHz bandwidth of the antenna provides high data rate for the gigabit wireless application. Furthermore, the Radio Frequency Microelectromechanical System (RF MEMS) switch is used to realize a switched antenna with a broad scan range. The design method and the characterization of the antenna are presented. The proposed antenna system is suitable for a wide range of applications, such as wireless high definition video/audio, USB and firewire replacement, Frequency Modulated Continuous Wave (FMCW) radar, and home/office backhaul application at millimeter-wave frequency.

Table of contents

Acknowledgements……i
Summary……ii
Table of contents……iii
List of abbreviations……v
List of figures……viii
List of tables……xii

1 Project description 1
1.1 Introduction of millimeter-wave wireless communication 1
1.2 Challenges in millimeter-wave wireless communication 3
1.3 Overview of the antenna structure 4
1.4 Project objective 6
1.5 System specification 7
1.5.1 Link budget analysis 7
1.5.2 Specification of the antenna structure 10
1.5.3 Specification of the RF MEMS switch 11
1.6 Report outline 12
2 Design of the dielectric rod antenna in the 60-GHz frequency band 15
2.1 Background of the dielectric rod antenna 16
2.1.1 How the rod antenna works 16
2.1.2 Field configuration 22
2.2 Design iteration of the rod antenna 25
2.3 Optimization of the rod antenna 31
2.4 Patch-fed structure 34
2.5 Transmission line structure 36
2.5.1 Coplanar waveguide 36
2.6 Preparation for the simulation 38
2.7 Antenna characterization 40
2.7.1 Array structure with 40° inter-element angular distance θ_{el} 40
2.7.1.1 S-parameter 42
2.7.1.2 Radiation pattern 43
2.7.2 Array structure with 20° inter-element angular distance θ_{el} 45
2.7.2.1 S-parameter 45
2.7.2.2 Radiation pattern 46
2.7.2.3 Polarization 49
2.7.2.4 Radiation efficiency 51
2.8 Comparison of the mutual coupling of different array structures 52
2.9 Design template 54
3 Design of the RF MEMS switch in the 60-GHz frequency band 59
3.1 Background of the RF MEMS switch 60
3.1.1 RF considerations 61
3.1.2 Electromechanical considerations 64
3.2 SP3T switch structure 66
3.3 Transmission line, interconnection, and packaging 71
3.3.1 90° CPW bend 72

3.3.2 Via, tapering, and SMA transition in CPW transmission line 73
3.3.3 λ/4 transmission line 74
3.3.4 Packaging 75
3.4 RF MEMS characterization 75
3.5 Actuation voltage 79
4 Prototype of the switched-beam antenna array 83
4.1 Integration of the antenna and RF MEMS 83
4.2 Sensitivity of the structure 88
5 Fabrication and measurement 91
5.1 Consideration for manufacturing the antenna structure 91
5.2 Characterization of the foam material 93
5.3 Characterization of the RMSW 220HP evaluation board 95
5.3.1 Return loss and insertion loss 95
5.4 Characterization of the conformal rod antenna 96
5.4.1 S-parameter 96
5.4.2 HPBW, far-field pattern, and antenna gain 98
5.5 Characterization of the antenna system 104
5.5.1 Return loss 104
5.5.2 HPBW, far-field pattern, and antenna gain 105
6 Conclusions and future works 107
6.1 Conclusions 107
6.2 Recommendations and future works 108
7 References 111
8 Appendices 119
8.1 Project based management 119
8.1.1 Introduction 119
8.1.2 Problem description 120
8.1.3 Goal and results 120
8.1.4 Delimitation 121
8.1.5 Project phases 122
8.1.6 Capacity and time plan 123
8.1.7 Organization 124
8.1.8 Money 125
8.1.9 Quality 126
8.1.10 Progress control 126
8.1.11 Risk list and risk management 127
8.2 Antenna demonstrator 128
8.3 DC-DC converter for actuating the MEMS 130
8.4 System overview of the 60-GHz wireless communication 132

List of abbreviations

BER	Bit error rate
BW	Bandwidth
CPW	Coplanar Waveguide
CST	Computer Simulation Technology
DC	Direct Current
DEVURO	Detection of Vulnerable Road User
DIMES	Delft Institute of Microsystems and Nanoelectronics
EM	Electromagnetics
ESD	Electrostatic Discharge
FEC	Forward Error Correction
FET	Field Effect Transistor
FGCPW	Finite Ground Coplanar Waveguide
FIT	Finite Integration Technique
FMCW	Frequency Modulated Continuous Wave
GaAs	Galium Arsenide
Gbps	Gigabit per second
GHz	Giga Herzt
GmbH	Gesellschaft mit beschränkter Haftung
GND	Ground
GSG	Ground-Signal-Ground
GTD	Gemeenschappelijke Technische Dienst
HD	High Definition
HE	Hybrid mode
HPBW	Half Power Beamwidth

ISI	Inter Symbol Interference
ISM	Industrial, Scientific, Medical
ITU	International Telecommunication Union
LNA	Low Noise Amplifier
LCP	Liquid Crystal Polymer
LHCP	Left-hand Circular Polarization
LOS	Line-of-sight
LTCC	Low Temperature Co-fired Ceramic
MHz	Megaherzt
MIMO	Multiple-Input and Multiple-Output
MS	Microstrip
MMIC	Monolithic Microwave Integrated Circuit
MWS	Microwave Studio
NF	Noise Figure
NLOS	Non-line-of-sight
OTS	Off-the-shelf
PI	Polyimide
PIN	P-type, Intrinsic, N-Type semiconductors
PML	Perfectly Matched Layer
PS	Polystyrene
PTFE	Polytetrafluoroethylene
QPI	Quality Products International
QPSK	Quadrature Phase Shift Keying
Radar	Radio Detection and Ranging
RF	Radio Frequency
RF MEMS	Radio Frequency Microelectromechanical System

RHCP	Right-hand Circular Polarization
RMI	Radant MEMS, Inc.
Rx	Receiver
SAI-ICT	Stan Ackermans Institute – Information & Communication Technology
SLL	Side Lobe Level
SMA	Sub-Miniature version A
SPNT	Single Pole *N* Throw
SUT	Substrate-under-test
TE	Transverse Electric
TM	Transverse Magnetic
TEM	Transverse Electromagnetic
TRL	Thru-Reflect-Line
TTD	True-time-delay
TU Delft	Delft University of Technology
TU/e	Eindhoven University of Technology
Tx	Transmitter
VNA	Vector Network Analyzer
VRU	Vulnerable Road User
WLAN	Wireless Local Area Network
WSN	Wireless Sensor Network

List of figures

Figure 1.1. Beamwidth and channel distortion [17]. 3
Figure 1.2. Indoor channel measurement at 60 GHz for NLOS [23]. 4
Figure 1.3. Conformal structure of rod antennas. 5
Figure 1.4. RF MEMS position underneath the conformal structure. 6
Figure 2.1. Definition of Cartesian coordinates (*x*-, *y*-,and *z*-coordinate), elevation angle (θ), and azimuthal angle (φ) that is being used throughout this design report. 17
Figure 2.2. Comparison of radiation patterns between the simulation and the approximation formula. 18
Figure 2.3. Ray paths inside (a) the uniform dielectric rod, (b) the tapered dielectric rod, and (c) the tapered dielectric rod with a cylindrical section. 21
Figure 2.4. Electric field (E-field) for the HE_{11} mode in circular dielectric waveguide with diameter $Ø_{rt}$ = 1.64 mm, ε_r = 2.53 at 60 GHz: (a) absolute E-field and (b) E-field lines. 25
Figure 2.5. Array of the dielectric rod antenna. 26
Figure 2.6. S-parameter in the frequency range from 56 to 64 GHz, simulated using the time domain solver with 40° inter-element angular distance (θ_{el}). 27
Figure 2.7. S-parameter in the frequency range from 56 to 64 GHz, simulated using the frequency domain solver with 40° inter-element angular distance (θ_{el}). 28
Figure 2.8. Radiation pattern of the dielectric-rod antenna array: The comparison between PS and Kapton rod antenna. 29
Figure 2.9. Dielectric rod antenna with a waveguide: An optimized rod shape. 30
Figure 2.10. Influence of the launcher in the radiation pattern of the whole antenna structure. 32
Figure 2.11. Comparison of the sidelobe pattern for different cylindrical rod diameters ($Ø_{rt}$) (see Figure 2.18(a)). 33
Figure 2.12. Comparison of the sidelobe pattern for different length ratios (r_{tl}) of the tapered section (h_{tr}) to the overall rod (h_{tr} + h_{cr}) (see Figure 2.18(b)). 34
Figure 2.13. Transition to the rod antenna using an electromagnetically-coupled circular patch antenna. 35
Figure 2.14. Cross-sectional view of a CPW. 36
Figure 2.15. S_{11} and S_{21} of a CPW transmission line at the microwave frequency band. 37
Figure 2.16. Stop criterion of the transient simulation: (a) The field energy decaying over time in the simulation environment and (b) recorded incident and scattered signals over time in several simulation ports. 39
Figure 2.17. Rod antenna array with θ_{el} = 40°. 40
Figure 2.18. Dimension of the single-element rod antenna: (a) bird's-eye view, and (b) cross-sectional view 42
Figure 2.19. S-parameter over the frequency band of the dielectric-rod antenna array with θ_{el} = 40°. 43
Figure 2.20. Radiation pattern of the dielectric-rod antenna array with θ_{el} = 40°. 44
Figure 2.21. Two-dimensional radiation pattern of the rod element. 44
Figure 2.22. Rod antenna array with θ_{el} = 20°. 45
Figure 2.23. S-parameter over the frequency band of the dielectric-rod antenna array with θ_{el} = 20°. 45
Figure 2.24. Radiation pattern of the dielectric-rod antenna array with θ_{el} = 20°. 47
Figure 2.25. Typical realized gain and HPBW of the rod element. 47

Figure 2.26. Snapshots of the electric field at (a) 0.175 ns, (b) 0.275 ns, and (c) 0.35 ns.....49
Figure 2.27. Axial ratio.....50
Figure 2.28. Far-field components for the spherical coordinate system.....50
Figure 2.29. Radiation efficiency and total efficiency of the rod element. 51
Figure 2.30. Mutual coupling S_{21} between neighboring rod elements for different θ_{el}'s: (a) S_{21} magnitude over a frequency band and (b) S_{21} magnitude at 60 GHz. 52
Figure 2.31. Mutual coupling S_{21} between neighboring rod elements for different substrate extensions, d's. This distance, d, is measured from the waveguide edge to the substrate edge of the single-element antenna. (a) S_{21} magnitude over a frequency band and (b) S_{21} magnitude at 60 GHz. 53
Figure 2.32. Reflection coefficient for different heights (h_{cr}) of the cylindrical rod. 54
Figure 2.33. Design template for various heights of the cylindrical PS rod (h_{cr}) (see Figure 2.18(b)): (a) the gain (at $\theta = 0^{\circ}$) for $\varphi = 90^{\circ}$, (b) the half power beamwidth for $\varphi = 90^{\circ}$, (c) the radiation efficiency, and (d) the sidelobe level for $\varphi = 90^{\circ}$ 55
Figure 2.34. General design template for various heights of the cylindrical rod (h_{cr}): (a) the directivity (at $\theta = 0^{\circ}$) for $\varphi = 90^{\circ}$, (b) the half power beamwidth for $\varphi = 90^{\circ}$, and (c) the sidelobe level for $\varphi = 90^{\circ}$. 56
Figure 2.35. Broadband characteristics for various heights of the cylindrical rod (h_{cr} in mm): (a) maximum gain (at $\theta = 0^{\circ}$) for $\varphi = 90^{\circ}$, (b) half power beamwidth for $\varphi = 90^{\circ}$, and (c) sidelobe level for $\varphi = 90^{\circ}$. 58
Figure 3.1. Cross-sectional view of (a) the ohmic-series switch and (b) the capacitive-shunt switch. 61
Figure 3.2. Circuit model of (a) the ohmic-series switch and (b) the capacitive-shunt switch. 61
Figure 3.3. Structure and dimension of (a) the SP3T RF MEMS switch and (b) its detail in the close vicinity of the transmission line. The solid line represents the structure that faces towards the reader, while the dashed line represents the structure that faces away from the reader.....67
Figure 3.4. Structure of the air bridge.....69
Figure 3.5. Beam structure of the RF MEMS on the CPW transmission line. 69
Figure 3.6. Side view of the SP3T. 70
Figure 3.7. Two-port equivalent circuit of the 90° CPW bend. 72
Figure 3.8. Characterization and optimization of the chamfered bend of the FGCPW transmission line. 73
Figure 3.9. Two-port equivalent circuit of the via. P_1 and P_2 are input and output ports, respectively. 73
Figure 3.10. S-parameter over a frequency band of the SP3T RF MEMS: (a) the right-angle arm and (b) the straight arm. 75
Figure 3.11. Simulation snapshots of the SP3T RF MEMS: (a) the straight arm and (b) the right-angle arm. 77
Figure 3.12. (a) Capacitance and (b) inductance of the MEMS beam in up- and down-positions. 78
Figure 3.13. (a) True-time-delay (TTD) characteristic of the RF MEMS switch; and (b) Group delay time of the RF MEMS switch. 79
Figure 3.14. Actuation DC voltage to produce electrostatic force between actuation pads and aluminum beam. 79

Figure 3.15. Results of mechanic and electrostatic simulations: (a) the electrostatic force and its corresponding traction by applying the actuation DC voltage, (b) a deformed aluminum beam touching the signal conductor by, e.g., applying 90 V_{dc} in actuation pads (see Figure 3.14) 80
Figure 4.1. Structure of the integrated antenna and SP3T. 84
Figure 4.2. Bottom view of the integrated antenna and SP3T. 84
Figure 4.3. S-parameter over the frequency band of the integrated antenna and SP3T. The black-colored line is for the case when the MEMS path for the tilted rod is on (while other paths are off), whereas the red-colored line is for the case when the MEMS path for the upright rod is on. 85
Figure 4.4. Radiation pattern of the rod antenna array with SP3T at 60 GHz. 86
Figure 4.5. Radiation pattern of the integrated antenna and SP3T in a frequency range from 58.5 to 61.5 GHz. 87
Figure 4.6. Realized gain and HPBW of the integrated antenna and SP3T in a frequency range from 58.5 to 61.5 GHz. 87
Figure 4.7. Tolerance analysis of the reflection coefficient. The patch radius ($Ø_{cp}/2$) is perturbed with δ_{max} = ±15 µm. The black-colored line is the nominal design. 89
Figure 4.8. Tolerance analysis of the reflection coefficient. The nominal feed position is perturbed with δ_{max} = ±15 µm, and the black-colored line is the nominal design. This feed position is relative to the center of the patch (see Figure 2.13). 89
Figure 5.1. The manufactured dielectric-rod antenna array: (a) 3 rod elements made from Polystyrene and (b) the SMA connector connected to the FGCPW. 92
Figure 5.2. Two microstrip lines (10.06 and 1.94 cm) for characterizing the foam. 93
Figure 5.3. Measured phases over a frequency range in the two-microstrip-line method. 94
Figure 5.4. RMSW 220HP evaluation board. 95
Figure 5.5. Measured return and insertion losses for both (a) the right-angle arm and (b) the straight arm. S_{11}, S_{22}, and S_{33} are return losses and S_{13}, S_{31}, S_{12}, and S_{21} are insertion losses (see Figure 5.4). 96
Figure 5.6. Comparison between the simulation and measurement for both (a) return loss S_{11} and (b) mutual coupling S_{21}. TRL-calibrated S_{11} is also given in figure (a). 97
Figure 5.7. (left to right) Line, open, and thru configurations for the TRL calibration of the transitions. 98
Figure 5.8. Measurement result of the received power for the gain measurement. 99
Figure 5.9. Measured radiation pattern of the conformal dielectric-rod antenna array. Simulation results are also given for the comparison. 100
Figure 5.10. Measured radiation pattern for different frequencies (a) from 10 to 11.2 GHz and (b) from 11.2 to 12.4 GHz. 101
Figure 5.11. (a) Comparison of the co-polarized radiation pattern between the simulation and measurement, and (b) comparison of the cross-polarized radiation pattern between the simulation and measurement for $\varphi = 90^{\circ}$ and $\varphi = 0^{\circ}$. The measured E-plane for $\varphi = 90^{\circ}$ is also included for the comparison. 102
Figure 5.12. Sidelobe comparison for different measurement distances. 103
Figure 5.13. Comparison of the normalized radiation pattern for different rod materials (i.e. different ε_r). 103
Figure 5.14. (a) Measurement setup for the switched-beam operation, and (b) radiation pattern measurement in the anechoic chamber. 104

Figure 5.15. Measured return loss for the combined rod antenna array and RF MEMS switch (RMSW 220 HP).....105
Figure 5.16. Measured radiation pattern for the combined rod antenna array and MEMS switch. The magnitude of the realized gain is also given for different frequencies. 106
Figure 8.1. Project organization.....124
Figure 8.2. Structure of the 11-GHz antenna demonstrator.....128
Figure 8.3. Surface current of the transition using the SMA connector 129
Figure 8.4. Design template for various heights of the cylindrical rod (h_{cr}) in the frequency range from 9.5 to 12 GHz: (a) the realized gain (at $\theta = 0^{\circ}$) for $\varphi = 90^{\circ}$, (b) the half power beamwidth for $\varphi = 90^{\circ}$, (c) the radiation efficiency, and (d) the sidelobe level for $\varphi = 90^{\circ}$. The rod height in figures is h_{cr} for the antenna demonstrator (f_o = 11 GHz).....129
Figure 8.5. Bird's-eye view of the SP3T. 130
Figure 8.6. (a) Schematic of the MAX774 DC-to-DC converter, and (b) the list of its components. 131
Figure 8.7. MAX774 DC-to-DC converter (the right board) used in the measurement setup for actuating the MEMS switch (the left board). 132
Figure 8.8. Antenna and RF MEMS switch along with the RF front-end system.....132

List of tables

Table 1.1. Link budget analysis for typical millimeter-wave communication system, i.e. 60 GHz. (a) the signal part, (b) the noise part, and (c) the SNR part. 7
Table 1.2. Available margin for different user data bandwidths and Tx antenna gains. 9
Table 1.3. Specification of the antenna structure. 10
Table 1.4. Specification of the RF MEMS switch design. 12
Table 1.5. Requirement of the RF MEMS switch design. 12
Table 2.1. Properties of investigated materials at 60 GHz. 26
Table 2.2. Antenna performances for different cylindrical rod diameters ($Ø_{rt}$) (see Figure 2.11). 33
Table 2.3. Gain performance for different length ratios (r_{tl}) (see Figure 2.12). 34
Table 2.4. Sources of simulation error and inaccuracy. 38
Table 3.1. Material parameters for the high-frequency problem at 60 GHz. 71
Table 3.2. Material parameters for electrostatic and mechanic problems 71
Table 3.3. Insertion loss of the chamfered bend in Figure 3.8. 72
Table 3.4. Comparison of RF MEMS switches: 11-GHz OTS product vs 60-GHz design. 76
Table 8.1. Time plan: DEVURO project – Switched-beam antenna array design for millimeter-wave applications 123
Table 8.2. Gantt chart for project phases and involved capacity. 123
Table 8.3. Possible risks and their priorities. 127
Table 8.4. Risk management plan. 127
Table 8.5. Power loss coefficient values, *N*, for the ITU site-general indoor propagation model. 133

CHAPTER 1

1 Project description

1.1 Introduction of millimeter-wave wireless communication

In recent years, the demand for high data rate telecommunication has been increasing faster than ever. The Industrial, Scientific, Medical (ISM) application band at 2.4 GHz has been overcrowded by numerous and various commercial products of end users, among others, WLAN, Bluetooth, and Wireless Sensor Network (WSN). The use of wireless communication has also rapidly increased, much faster than its wireline counterpart. As a result, the required bandwidth doubles every 18 months [1]. Moreover, the number of owned wireless devices per user has been ever increasing. Not only will the wireless devices connect people to people, but also people to machines and machines to machines. Thus, the limited bandwidth around 2.4 GHz (ISM-band) cannot support the higher data rate if the band has to be shared among many potential users. The availability of 7 GHz around 60 GHz (ISM-band) is able to accommodate high data rate communication. Furthermore, the propagation condition in the 60-GHz wireless channel enables frequency reuse. This frequency reuse is mainly enabled due to the large amount of path losses experienced by the propagating electromagnetic waves. Therefore, the electromagnetic wave does not interfere with other waves generated by the neighboring 60-GHz wireless systems. However, this interesting property comes not only with this advantage. In this frequency band, the wave is highly

attenuated so that the front-end devices of the receiver end have to be very sensitive, otherwise the wave will be effectively undetected. This situation thus limits the communication distance or range of 60-GHz and other millimeter-wave applications.

More applications emerge in the automotive area in this millimeter-wave frequency band. It is expected that the detection of vulnerable road users in the blind spot of a car will incorporate a large number of 76-GHz wireless device [25]. The 76-GHz band is able to facilitate this, mainly due to the feature of the frequency reuse and the large available bandwidth. The use of the millimeter-wave frequency is also preferable for radar applications due to its better resolution.

The highly sensitive front-end device is a necessary requirement for 60-GHz systems or devices. This requirement demands the advancement of the front-end devices and a more sophisticated antenna design. In the design, the cost factor has to be taken into account since this typical device has to be cheap to be ubiquitous. Therefore, high quality front-end devices, including the antenna, with low production cost are preferred. The advent of the supporting high-end technology for 60-GHz applications has to enable the realization of that product in the competitive market.

The significant role of the antenna development has to be considered carefully and extensively since the antenna is a very important part of the wireless system. The major problem in an antenna design in this frequency band is the required high gain needed to compensate for the high path loss. The planar antenna array, realized on a thermoplastic polymer substrate, has been proposed [2]. However, such an antenna is costly due to the need for a large area substrate to achieve the high antenna gain. Thus, large space is highly necessary here. High yield problem for the manufacturing with large substrate area can lead to high cost to produce and commercialize this antenna array. The low cost antenna, using rod configuration made from dielectric material for millimeter wave applications, was first proposed in [3]. To improve the scan range and to enable the efficient switched-beam capability, [4] proposed the enhanced version of [3]. The detailed configuration of the antenna can be found in [5] and [6], though the waveguide configuration is too bulky there. Therefore, the patch-fed method is the plausible approach [7].

The present report mainly addresses and outlines the possible design and improvement for antennas in the 60-GHz band. The antenna's realized gain of 18 dBi is reported in all directions of beam scanning and is low cost to manufacture. The Half Power Beamwidth (HPBW) is approximately 20°. The antenna's scan range of up to 100° and 180° is achievable with 5 and 9 antenna elements, respectively. Since the antenna dimension is also less than 5 centimeters in axial direction, it is suitable to be placed in a car radar system or as a conformal access point in an indoor gigabit communication system. The radome is incorporated to protect the antenna from the environment, such as rain drops, dust, and mud, and to improve the antenna's mechanical strength.

The antenna's switch is realized in RF MEMS which has a prospect to replace the current switching mechanism using PIN diode and FET switches. This is mainly because of

the high linearity and low insertion loss of the RF MEMS device. The design of the antenna system, with the RF MEMS, has been optimized by computer simulations using CST MWS™. Furthermore, the optimized antenna design has been verified by the measurement of the antenna demonstrator. This antenna and RF MEMS design is suitable for the millimeter-wave frequency range due to its high performance and small dimensions at this high frequency. Some applications are: wireless high definition video/audio, USB and firewire replacement, Frequency Modulated Continuous Wave (FMCW) radar, and home/office backhaul application at millimeter-wave frequency [24].

1.2 Challenges in millimeter-wave wireless communication

In addition to some challenges mentioned in section 1.1, some problems that even more degrade the quality of the received signal at the receiver will be discussed here. In other words, while the attenuation is from blockage and free-space path loss, some other causes of the problem also exist. Clearly, severe attenuation requires high gain of antenna and RF front-end system.

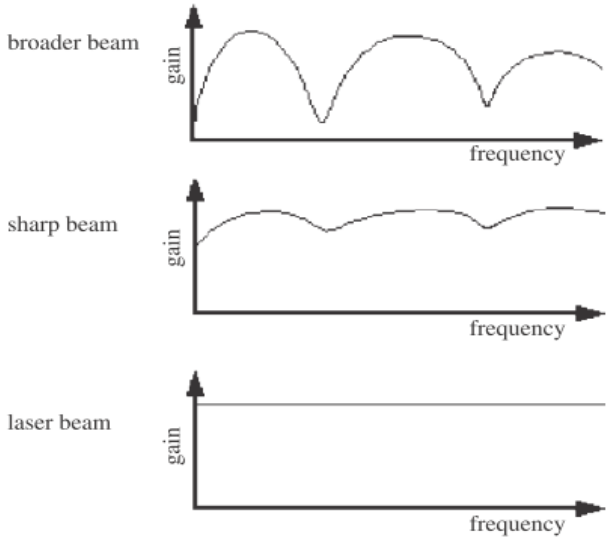

Figure 1.1. Beamwidth and channel distortion [17].

Figure 1.1 shows the multipaths in an indoor environment, e.g. an office. The notch width is due to the delay spreads; its depth is due to the difference in path gain (or loss). The notches' width is influenced by the size of the multipath environment in this case an office room. This multipath can cause inter symbol interference (ISI).This ISI may increase the bit error rate (BER) in the signal detection. To reduce the number and amplitude of multipath waves, a narrow-beam antenna is preferred. The narrower the beam is, the less the multipaths

occur. This means also that no equalizer is needed at the receiver. This results in less cost for the receiver digital part and more synchronized video data due to the absence of delay that would have been introduced by the equalizer.

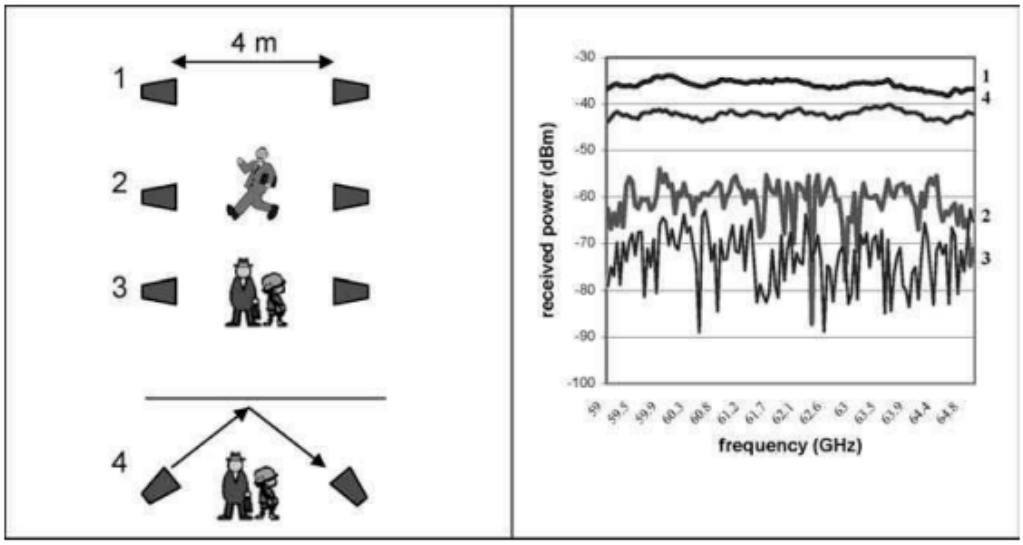

Figure 1.2. Indoor channel measurement at 60 GHz for NLOS [23].

Figure 1.2 illustrates the shadowing caused by obscuring objects in this case humans. Case 1 shows the line of sight (LOS) scenario. Case 2 and 3 shows one and two humans standing between two antennas, respectively. Case 4 shows a non-LOS (NLOS) wireless link. The corresponding received power is shown in the picture at the right side. Obviously, the obscuring objects can reduce the amount of the available received power, particularly at this millimeter-wave band. In other words, a LOS communication is easily blocked. To cope with this problem, the switched-beam conformal antenna is proposed. Moreover for such conformal structure, every antenna element can have less signal correlation to each other due to its spacing and its angular diversity. A multiple-input multiple output (MIMO) system can also use this antenna structure, to increase the overall capacity of the communication system.

1.3 Overview of the antenna structure

The increase in popularity of the dielectric rod with circular cross section is because of its wide bandwidth, shape, ability to create a symmetric radiation pattern, low polarization cross coupling, ease of fabrication, and low cost [14][78][40]. The rod antenna can be integrated directly to the monolithic microwave (MMIC) and millimeter-wave integrated circuits. It can be also used as an high efficiency feed system for reflector antennas at low frequencies [13]. Moreover in active and passive imaging application at millimeter-wave frequency, the rod antenna can provide good illumination for the lens or reflector in focal plane arrays and can be densely packed, what the feed horn antenna cannot meet [15].

In this design, the rod antenna is chosen because of its high performance as mentioned earlier. Also, with careful design, the rod antenna can provide high gain that is suitable for millimeter-wave applications. Compared to its counterpart, namely the horn antenna, the rod antenna is simpler to design and is not too bulky, which is suitable for integration with the MMIC. It has a small cross-sectional dimension which can fit to a lateral planar structure, and is flexible by designing it conformal.

The novelty of the present design is its conformal structure as shown in Figure 1.3 and the optimized tapered rod structure which can support millimeter-wave application effectively. With the careful choice of the rod structure, the high gain and controlled radiation pattern can be obtained. The dielectric material shown as green color in the figure is polystyrene (PS), which has 0.0008 and 0.00094 loss tangent (δ) at 11 GHz and 60 GHz, respectively. The yellow-colored metallic waveguide in the figure is made from brass. This waveguide which acts as horn launcher here can reduce the sidelobe level (SLL). The planar structure below it is made from liquid crystal polymer (LCP) which has 0.0045 loss tangent (δ) at 60 GHz [60] [61].

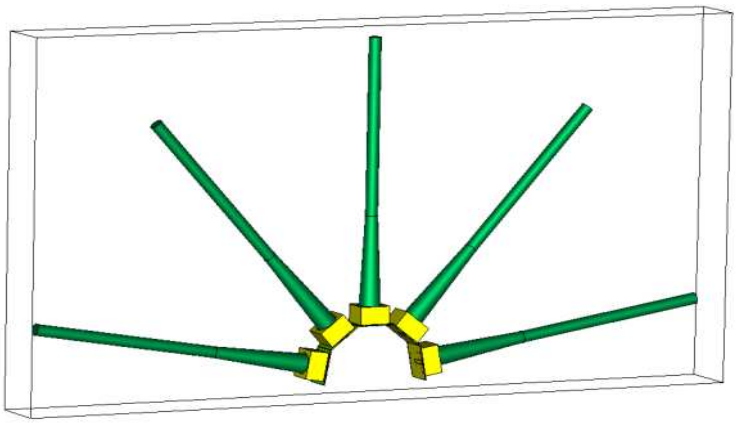

Figure 1.3. Conformal structure of rod antennas.

In Figure 1.4, the blue-colored RF MEMS chip which acts as switch in the design is also shown. It is positioned underneath the planar substrate. As a result, no via is needed to connect the signal path to the upper part of the planar structure. In this way, the matching condition does not degrade. However, a bond pad is needed here to attach the RF MEMS to the planar substrate. The solder ball is generally much thinner than the LCP dielectric thickness. The RF MEMS substrate is made of sapphire. Sapphire is gas-air-impermeable (preventing gas and liquid diffusion) and has very high strength (even at temperature near 2000° C) [57]. The RF MEMS will then be packaged using sapphire material as well, though it is not shown here for the sake of clearness. Since here the signal path is connected to the solder ball by a very thin via to the back part of the sapphire, no connection from the upper plane RF MEMS to the out world is needed. Thereby, the package can be attached tightly to the sapphire surface. This condition can prevent the gaseous contaminants from residing

inside the packaging that can reduce the beam performance and the lifetime. More detailed discussion of the antenna and the RF MEMS structure will be given in the next chapters.

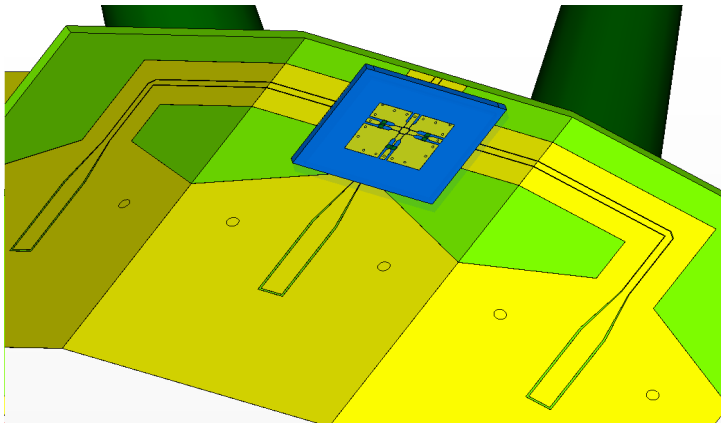

Figure 1.4. RF MEMS position underneath the conformal structure.

1.4 Project objective

The project objective is to design an antenna system for millimeter-wave applications. That antenna has to have high gain and broad scan range and low cost of production. To support a very broad scan range with constant performance, a novel conformal structure of the rod antenna is designed in this project. This antenna system will be integrated to MMIC front-end system. Moreover, it can be applied for various applications in the millimeter-wave frequency band, e.g. 24- and 76-GHz radar applications, 60-GHz indoor communication, and radiometry application. Also, a novel 60-GHz SP3T RF MEMS switch has been designed. A fabrication of this MEMS will take a long technology flow and time. Hence, in this project, the MEMS design is finalized through the working simulation, with considerations for the fabrication process.

For this project, the demonstrator of the rod antenna is then prepared for 11-GHz operating frequency, because of the commercial availability of the RF MEMS switch at that frequency and the availability of the measurement equipment at TU/e at the time this project is performed. In addition, the size of the antenna demonstrator has to be accounted as well. However, the design of the antenna and the RF MEMS has been completed successfully at 60 GHz. For the antenna structure, its dimensions are inversely proportional to its operation frequency. Thereby, for a higher operation frequency, the antenna dimension is proportionally smaller.

1.5 System specification

The system specification is the most important part in the design of a communication system. The wave propagation in the millimeter-wave frequency band faces very challenging problems; the electromagnetic wave cannot propagate for a long distance because of the high path loss due to a.o. blockage. To investigate this from a system point of view, first a link budget analysis will be performed. Subsequently, the specification and requirement of the antenna and the RF MEMS switch design will be discussed. The cost for manufacturing the structures will also be discussed in section 8.1 in the Appendices, since the low cost requirement for consumer product applications is indispensable.

1.5.1 Link budget analysis

To find the limitation in the design of the front-end parts including the antenna, a link budget analysis is performed in Table 1.1. From this analysis, the antenna gain requirement can be specified for a particular application and for the planned frequency band. In this case, 60-GHz wireless communication is taken as a representative example of millimeter-wave applications. The communication distance, *d*, of 10 meters is chosen here as the worst case scenario for the 60-GHz indoor application. The bandwidth of 4 GHz is chosen to see the limitation.

Assumed that 1 W power is available in each 60 GHz transceiver terminal. However, the allowed EIRP is limited due to the regulation in which the peak EIRP is around 43 dBm for Europe region [52]. For the antenna gain of 18 dB, the transmitted power P_t is now 316 mW. This is because in terms of dBm, it results in:

Table 1.1. Link budget analysis for typical millimeter-wave communication system, i.e. 60 GHz. (a) the signal part, (b) the noise part, and (c) the SNR part.

(a) The signal part.

Parameter	Maximum value	Total sum	Description
Tx power	25 dBm	25 dBm	According to equation (1.1)
Tx antenna gain	18 dBi	43 dBm	**Proposed high-gain rod antenna**
Path loss	-90 dB	-47 dBm	According to equation (1.2)
Rx antena gain	0 dBi	S = -47 dBm	Omnidirectional antenna of user terminal

(b) The noise part.

Parameter	Maximum value	Total sum	Description
Background noise	-174 dBm/Hz	-174 dBm/Hz	According to equation (1.4)
Noise BW (e.g. 4 GHz)	96 dB	-78 dBm	4 GHz user data BW, ¾ code rate of FEC, and ¾ RF bandwidth of shaped QPSK (see equation (1.5))
Noise figure of Rx	19 dB	N = -59 dBm	Typical NF for RF front-end system

(c) The SNR part.

Parameter		Total sum	Description
SNR output		S - N = -47-(-59) = 12 dB	
Required SNR		10 dB for QPSK	For BER 10^{-5} with QPSK
Margin		**4 dB**	

$$P_t(dBm) = 10\log\left(\frac{316mW}{1mW}\right) = 25\ dBm, \tag{1.1}$$

where the sum of the transmitted power and the antenna gain is 43 dBm. However, for other regions, the allowed EIRP can be found in [52].

The total path mean loss in the office indoor environment according to the ITU formula is given by:

$$L_{total} = 20\log_{10}(f) + N\log_{10}(d) + Lf(n) - 27.54\ dB, \tag{1.2}$$

where f is frequency in MHz, d distance in meters, N power loss coefficeint, and $Lf(n)$ floor penetration loss factor, which is not taken into account for communication in the same room. The value of 27.54 dB in equation (1.2) comes from:

$$20\log(c) - 20\log(4\pi) = 49.54\ dB - 22\ dB = 27.54\ dB,$$

where c is the speed of light in vacuum (= 3 x 10^8 m/s). Hence from equation (1.2),

$$\begin{aligned} L_{dB} &= 20 * \log(f[MHz]) + N * \log(d) - 27.54 \\ &= 20 * \log(60 * 10^3[MHz]) + 22 * \log(10) - 27.54\, dB \\ &= 90.02\, dB. \end{aligned} \quad (1.3)$$

Coefficients *N* for the path loss calculation are presented in the Table 8.5 in the Appendices. For 60 GHz indoor office environment in the same room, *N* = 22. The background noise (see in Table 1.1(b)) is defined as follows:

$$10 \log_{10}(kT), \quad (1.4)$$

where *k* is Boltzman constant = 1.37 x 10-23 Watt -s/Kelvin = -198.6 dBm –s/Kelvin; and T = room temperature = 290 Kelvin.

The modulation is specified as it has a constant envelope to lessen the requirement to meet the linearity in the RF front-end circuit. Also, it is simple to demodulate, so the digital part could be realized with a cheaper design. Furthermore, the system utilizes a forward error correcting mechanism FEC with ¾ code rate. This is the reason for 5.33(3) Gbps specification as a gross amount of data that need to be sent through the radio channel. The bandwidth for the signal has to take into consideration the additional bits needed for the error correction. With shaped QPSK modulation, the bandwidth of one channel is thus:

$$\text{BW} = 5.33(3)\ \text{Gbps} * 0.75 = 4\ \text{GHz}. \quad (1.5)$$

The noise figure (*NF*) in Table 1.1 (b) is a typical value in RF front-end devices, including low noise amplifier (LNA), mixer, and filters. However, NF is not restricted to that value for some applications. The antenna system with its neighboring RF front-end system can be found in Figure 8.8 in the Appendices.

Table 1.2 summarizes various conditions and corresponding available margins for the system. The other parameters are fixed to values as shown in Table 1.1. It can be observed for 1-GHz data rate that 18-dBi gain of the proposed rod antenna can have an 8-dB margin. This is to anticipate the slow fading due to blockage and the fast fading due to multipath propagation.

Table 1.2. Available margin for different user data bandwidths and Tx antenna gains.

Tx antenna gain (dBi)	**Available margin (dB)**	
	User data bandwidth 4 GHz	**User data bandwidth 1 GHz**
12	-4	2
15	-1	5
18	2	8

Furthermore, a margin of two times the standard deviation (Ω) of the spread in the shadowing component corresponds to 98 % availability [52]. The parameterization of the generic 60-GHz path-loss model for both indoor and office environments are already presented in [53]. Thereby, this 8-dB antenna margin can support 98% availability in LOS condition for both generic indoor and office environments (Ω = 1.8 dB) for up to 2-GHz data rate. Note that this is for the worst-case scenario where the communication distance (*d*) is 10 m. For $d \sim 6$ m, this antenna can support the same availability in NLOS condition of those environments (Ω = 4.6 (indoor) and 5.1 (office)) for the same data rate. In addition, the gain of the receiver's antenna can also be added to improve the probability of the successful connection and to extend the communication distance.

1.5.2 Specification of the antenna structure

As has been mentioned in section 1.2, an obscuring object, e.g. human, can severely block the communication channel especially for the radiation with a narrow beamwidth. Furthermore, for a typical indoor environment where there are multipaths, an antenna that can minimize the destructive effect of this channel condition will be beneficial. Therefore in Table 1.3, the gain and the HPBW of the antenna are specified. Also, other necessary parameters have to be fulfilled to have an antenna working efficiently.

Table 1.3. Specification of the antenna structure.

Parameters	Specification
Operation frequency	60 GHz
-10 dB impedance bandwidth	> 1 GHz
Input impedance	~ 50 Ω
Realized gain	18 dBi
Radiation efficiency	> 70 %
HPBW	~ 20°
SLL	< -10 dB
Mutual coupling	~ -30 dB
Polarization	Linear vertical polarization
System demands	Low cost, conformal structure, relatively small, repeatability

The operation frequency of the antenna in the millimeter wave frequency band is chosen to be 60 GHz. Typical multi-gigabit applications at 60 GHz require a large bandwidth, > 1 GHz, for an high-speed communication. This bandwidth is planned and allocated for full-duplex operation of both Tx and Rx. The input impedance is 50 Ω. The radiation efficiency has to be sufficiently large to have an high antenna gain. The antenna with a small HPBW can minimize ISI and also give a large gain. This HPBW also determines the number of array element so that the antenna array can have a broad scan range with a believable number of elements. SLL < -10 dB is sufficient for a directive antenna. Finally, a good port-to-port isolation (i.e. sufficiently low mutual coupling) is necessary for a switched-beam antenna.

1.5.3 Specification of the RF MEMS switch

The RF MEMS switch as a part of the antenna system has to have good performances otherwise the antenna performance will be limited by the RF MEMS switch. A careful design has to be performed especially for the insertion loss, bandwidth, and the port isolation of the switch. For example, if an antenna has a high gain while its switch has a high insertion loss, this loss will cancel out that antenna gain. The RF MEMS here is to perform its task as a switch, and it shall have a low loss. Table 1.4 shows important parameters that have to be specified for designing that RF MEMS switch. Table 1.5 shows typical requirements for an efficient and reliable RF MEMS switch.

The operation frequency of the switch has to support the operation frequency of the antenna, and this switch has to be able to support a broadband operation frequency, so the antenna performance will not be limited by the switch performance. Moreover, the switch with bandwidth > 4 GHz allows its use for various millimeter-wave applications. The insertion loss < 1.5 dB is sufficient for a working switch with its packaging and interconnection. The RF MEMS is a mechanical device whose its linearity performance is better in comparison to its counterpart diodes. This means that it can reduce the inter-modulation caused by high power transmission. Finally, the isolation performance of the switch should not limit the isolation performance of the antenna. The isolation by its definition should be a large value e.g. 30 dB instead of -30 dB. However, due to its common use (i.e. -30 dB), it is explicitly explained here to avoid confusion. Similarly, the insertion loss by its definition should be 1.5 dB instead of -1.5 dB. However, if it is mentioned as -1.5 dB, it should be still clear for the reader.

The typical switching time of the RF MEMS switch is in the order of µs. However, this has to be low enough to compete with its counterpart, i.e. diodes and FET. Having its low-power consumption is one of advantages of the RF MEMS switch. The mentioned value is the typical power consumption per actuation [26]. Also, the typical reliability of the RF MEMS structure is as in [26]. Apart from the switching time, the reliability (switching cycle) can only be measured from a manufactured product in a specialized measurement environment.

Table 1.4. Specification of the RF MEMS switch design**.**

Parameters	Specification
Operation frequency	60 GHz
-10 dB impedance bandwidth	> 4 GHz
Insertion loss	< 1.5 dB
Isolation	~ -30 dB
Linearity	30 dB better than PIN diode or FET switches
System demands	Low cost, repeatability

Table 1.5. Requirement of the RF MEMS switch design.

Parameters	Requirement
Switching time	< 40 µs
Reliability	0.1-10 billion cycles
Power consumption	10-100 nJ per cycle

1.6 Report outline

Chapter 2 presents the design aspects of the rod antenna. The physics and the working principle of the rod antenna will be explained. Also, the influence of the antenna's dimension and material to the antenna performance will be carefully discussed here. The design flow is used to find the optimized antenna structure. Antenna characterizations from the simulation are described here for different array structures. The design template for the antenna pattern is also depicted graphically. Some related design aspects for such a structure will be included.

Chapter 3 aims mainly at designing the RF MEMS switch for millimeter-wave applications. The packaging technique and the mechanical and electrostatic parts will be discussed. The characterization of the structure will be shown by performing computer simulations. Eventually, the integrated prototype of the antenna and the RF MEMS switch is presented in Chapter 4. This chapter also deals with the manufacturing tolerance.

Chapter 5 will explain the problem concerning the fabrication of the antenna structure. The antenna demonstrator is characterized by measurements and compared with the simulated results. Chapter 6 provides the conclusions, recommendations, and future works. The references and Appendices are in Chapter 7 and 8, respectively.

CHAPTER 2

2 Design of the dielectric rod antenna in the 60-GHz frequency band

The rod antenna is designed here because of its high performance as discussed in Chapter 1. This antenna has high gain which can be very advantageous for the propagation condition with very significant path loss. The low sidelobe level of the radiation pattern is another important feature of the rod antenna. In this way, the antenna will not radiate a significant amount of power in the direction other than the main lobe, and reciprocally, the antenna will not intercept propagating waves in, e.g. free space, in the direction other than the main lobe. This also means that the antenna has a good angular selectivity over the space. In addition to that, the typical radiation pattern produced by the rod antenna is symmetric (i.e. nearly the same 3 dB beamwidth in E- and H-plane).

In the following section of this chapter, the background of the dielectric rod antenna will be discussed. Subsequently, the design steps will be explained and supplemented with the performance characterization of that designed antenna. Moreover, the design iteration, the design template, and the sensitivity of such antenna structure to manufacturing tolerances are also included. The discussion on the sensitivity in this chapter will complement a similar discussion in Chapter 4.

2.1 Background of the dielectric rod antenna

The rod antenna can have a circular, square and rectangular cross section. The cross-section's dimensions depend on the cut-off frequency for which the antenna is intended. The length of the rod usually determines the gain and the radiation pattern of the antenna. The rod itself can be solid dielectric or air-filled. The latter one uses the dielectric sleeve as a mean for wave-guiding. The solid dielectric rod can be made inhomogeneous to meet certain wave or ray guiding characteristics, e.g. supporting several dominant modes. The two-layer dielectric rod antenna has been reported to have broad bandwidth operation and good polarization purity [47][48]. In this two-layer case, the high frequency components are guided inside the inner layer while the low frequency components are guided through the outer layer. However, the drawback for this rod type is its low gain [40].

Some applications using this dielectric rod antenna have been mentioned in section 1.1 and 1.3. Also quite recently, the rod antenna has been successfully reported to be a feeder for a reflectarray [79]. Moreover, the tapered rod antenna can efficiently feed the Cassegrain antenna in [81]. The rod antenna as a feeder necessitates the determination of its phase center. Some previous works in [21], [72], and [74] discuss about the phase center in detail. For terahertz applications, the feasibility of the rod antenna has been reported in [78] and [80]. To build the rod structure that fits the dimension requirement at this frequency band, a laser ablation technique can be utilized.

A high gain antenna can actually be realized by means of a patch array. Nonetheless, this patch array suffers from very high conductor losses arising from high current densities at the strip edge of its feeding network. This antenna however has advantages such as lightweight, compact, and low-profile. To foster those conditions, the dielectric rod antenna is one of the alternative structures, due to its high gain and small size. These conditions can then be exploited to meet the requirement for building e.g. a radiometer system in the millimeter-wave band [75].

2.1.1 How the rod antenna works

The working principle of the dielectric rod antenna uses the fact that the wave-guiding action in a dielectric rod is imperfect. In this way, a considerable amount of power may escape the wall of the rod and be radiated [7]. This rod antenna acts as an end-fire antenna where the main lobe of the radiation pattern is in the direction of the rod's height or *z*-axis as shown in Figure 2.1.

Note that, the coordinate system and angular orientation shown in Figure 2.1 will be used throughout this design report. Furthermore, the position of the feeding point is explicitly observable.

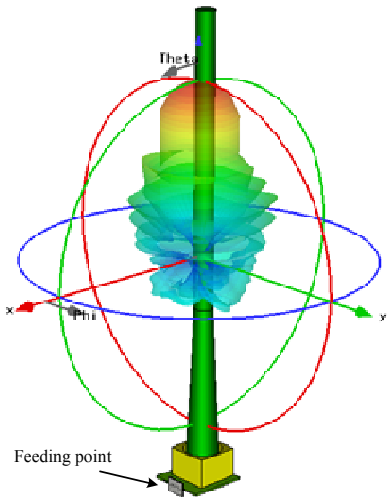

Figure 2.1. Definition of Cartesian coordinates (*x*-, *y*-,and *z*-coordinate), elevation angle (θ), and azimuthal angle (φ) that is being used throughout this design report.

The rod can be regarded as consisting of isotropic point sources along the rod's height. These point sources are excited uniformly in amplitude and it is assumed that a phase shift of:

$$360\left(1+\frac{1}{2L_\lambda}\right)\text{deg/wavelength} \tag{2.1}$$

exists along the rod's height. L_λ is the length of the rod divided by the wavelength. These point sources are regarded as a continuous array. The field pattern as a function of the angle θ from the axis is expressed as follows [7] [17]:

$$E(\theta)=\frac{\sin(\psi'/2)}{\psi'/2}, \tag{2.2}$$

where

$$\psi'=2\pi L_\lambda cos\theta-2\pi L_\lambda\left(1+\frac{1}{2L_\lambda})\right)=2\pi\left[L_\lambda(cos\theta-1)-\frac{1}{2}\right]. \tag{2.3}$$

Equation (2.2) is a sinc function with an argument given by equation (2.3) that expresses the phase-shift factor as shown in equation (2.1). This analytical approximation (i.e. dimension approximation) shows that at θ = 0, the pattern exhibits a maximum magnitude, and that with increasing θ the pattern gradually reduces with maxima and minima, i.e. due to the cos θ. This occurs for both E-plane pattern and H-plane pattern.

It is clear from equation (2.3) that with larger L_λ, the sinc function will reach the nearly zero magnitude faster. This discussion is important in the design of the rod antenna to have fast decaying sidelobes as θ increases. Also, it is observed that the number of maxima and minima will increase as L_λ increases.

Figure 2.2 plots this analytical approximation and compares it with numerical simulation results. The simulation for this design project has been done using Computer

Simulation Technology (CST) Microwave Studio™ (MWS). This is a full-wave EM simulator [51]. The analytical approximation shows a slow-decaying sidelobe until it reaches -12.5 dB side-lobe suppression level at θ = 90°. There are a large number of maxima and minima in this field pattern. This is owing to the many constructive and destructive additions of the waves or rays, as the formula approximates the rod with a linear array of isotropic point sources, i.e. the diameter of the rod is assumed to be zero. Therefore, there is no guiding effect for the waves in this analytical approximation. Note that throughout this report the term ray and wave are used interchangeably. The term 'ray' is usually used in geometrical optics, while the term 'wave' per se is a general term in physics. The ray indicates the propagation trajectory of the wave.

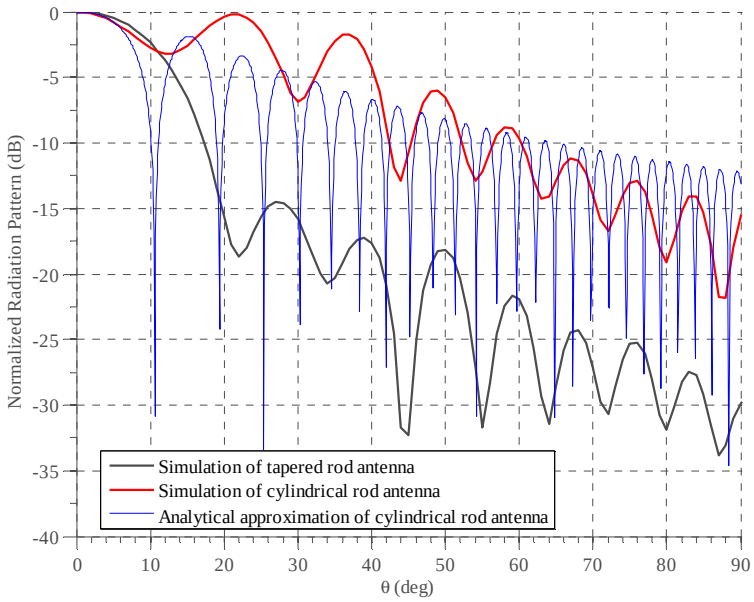

Figure 2.2. Comparison of radiation patterns between the simulation and the approximation formula.

The simulation results of the uniform cylindrical rod antenna clearly differ from the case when the rod's diameter is zero. There are less sidelobes and the first sidelobe level (SLL) is higher. This is caused by the fact that the diameter of the rod at the far-end (top) is the same as at its base. At the far-end rod surface, rays that are refracted or radiated at θ = 22° have nearly as significant power as rays that radiate at θ = 0°. To tackle this large SLL, the tapered rod antenna's pattern is shown as black-colored curve. The tapered rod is the rod with a gradually reducing diameter with its increased length. The half power beamwidth (HPBW) is slightly larger here since most of early refracted rays (i.e. due to the tapered section of the rod) also contribute constructively to ray that are at θ = 0° direction, whereas a gradually smaller fraction of early refracted rays contribute to pattern at θ > 0°.

The dielectric antenna is often referred to as a slow-wave antenna or a travelling surface-wave antenna. Therefore, the rod antenna whose guiding rod is made from a dielectric material is comparable to a travelling surface-wave antenna. The amount of the

guided wave or ray depends on the cross-sectional dimension of the rod. The chosen and designed cross-section shape is a circle because it can best maintain the symmetry of the radiation pattern over the azimuth angle (see Figure 1.3). For this circular shape, there is a relationship to express the dependency of the optimal directivity to the diameter of the rod's cross section. Equation (2.4) shows this relationship [7][17][38]:

$$D_\lambda \cong \frac{3}{\varepsilon_r^{3/2}\sqrt{1+2L_\lambda}} + 0.2, \tag{2.4}$$

where D_λ is the diameter of the circular rod divided by the free-space wavelength λ, ε_r the relative permittivity of the rod material, and L_λ the total length of the divided by λ. Note that this relationship is only valid for $L_\lambda > 2$ and $2 < \varepsilon_r < 5$. Normally, the polystyrene (PS) rod has D_λ value in the range from 0.3 to 0.5 λ. PS is a popular material to build the rod structure, mainly because it is easy to machine and has low loss tangent (δ). Therefore, the rod antenna is often called polyrod antenna. Other popular materials for the rod antenna are ferrite [81], teflon [3][17], and Kapton.

The wave inside the rod's dielectric material propagates slower, while the wave propagates faster outside the rod's dielectric material, i.e. free-space. It is expressed in equation (2.4) where for higher ε_r, the required diameter for the optimal directivity is smaller. This means the cross-sectional dimension of the rod can be smaller, saving the space usage. In other words, the rod with larger ε_r has more guiding effect on the wave for the same rod's diameter. More from equation (2.4), the length of the rod is less influential in determining the optimal diameter of the rod antenna. Intuitively for very long rod antenna, a high directivity may be obtained with small diameter rod since more power is collected along the rod due to slow-wave propagation along the rod's length.

When equation (2.4) is violated, for instance when $D_\lambda \ll 0.3\ \lambda$ and the material is PS, only small amount of power is confined to the inside of the rod. On the other hand, when D_λ is very large or $D_\lambda \gg 1\ \lambda$, large amount of the power is confined to the inside of the rod, and the phase velocity is nearly the same as in an unbounded medium of PS. In section 2.3, the optimization to produce even more directivity will be explained, e.g. by tapering the shape of the cylindrical rod. Note that equation (2.4) is only applicable for the base structure of the rod, but not for the tapered section or the far end of the rod element. Moreover, the relation of D_λ with radiation efficiency is reported in [73].

The theoretical approximation of the directivity D of the polyrod antenna is [7][38]:

$$D \cong 8L_\lambda. \tag{2.5}$$

Note that D is the directivity now; for its calculation, the ten-base logarithmic scale has to be incorporated here, thus D's unit is decibels (dB). This equation is only valid for the same range of L_λ and ε_r as mentioned for equation (2.4). Correspondingly, the HPBW is given by:

$$HPBW \cong \frac{60^o}{\sqrt{L_\lambda}}. \tag{2.6}$$

In [81], it is mentioned that equation (2.5) will not be applicable when L_λ keeps increasing. Instead, the directivity of the antenna will decline after some point of L_λ.

Now, the working principle of the taper in a rod antenna is explained. A relationship between the rod's dimension, the angle profile, α, of the taper section, and ε_r will be explained by means of the ray optic technique [17][44]. In this technique, the definition of the critical angle (θ_c) of the ray is coined, and a point source is assumed in the aperture plane of the metallic waveguide or launcher. The critical angle is the angle at which if it is exceeded, transmission coefficient is zero and reflection coefficient is one. This notion will be further explained in the following paragraph.

Assumed that θ is the angle of the incident ray. If θ is larger than θ_c, there will be total reflection (see Figure 2.3). The θ_c value here depends on ε_r of the rod's material. For a smaller ε_r, the θ_c has a larger value and vice versa. For a relatively large θ_c (e.g. rays no. 3 and 4 in Figure 2.3 (a)), the ray will be reflected or guided inside the rod, whereas for a relatively small θ_c (e.g. rays no. 1 and 2 in Figure 2.3 (a)), the ray will be (partly) refracted out to the free-space. If the abrupt termination occurs like in ray 4, the ray will be radiated or refracted, and the condition of the critical angle is also consistent here. The portion that is reflected will be absorbed at the port of the wave launcher (point source) or by dielectric losses inside the rod. Note that in this figure, the rays are either totally reflected or totally refracted, for the sake of the simplicity. If $\theta < \theta_c$, both reflection and transmission will actually occur.

The taper can be then introduced here to reduce the number of the reflected-back ray such as ray 3. This taper improves the matching of the rod antenna to free-space. Therefore, this taper is often called an impedance matcher between the wave impedance inside the rod to the wave impedance in free-space. Within the usable frequency range, the refracted wave combines with the guided surface wave to focus the radiated field and achieve a higher gain. Therefore, a choice of an optimal rod's length is important since a very long rod may cause destructive additions of refracted and guided waves.

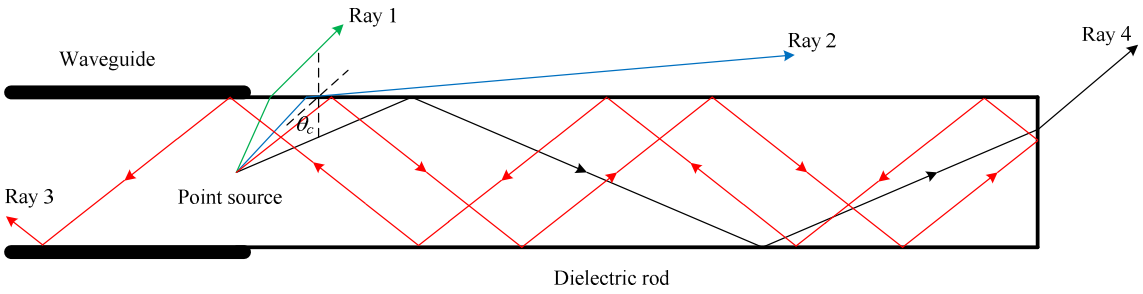

(a)

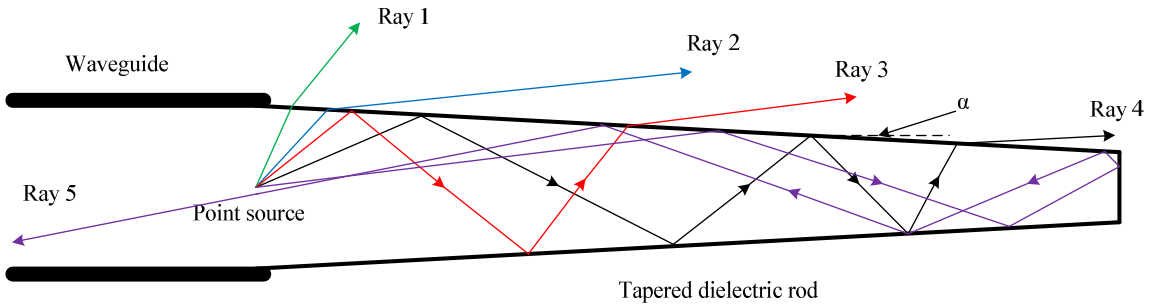

(b)

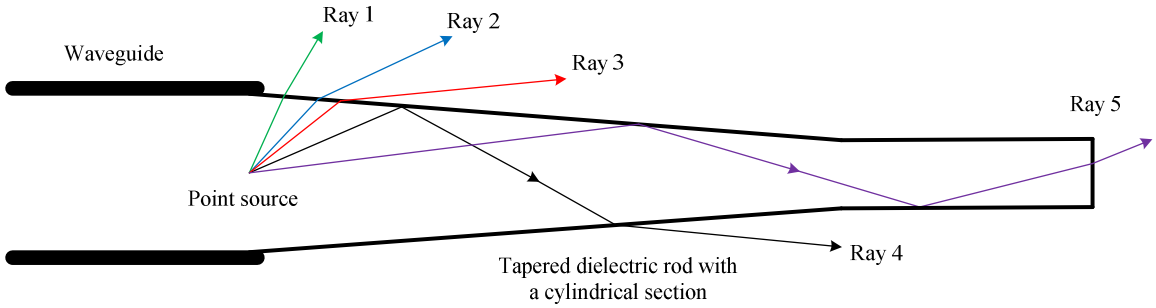

(c)

Figure 2.3. Ray paths inside (a) the uniform dielectric rod, (b) the tapered dielectric rod, and (c) the tapered dielectric rod with a cylindrical section.

In Figure 2.3 (b), ray 3 can now radiate instead of being reflected back to the launcher. This is because ray 3 increases its incident angle to the rod surface by twice the local taper angle α at each reflection, and finally ray 3 radiates as the critical angle condition is reached. It is also seen that ray 4 is still be refracted out towards the main lobe direction, instead of like the one in Figure 2.3 (a). This also explains the large sidelobe level for a uniform rod in Figure 2.2. In addition, note that ray 5 in Figure 2.3 (b) which has a relative large incident angle seems to be reflected back towards the radiator. Note that ray 5 is introduced in Figure 2.3(b) and (c) to exemplify a large-θ ray.

The power distribution along the rod affects the side-lobe performance. The ray 1 in both rod structures ((b) and (c)) is encouraged to exit the rod as soon as possible. As a result, this can yield a balanced power distribution (i.e. rotationally symmetrical distribution) along the rod. The reason is because the wide-angle rays inside this rod are associated with weaker rays from a directional source, i.e. the metallic waveguide, and these weaker rays reduce the uniformity of the phase and magnitude distribution in the rod aperture. Also, as mentioned earlier, a two-layer dielectric rod can also be incorporated in the rod structure to have a broadband operation. This is because the optimum rod's ε_r and diameter determine particular wavelength for that rod to operate properly (see equation (2.4)). To further allow weaker rays

to radiate earlier, an optimized structure with a higher slope at the taper near the launcher end is used. This can be done by means of a structure as shown in Figure 2.3 (c). The slope of the taper is higher now, but this can result in a short rod, i.e. low gain. Therefore, a section of cylindrical rod is added at the far end of the tapered section. As seen in the picture, more rays now radiates, and most of them will contribute to the radiation pattern in the main lobe.

Note that now ray 5 is prevented from being reflected due to the added cylindrical section. A fraction of the ray distribution with a range of incident angles can be prevented from being reflected at the tip of the rod, due to the added cylindrical section. In Figure 2.3(c), the tapered section refracts the rays with a range of incident angles that may be reflected at the tip if they are in the rod in Figure 2.3 (b). Therefore, in Figure 2.3(c), the rays that can now reach the tip only the rays that can radiate. The optimization of this structure will be explained more in detail in section 2.3.

2.1.2 Field configuration

In this section, the field expressions for the dielectric rod with a circular cross section will be discussed. This structure can be regarded as a circular waveguide made from a dielectric material. For a cylindrical-dielectric-rod structure, the dominant $HE_{1,1}$ mode fields always exist, no matter how large the diameter of the rod's cross section is. Therefore, the presence of the $HE_{1,1}$ mode is not determined by the diameter although a minimum value is required, whereas the first higher-order modes ($TE_{0,1}$, $TM_{0,1}$, and $HE_{2,1}$) can propagate in case [21]

$$\varepsilon_r > 1 + \left(\frac{2.4048}{k_0 a}\right)^2, \tag{2.7}$$

where a is the radius of the rod and k_0 is the wave number in free-space. The next higher-order mode is the $EH_{1,1}$ mode, and its precondition is given by equation (2.7) after replacing 2.4048 with 3.8317. These numbers, so-called cutoff values, for a cylindrical-dielectric-rod structure are summarized in [84]. It can be observed that this cutoff value for $HE_{1,1}$ mode is 0 (i.e. replacing 2.4048 with 0). In the design, the radius (a) is chosen to have slightly smaller value before the first higher-order modes are excited so the radius also meets the requirement to have high radiation efficiency as expressed in equation (2.4). Note that equation (2.4) is to determine the radius for the optimal directivity.

This dominant $HE_{1,1}$ mode has the dispersion relationship for a a cylindrical-dielectric-rod structure surrounded by free-space medium given by [46]:

$$\left[\frac{J_1'(u)}{uJ_1(u)} + \frac{K_1'(v)}{vK_1(v)}\right]\left[\frac{J_1'(u)}{uJ_1(u)} + \frac{K_1'(v)}{\varepsilon_r vK_1(v)}\right] = \left(\frac{1}{u^2} + \frac{1}{v^2}\right)\left(\frac{1}{u^2} + \frac{1}{\varepsilon_r v^2}\right). \tag{2.8}$$

$J_n(.)$ and $K_n(.)$ are the n-th order Bessel function of the first kind and modified Bessel function of the second kind, respectively [90]. $J_n'(.)$ and $K_n'(.)$ are the derivatives of the Bessel functions and are expressed in their recurrence relationships

$$J_n'(z) = \frac{1}{2}[J_{n-1}(z) - J_{n+1}(z)] \text{ and} \tag{2.9}$$

$$K_n'(z) = \frac{1}{2}[K_{n-1}(z) + K_{n+1}(z)], \tag{2.10}$$

respectively. $u = k_\rho a$ and $v = \alpha_\rho a$ where

$$k_\rho = \sqrt{k_0^2 \varepsilon_r - k_z^2} \tag{2.11}$$

$$\alpha_\rho = \sqrt{k_z^2 - k_0^2}. \tag{2.12}$$

k_z is the waveguide propagation constant in the axial direction.

The rectangular coordinate system will be used here because it is more convenient to express the configuration of the field values. The $HE_{1,1}$ mode is degenerated due to the circular symmetry, namely $HE_{1,1}^x$ and $HE_{1,1}^y$. For the mode $HE_{1,1}^x$ with dominant field components E_x and H_z, the field expressions in the rod's core (i.e. for $\rho \leq a$) are [46][85]: (where a is $\frac{1}{2}$. rod diameter ($Ø_{wg}$) or radius of the rod)

$$E_x(\rho,\varphi) = j\frac{Ak_z}{2k_\rho}[(1-s)J_0(k_\rho\rho) + (1+s)J_2(k_\rho\rho)\cos(2\varphi)] \tag{2.13}$$

$$E_y(\rho,\varphi) = -j\frac{Ak_z}{2k_\rho}(1+s)J_2(k_\rho\rho)\sin(2\varphi) \tag{2.14}$$

$$E_z(\rho,\varphi) = -AJ_1(k_\rho\rho)\sin(\varphi) \tag{2.15}$$

$$H_x(\rho,\varphi) = -j\frac{A\omega\varepsilon_0\varepsilon_r}{2k_\rho}(1+s_1)J_2(k_\rho\rho)\sin(2\varphi) \tag{2.16}$$

$$H_y(\rho,\varphi) = -j\frac{A\omega\varepsilon_0\varepsilon_r}{2k_\rho}[(1-s_1)J_0(k_\rho\rho) + (1+s_1)J_2(k_\rho\rho)\cos(2\varphi)] \tag{2.17}$$

$$H_z(\rho,\varphi) = -\frac{Ak_z s}{\omega\mu_0}J_1(k_\rho\rho)\cos(\varphi) \tag{2.18}$$

while in the rod's surrounding free-space (i.e. for $\rho > a$), the field expression are:

$$E_x(\rho,\varphi) = j\frac{Ak_zJ_1(u)}{2\alpha_\rho K_1(v)}[(1-s)K_0(\alpha_\rho\rho) - (1+s)K_2(\alpha_\rho\rho)\cos(2\varphi)] \tag{2.19}$$

$$E_y(\rho,\varphi) = -j\frac{Ak_zJ_1(u)}{2\alpha_\rho K_1(v)}(1+s)K_2(\alpha_\rho\rho)\sin(2\varphi) \tag{2.20}$$

$$E_z(\rho,\varphi) = -A\frac{J_1(u)}{K_1(v)}K_1(\alpha_\rho\rho)\sin(\varphi) \tag{2.21}$$

$$H_x(\rho,\varphi) = j\frac{A\omega\varepsilon_0 J_1(u)}{2\alpha_\rho K_1(v)}(1+s_0)K_2(\alpha_\rho\rho)\sin(2\varphi) \tag{2.22}$$

$$H_y(\rho,\varphi) = -j\frac{A\omega\varepsilon_0 J_1(u)}{2\alpha_\rho K_1(v)}[(1-s_0)K_0(\alpha_\rho\rho)-(1+s_0)K_2(\alpha_\rho\rho)\cos(2\varphi)] \tag{2.23}$$

$$H_z(\rho,\varphi) = -\frac{Ak_z s J_1(u)}{\omega\mu_0 K_1(v)}K_1(\alpha_\rho\rho)\cos(\varphi), \tag{2.24}$$

where A is the amplitude constant and

$$s = \left(\frac{1}{u^2}+\frac{1}{v^2}\right)\left[\frac{J_1'(u)}{uJ_1(u)}+\frac{K_1'(v)}{vK_1(v)}\right]^{-1} \tag{2.25}$$

$$s_0 = \frac{k_z^2}{k_0^2}s_n \text{ and } s_1 = \frac{k_z^2}{\varepsilon_r k_0^2}s_n. \tag{2.26}$$

Using the simulation for the designed rod structure, i.e. $a = Ø_{wg}/2$ = 1.5 mm and $Ø_{rt}/2$ = 0.82 at 60 GHz (see Figure 2.18), equation (2.13)-(2.15) and (2.19)-(2.21) are plotted in Figure 2.4. Because the rod is fed from *x*-axis direction, the dominant field components are E_x and H_z (see Figure 2.1). It can be seen that expressions (2.13)-(2.15) are separated from expression (2.19)-(2.21) through a dielectric-air boundary condition; tangential fields over the rod surface are thus enforced to be zero.

It can be verified from Figure 2.4 (b) that for a relatively large ε_r = 2.53, a large portion of the power is carried out outside the dielectric, while e.g. for foam material where ε_r is close to one, most of the power is carried inside the cylinder. Moreover, Figure 2.4 (a) shows that the field value at the dielectric boundary is relatively high. Inside the dielectric cylinder the $HE_{1,1}$ mode field is mostly linearly polarized. Also, the cross polarization has non-negligible amplitudes outside the dielectric (see Figure 2.4 (b)). This is the advantage of the rectangular coordinate system that can show the cross polarization.

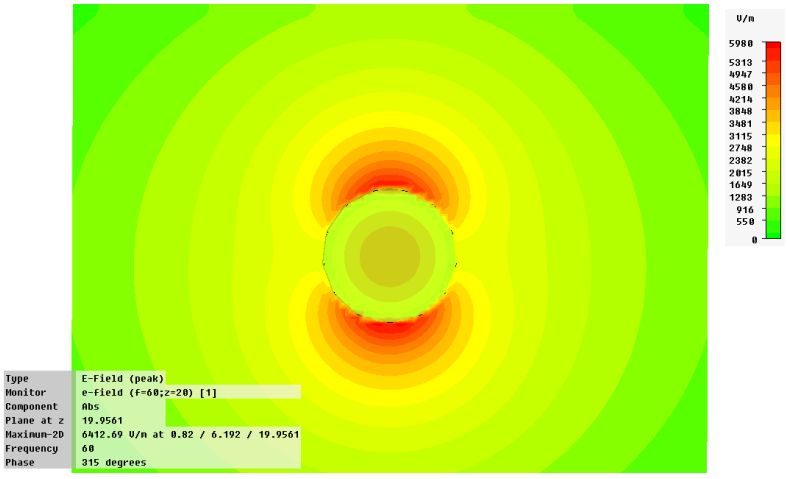

(a)

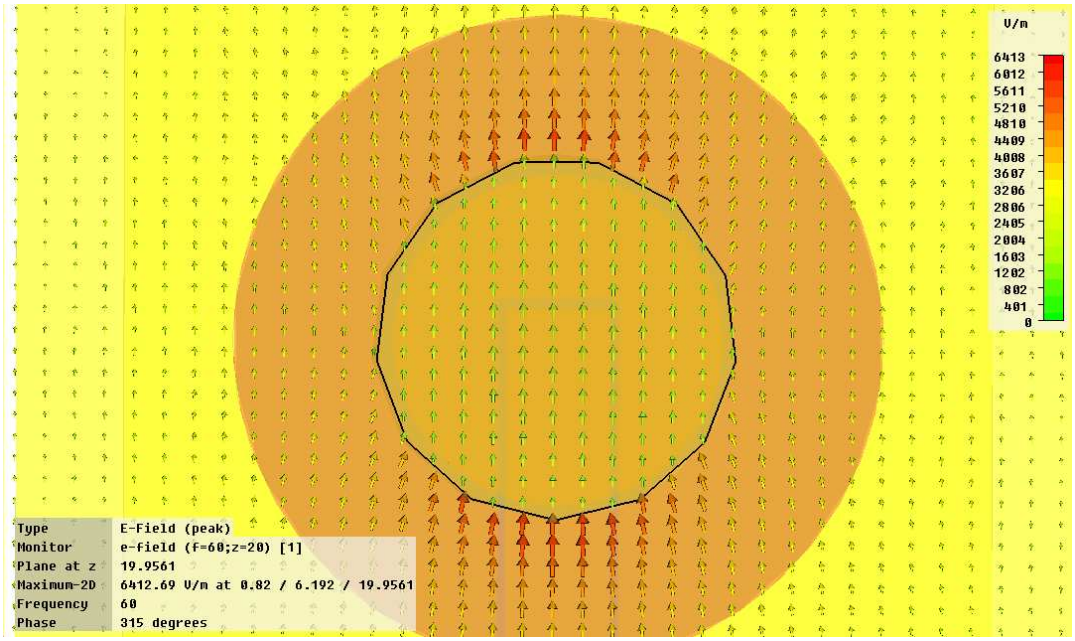

(b)

Figure 2.4. Electric field (E-field) for the HE_{11} mode in circular dielectric waveguide with diameter $Ø_{rt}$ = 1.64 mm, ε_r = 2.53 at 60 GHz: (a) absolute E-field and (b) E-field lines.

2.2 Design iteration of the rod antenna

The design of the rod antenna takes several steps; first by investigating the current available design in [3], [4], [5], and [17] and subsequently by improving the performance to meet the specification as mentined in section 1.5. The chosen dielectric materials play a major role in the design decision as well. This is mainly because the feasibility to machine this material by available manufacturers has to be included in the design process. Hence, the accuracy that can be obtained by the technology from the manufacturer to build the structure has to be confirmed as well. Moreover, the yield analysis for fabricating a planar structure is indispensable. In the following discussion, several materials will be tested and discussed since they are used in the designed structure. Table 2.1 serves as a summary of material properties if they are not mentioned explicitly in this report.

Currently it is reported that for gluing stacked LCP material by means of bond-ply or prepreg material may result in low yield performance since blistering may occur [68][69]. It is even worse if a multilayered structure needs to be designed for a large dimension (i.e. for an array); then a probability to have a blistering in the structure gets higher. Therefore, a design with a single layer LCP material is prefered, but this again has to be traded off with the bandwidth which depends on the thickness of the substrate material. 0.16 mm thick LCP

material is thin enough (approximately 2 layers of LCP plane), and it can support the desired bandwidth as will be reported in the subsequent section.

Table 2.1. Properties of investigated materials at 60 GHz.

	Relative permittivity, ε_r	**Loss tangent, δ**
LCP [59][60][61]	3.1	0.0045
PS [71]	2.53	0.00094
Teflon [3][4][71]	2.1	0.00022
Kapton [17][70]	2.8	0.002

For the first design iteration, Figure 2.5 shows the structure of the dielectric rod antenna array with a metallic waveguide surrounding the array's base. To achieve a larger scan range, this conformal is designed. The rod antenna consists of two main sections, namely the uniform section and the tapered section. The uniform section of the rod has the height of only 3 mm, and the remaining 32 mm is for the tapered section. The height of the metallic waveguide is 1 mm. The diameter of the tapered rod is from 1.7 mm at the rod's base to 0.6 mm at the rod's tip, and the diameter of the uniform rod is made equal to the largest diameter of the tapered rod to avoid unnecessary discontinuity. The material of the rod is Kapton (Duroid's Polyimide) with ε_r = 2.8 at 60 GHz [70]. Before this material, a Teflon material which has lower loss tangent (δ) was chosen, but this material is difficult to machine by the manufacturer. Therefore, the antenna structure with Kapton material is designed and simulated here.

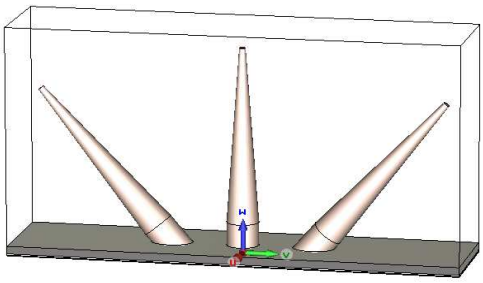

Figure 2.5. Array of the dielectric rod antenna.

The feeding type is a coaxial probe attached at the lower part of the structure, and the dimension of this feeding probe is optimized to achieve 50 Ω characteristic impedance. The body of the coaxial feed is then embedded through the substrate from the bottom part of the antenna until it touches the metallic radiator. This metallic radiator is photoetched on LCP

substrate with ε_r = 3.1. The metal patch is exactly created at the lower surface of the rod antenna with circularly planar geometry, a so-called circular patch. This patch antenna excites the electromagnetic wave to the dielectric rod section, yet may introduce some reflection due to the limited transition efficiency of this patch to the rod structure. This unavoidable issue can be minimized by choosing the similar dielectric property of the rod material with the planar substrate (e.g. rod made from LCP). However, due to the limitation in the manufacturing and molding processes, the cost of the material, and the required dielectric property of the material, the choice of the same material for both the rod and the plannar substrate cannot always be possible. The LCP for planar structure itself is chosen due to its good characteristic in the millimeter-wave band and its material flexibility, which later can be bent to create a conformal structure.

The return loss or reflection coefficient result of this antenna can be seen in Figure 2.6. Here, the antenna exhibits a low return loss around the 60-GHz frequency band. For most applications, the bandwidth is generally defined as the criterion where the reflection coefficient (S_{11}) is lower than -10 dB. Consequently, the bandwidth of the antenna is around 4 GHz (from 58 to 62 GHz). Nevertheless, for highly sensitive applications, i.e. radiometry, more strict criterion is recommended for having much lower reflected power. The filtering can be thus introduced in the RF electronic system to obtain only 1 GHz bandwidth around the center frequency of 60 GHz where the antenna system has the best performance (S_{11} < -25 dB). With this new bandwidth criterion, a radiometer system with an error of around 0.5 K can be obtained [86]. However for the current design, the antenna is designed for a general wireless-communication applications, thus S_{11} < -10 dB is sufficient.

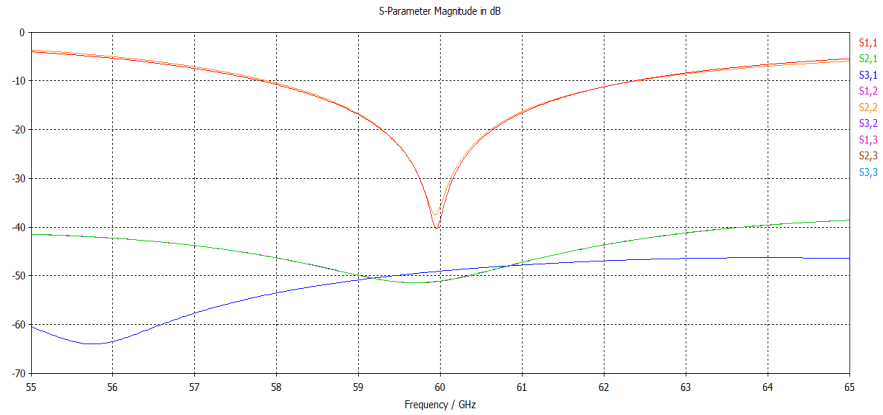

Figure 2.6. S-parameter in the frequency range from 56 to 64 GHz, simulated using the time domain solver with 40° inter-element angular distance (θ_{el}).

The other antenna elements of this array system are also evaluated here. This is plotted in the figure with slightly increasing indices of the S_{11} value at 60 GHz. Also, the mutual coupling has to be investigated because if it is not properly controlled, the radiation performance may degrade due to the disturbed energy balance inside the rod. The mutual coupling between antenna elements, which is less than -40 dB, is obtained. This shows the

good isolation between antenna elements, which results from the very directive antenna element.

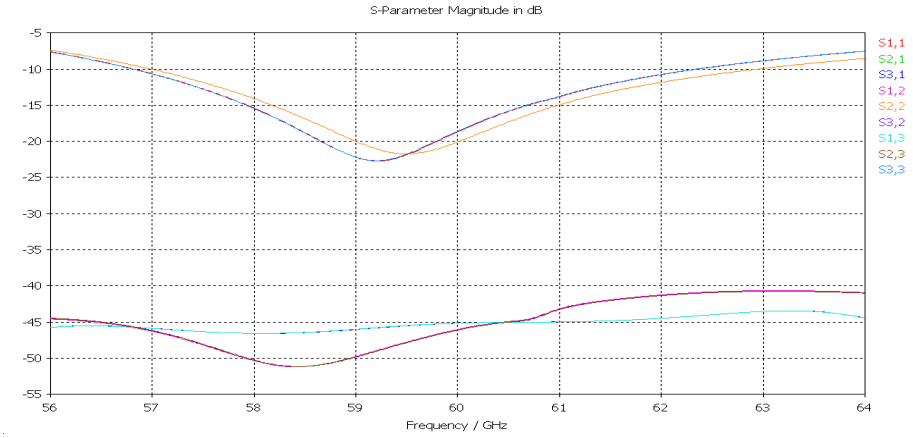

Figure 2.7. S-parameter in the frequency range from 56 to 64 GHz, simulated using the frequency domain solver with 40° inter-element angular distance (θ_{el}).

Figure 2.7 portrays the S-parameter of the same antenna solved by the frequency domain solver. From the result, the slight shifts of the S-parameter are considered reasonable since the simulation setting is prepared to accommodate the available memory and simulation time resources. Unless otherwise specified, the subsequent simulation result will be done by means of the time domain solver of the CST MWS^{TM} simulator.

The array configuration of the rod antenna with certain angular orientation (see Figure 2.5) can result in radiation pattern's main lobe in that angular orientation. Since the rod antenna is to radiate and intercept the electromagnetic radiation with an end-fire pattern, the angular distance between rod antennas determines the pointing resolution. Figure 2.8 depicts the radiation pattern of the dielectric-rod antenna array using two different materials, namely polystyrene (PS) and Kapton [70] [71]. The PS material is chosen here as the second design iteration where this material exhibits low loss tangent (δ) compared to what Kapton does.

The solid line is the radiation pattern using the PS material whereas the dashed line is the one with the Kapton material. The good performance of the PS antenna can be seen as this material has δ = 0.00094 at the 60 GHz frequency band. The version of the 40° tilted antenna has the main lobe around 40° and, correspondingly, it is the same for the -40° one. The important result is that the tilted PS antenna exhibits higher sidelobes, especially at the same direction as the main lobe of the upright rod antenna. This may result in interference when the antenna is intended to operate at, for example, 0° instead of 40°. Nonetheless, this sidelobe magnitude is very low compared to the main lobe magnitude of the upright rod antenna, which is 12.6 dBi. The Kapton antenna has much lower sidelobes at the expense of the lower gain. More important issue for this array structure is that the uniformity among the rod element is not preserved, e.g. the sidelobe level of the tilted element. This is because of the flat base structure.

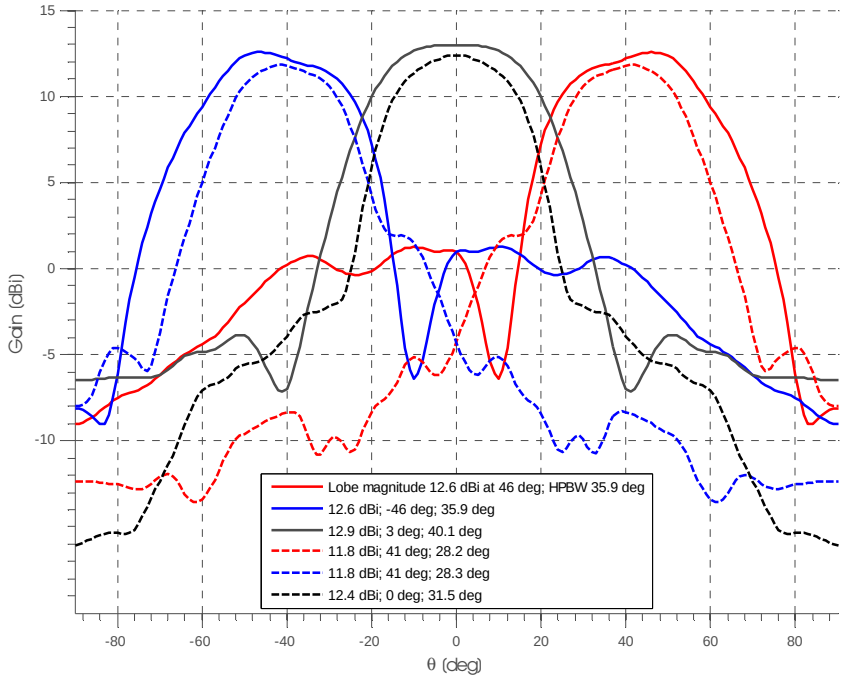

Figure 2.8. Radiation pattern of the dielectric-rod antenna array: The comparison between PS and Kapton rod antenna.

To achieve higher gain, the dielectric material with very low loss tangent is preferable. Teflon (PTFE) has the lowest loss tangent (δ) compared to the other materials. Although it is not shown in Figure 2.8, the realized gain for this antenna is around 14 dBi which is 1.4 dB larger than the rod material made from PS. Unfortunately, as mentioned earlier, this material is hard to machine, especially for its small and very precise dimension. Also, this rod may have broader beamwidth due to the very low permittivity (ε_r = 2.1) [3] [4]. This is due to the fact that rays inside a low ε_r can be easily refracted to the free space, thus the rays with very low incident angle tend to refract from the rod to free-space earlier.

The suitable and recommended material for dielectric rod is numerous [10]; polyurethane foam ($\varepsilon_r = 1.5$), PTFE ($\varepsilon_r = 2.1$), polystyrene (PS) ($\varepsilon_r = 2.53$), plexiglass [14], and nylon ($\varepsilon_r = 3.0$), due to their good mechanical properties. As mentioned earlier, one of the most important parts for antenna design is the electrical performance of the material. Hence, the PS material that has almost similar ε_r with the LCP material (i.e. to improve the matching) and has very good electrical performance at microwave and millimeter-wave frequencies is appropriate for the rod material. Kapton, family of polyimide (PI), may also be a good choice for its material robustness, ease to manufacture, and shear restraint. However, its large loss may make it less popular in its usage for dielectric structure. Therefore, a careful choice of low-loss dielectric material is necessarily important, whereby the structure with this material exhibits high radiation efficiency.

From this it can be concluded that PS material can be used for the final design as not only is it easy to machine, but it also has low δ. The sidelobe from the tilted rod from the structure shown in Figure 2.5 can be avoided by creating an array structure with a conformal planar base. Therefore, every antenna element can have the pattern as close to the case of a single element antenna. These design decisions will survive and be further explained in section 2.3.

The third design iteration is to increase the gain of the single element e.g. by optimizing the rod shape as is discussed in section 2.1.1 of this report. The optimized dimension of this antenna type is almost similar to the last type. Only now the position of the uniform section and the tapered section are interchanged (see Figure 2.9). The dielectric rod with ε_r = 2.53 and δ = 0.00094 of PS is used here, which is, as mentioned earlier, a good material characteristic for achieving the high radiation efficiency of the antenna system. These parameters of the dielectric material are suitable for the 60-GHz operation frequency. The metallic waveguide is filled with copper or gold plating to provide a higher conductivity with a lower cost of manufacturing. In this configuration, the substrate dimension is 10 x 10 mm for a single element rod antenna.

The length of the uniform section is 20 mm (h_{cr} = 4λ) while the length of the tapered section is 15 mm (h_{tr} = 3 λ). The configuration of the taper is to mimic the curvilinear taper though, in this case, it is linear. As discussed in 2.1.1, a continuous taper section is prefered, such as the curvilinear taper, but it is relatively difficult to manufacture such a continuous taper. This is because it is difficult to create the mould that has that curvilinear shape. Therefore, a taper combined with a uniform section is being used here. The aim is to ease the manufacturing process and also to give strong support to such thin construction. The substrate's thickness is 160 µm, and beneath it a ground plane made from a conducting material, i.e. copper, is utilized.

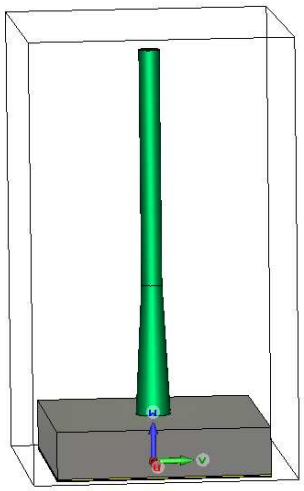

Figure 2.9. Dielectric rod antenna with a waveguide: An optimized rod shape.

Although the result is not shown here for the sake of conciseness of the report, it is observed that more gain is obtained compared to the result of the second design iteration (see Figure 2.5 for the rod using PS material). Eventually, the final design, i.e. the fourth, iteration will be reported and discussed in detail in section 2.7.

The dimension of the rod antenna is relatively large (typically $h_{cr} + h_{tr}$ = 6 - 9λ) with very narrow cross section which allows to be densely packed. The narrow cross section is very important when building a conformal array of this antenna, at the expense of a long structure in order to meet the gain requirement. Another structure in [14] is proposed to meet similar gain with lower axial length though its cross section is in the same order of its length. The narrow cross section can be obtained by means of the high permittivity of the dielectric rod material such as monocrystalline sapphire and silicon [16]. However, this does not affect the requirement of the rod's axial length, as is explained in equation (2.5). The decision for the height will be explained in section 2.7.

2.3 Optimization of the rod antenna

First step for optimizing the rod antenna is by incorporating the metallic waveguide structure or launcher to the structure. The use of this launcher has been included from the first design iteration in section 2.2. This paragraph will explain further about it. This launcher is intended to suppress higher-order modes of propagation that may be excited either at the input or by an imperfection such as the substrate inhomogeneity [84]. This inhomogeneity exists in the transition between the LCP material and the PS material. The higher-order modes, that for some cases may be excited have to be suppressed (see section 2.1.2) [21]. A lossy outer region or a metallic launcher can handle this. A careful choice of the metal material has to be taken, because the eddy current may introduce loss in the metal surface. Moreover, the height of this launcher has to be optimized since after some point, a further height increase may reduce the gain performance. This is because the metallic waveguide has a resonance and reduces the radiation from the tapered rod [3]. The optimized height for this launcher is 2.5 mm.

The radiation pattern is then determined not only by the dielectric rod but also by the launcher (see Figure 2.10). The $HE_{1,1}$ mode only contributes to the radiation inside a "trapping region", $-\theta_T < \theta < \theta_T$. The pattern due to the launcher exists everywhere but predominates outside the "trapping region". This is advantageous especially if a low-sidelobe radiation pattern needs to be designed. The reason is that the rod without a waveguide may have significant sidelobes as a result from the radiation near the bottom of the rod. The trapping angle θ_T is given by [21]

$$\theta_T = arccos\left(\frac{1}{\sqrt{\varepsilon_r}}\right). \tag{2.27}$$

Later on in Figure 2.20, the trapping region can be observed between -51 - 51° of the red curve. Outside this region, the radiation pattern is predominated by the waveguide. Inside this region, the radiation pattern is influenced by both the waveguide and the dielectric rod.

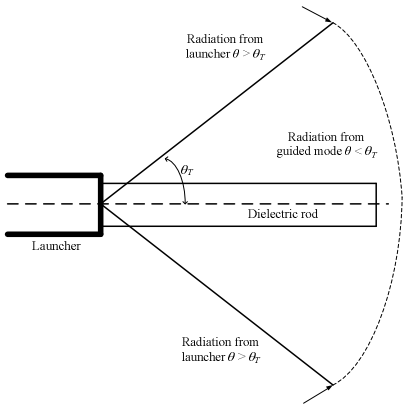

Figure 2.10. Influence of the launcher in the radiation pattern of the whole antenna structure.

This metallic waveguide is designed in such a way it gives gain from electromagnetic view point and is easy to produce from manufacturing viewpoint. The hollow circular waveguide is sufficient to reduce the sidelobe in the antenna radiation pattern. This sidelobe is generated by rays that have a large angle near the excitation point at the bottom of the rod. Nonetheless, in its sole use as the electromagnetic guiding and transition into free-space, its impedance transition performance is still less than the conical waveguide [11]. However, the design decision to incorporate the tapered rod antenna as filling dielectric inside the hollow waveguide alleviates the problem of impedance matching. The so-called matching section between dielectric and free space is required near the aperture of the metallic waveguide for best performance. The taper structure, as a matching section, significantly reduces the reflected electromagnetic wave, thus most of the wave is refracted to the space. Consequently, the benefits such as reduced sidelobe and matching condition can be fulfilled in simple yet robust design.

A unique rod design has been reported in [78] to produce high gain by detaching the surface wave from the rod. However, such a structure is very difficult to machine. In Figure 2.9, the optimized rod shape is shown. As the second step for the optimization, Figure 2.11 plots the pattern for different diameter ($Ø_{rt}$) of the rod's uniform section. It can be observed that $Ø_{rt}$ = 1.6 mm has a low SLL, i.e. < -15, and a small HPBW. If the diameter keeps increasing the SLL will increase, though the HPBW is slightly decreased. On the other hand, if the diameter is reduced the SLL may reduce, but the HPBW increases. A large HPBW is not always preferable because it is often related to a low gain antenna, as can be seen in Table 2.2. From the figure, it can be also observed the back lobe for $Ø_{rt}$ = 1.6 mm is very low. Therefore, $Ø_{rt}$ = 1.6 mm is chosen and can meet the design specification in section 1.5.2 of this design report. The design decision is indicated as the dashed column.

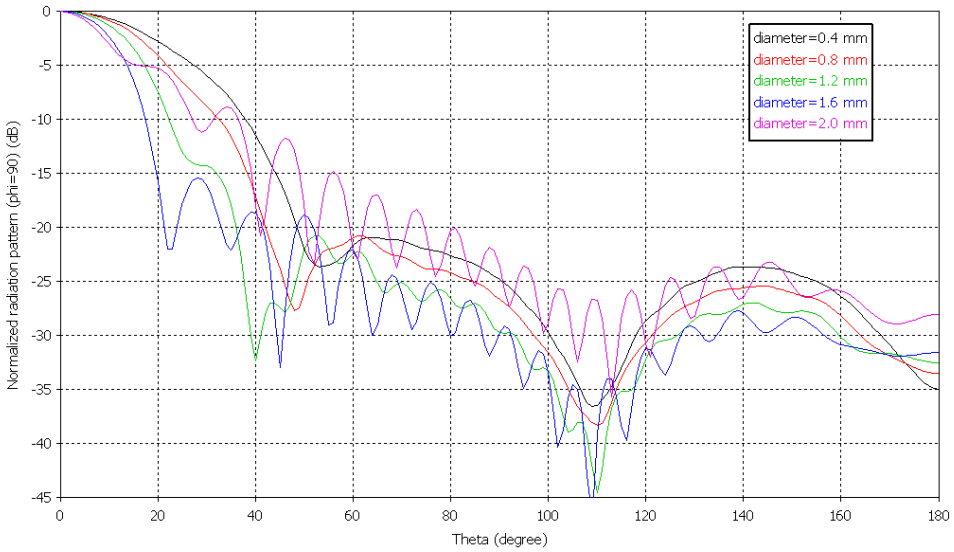

Figure 2.11. Comparison of the sidelobe pattern for different cylindrical rod diameters ($Ø_{rt}$) (see Figure 2.18(a)).

Table 2.2. Antenna performances for different cylindrical rod diameters ($Ø_{rt}$) (see Figure 2.11).

Diameter ($Ø_{rt}$) (mm)	0.4	0.8	1.2	1.6	2
Gain (dB)	12.7	14.1	16.2	17.9	14.4
HPBW (deg)	41.5	35.1	28.5	22.3	20
SLL (dB)	-20.9	-20.8	-20.7	-15.4	-8.9

The third step for the optimization is displayed in Figure 2.12. The picture plots the pattern for different length ratios (r_{tl}) of the tapered section (h_{tr}) to the overall rod (h_{tr} + h_{cr}) (see Figure 2.18(b)). It can be observed that r_{tl} = 37.5 % has the lowest SLL, i.e. ~ -15, and a low HPBW. If the r_{tl} is increased the SLL will increase, and the HPBW is dramatically increased. This is again related to the result in Figure 2.2, where the uniform rod exhibits high SLL. On the other hand, if the r_{tl} is reduced the SLL increases rapidly, but the HPBW remains the same. Therefore, r_{tl} = 37.5 % is chosen and can meet the design specification in section 1.5.2. Table 2.3 summarizes the gain for various r_{tl} value.

Table 2.3. Gain performance for different length ratios (r_{tl}) (see Figure 2.12).

Length ratio (r_{tl}) (see Figure 2.12)	12.5%	25%	37.5%	50%	62.5%	75%	87.5%	100%
Gain (dB)	16.6	17.7	17.9	17.4	16.3	15.1	14.2	13.9

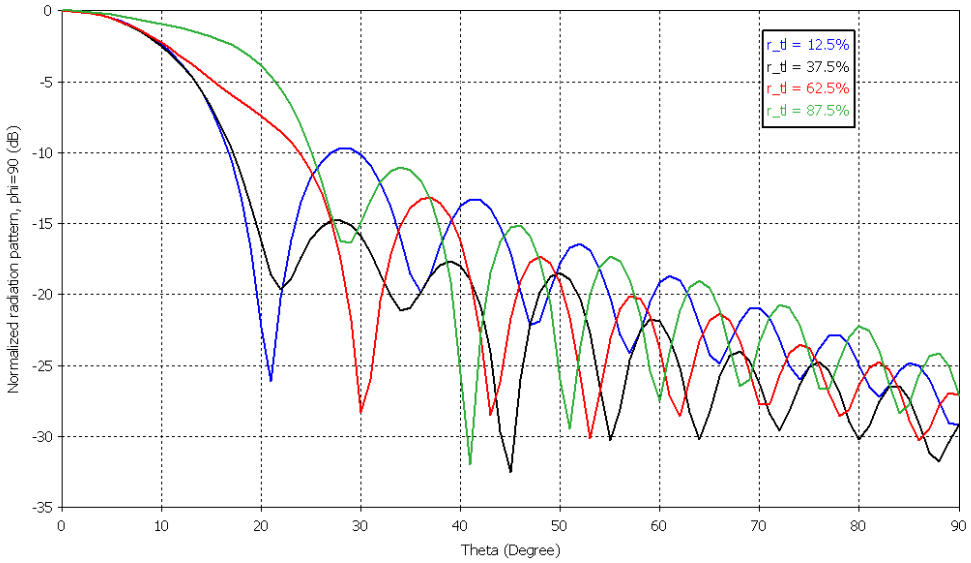

Figure 2.12. Comparison of the sidelobe pattern for different length ratios (r_{tl}) of the tapered section (h_{tr}) to the overall rod (h_{tr} + h_{cr}) (see Figure 2.18(b)).

2.4 Patch-fed structure

This section focuses on the mechanism to feed the rod antenna. The use of the conventional horn antenna to excite the rod may be too bulky and is thus avoided, especially for the application that necessitates a compact and light-weight design. In addition, the λ/4 section for the this feeding type may require an additional space at the bottom part that may expand out of the substrate thickness itself. A patch-fed technique is on the other hand suitable to have a compact and less complex design as shown in Figure 2.13.

The patch-fed technique may exhibit narrow band performance due to microstrip's narrow band performance. Nevertheless, planar structure is the most versatile choice for nowadays microwave and millimeter-wave applications. Therefore, the efficient transition between rod and patch microstrip structures is of a great interest when looking into each structure's inherent benefit. In addition, the bandwidth performance can still be increased by

using a thick dielectric substrate. However, the presence of the PS substrate of the rod structure enhances the bandwidth itself. In this way, nevertheless, the reflection due to the inhomogeneity has to be taken into consideration.

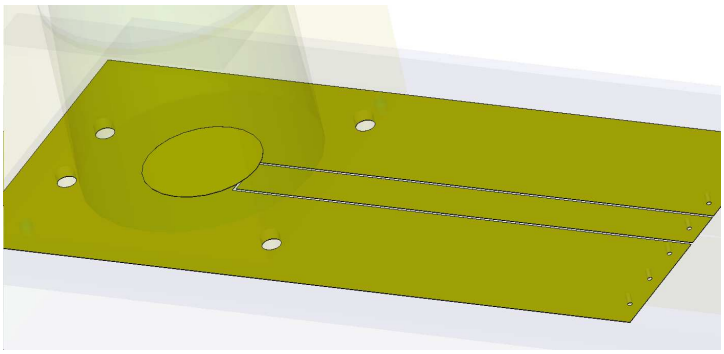

Figure 2.13. Transition to the rod antenna using an electromagnetically-coupled circular patch antenna.

The shape of the patch is a circle to match with the shape of the dielectric waveguide. To dimension this circular patch for the 60-GHz operation frequency, the formulas are given in [87]. Note that the patch is now inside inhomogeneous dielectric layers, i.e. PS and LCP.

The coplanar waveguide (CPW) is used as the feed line structure in this design due to its low attenuation [66]. Also, the shunt and series lumped elements can be easily added to a CPW feed line without affecting the characteristic impedance of the transmission line. This is due to the flexible distance between the signal strip and the ground strip of the CPW. For the microstrip feed line, the realization of these elements requires the change in the substrate thickness since the ground plane is at the opposite side of the signal strip. The CPW in Figure 2.13 also acts as a metallic reflector to reduce the backward radiation of the antenna system.

To determine the characteristic impedance, the choice of the dielectric material will influence the cross-section dimension of the CPW. A large ε_r requires less gap width (w_g) (see Figure 2.18 (a)); this may sound as less space requirement, but it perhaps does not fit the capability of the manufacturer to etch the structure. More detailed discussion of the CPW line will be in section 2.5.

A part in the LCP substrate between the metallic waveguide and the ground plane may have a potential difference and resonances at arbitrary frequencies (i.e. depending on the cross-sectional dimension of the waveguide). A trapped surface wave also occurs here, that can increase the sidelobe and increase the mutual coupling in an array structure. To alleviate this, four via holes are introduced (see Figure 2.13) to equate the potential between the waveguide and the ground plane. However, these vias can create a new antenna structure, so-called planar inverted-F antenna (PIFA), due to the shorting elements to the ground plane. This means that a resonance at unknown frequencies may still be generated. In [88], by increasing the distance of the shorting via relative to the feed point, the antenna's input impedance is increased. This means that the PIFA mode will not resonate and radiate, especially around the frequency band of our interest. The via dimension has to be small

enough to give a higher input impedance, e.g. 350 Ω, at particular frequency. The optimization has been done using the CST MWS™ simulator.

2.5 Transmission line structure

This section, as a continuation of the previous section, discusses the structure of the transmission line. Also, this section supplements the line features that will be used in the RF MEMS design in Chapter 3 (section 3.3). In that chapter, the line features may include the tapering, bend, transition, and chamfering in the FGCPW transmission line. The design of the FGCPW will be discussed here.

2.5.1 Coplanar waveguide

The dimension of the CPW line's cross section is designed to meet the requirement of 50-Ω characteristic impedance. This dimension can be calculated using formulas given in [92]. The reactance of the line structure depends on the CPW dimension. The reactance here is frequency-dependent, thus the conventional CPW structure will most likely exhibit the response of a low-pass filter. To define its cut-off frequency, the reactance, namely the inductance and the capacitance, can be adjusted to the need. Therefore, it is necessary that the LC product of the line structure is small enough to meet the requirement in a millimeter-wave structure. The CPW line can be modeled in an equivalent circuit. The width of the signal strip in the CPW here influences the serial inductance of the line impedance. The shunt capacitance comes as the gap width of the CPW. Both distributed elements are of a great importance to design a proper transmission line structure, i.e. a matched transmission line.

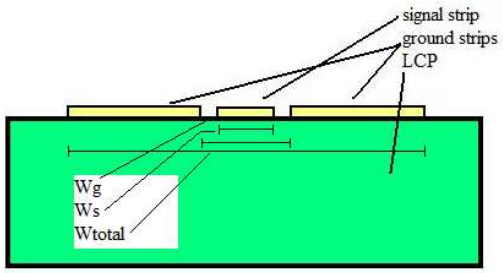

Figure 2.14. Cross-sectional view of a CPW.

This CPW cross-sectional view can be found in Figure 2.14. With this configuration, an even mode of TEM type will be generated [66]. Notwithstanding, inhomogeneous dielectrics occur when several dielectrics, namely ε_r's and μ_r's, exist or vary with position in the dielectric. In this case, the wave is not propagating in a strictly TEM fashion but instead

in a quasi-TEM. Also, for the CPW structure as shown in Figure 2.13 and Figure 2.14, because the ground plane is truncated at the right- and left side, it is a CPW variant named finite-ground coplanar waveguide (FGCPW) [67] or three coplanar strips [67]. If $\frac{w_{total}}{w_s+2w_g} > 5$, the impedance of the conventional CPW is affected by less than about 3% [67].

The resistance of the conductor at high frequency is no longer constant. It is due to the fact that most of the current distribution propagates in the outer part of the conductor strip, e.g. of the CPW. As a result, there is no uniform current distribution across the conductor section. This so-called skin effect results in more resistance of the strip line at higher frequency. Furthermore, the width of the strip influences not only the return loss characteristic but also influences the insertion loss of the transmission line. Therefore, usually a shorter transmission line is more preferred because of its smaller insertion loss, and a smaller cross section is more suitable for higher operation frequency because of its smaller insertion and return losses. The major portion of the insertion loss results from the cross-sectional dimension of the transmission line.

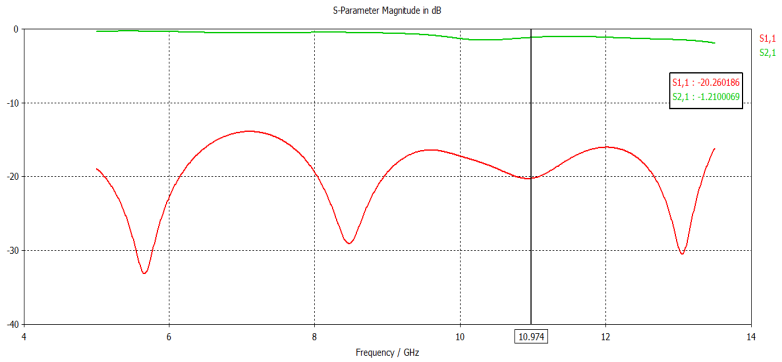

Figure 2.15. S_{11} and S_{21} of a CPW transmission line at the microwave frequency band.

Figure 2.15 shows an exemplary result for the return loss (S_{11}) and the insertion loss (S_{21}) at microwave frequency. It can be seen that the insertion loss increases with the frequency, while the return loss still has no significant difference for that frequency progression. It can be expected that the low-pass behavior can be observed when a larger frequency range is simulated.

There is also another challenge to design a transmission line. Sometimes, the manufacturer's capability to shape the metal structure is limited to a precision value, e.g. QPI can shape a metallic planar structure up to 70 µm wide and 2 µm thick. In addition, different gap widths due to the less precise fabrication for a CPW may produce odd mode of propagation since there are different left-side and right-side potentials between conductor strips, i.e. different electric fields. Therefore, the challenge here is to design 60 GHz transmission line structure that can meet the manufacturability, repeatability, and performance. Besides, the substrate material also has an important factor when dimensioning the structure. A smaller structure can be realized using a higher dielectric's relative permittivity with the same operation frequency. Last but not least, the material homogeneity with position in the material has to be considered as well.

2.6 Preparation for the simulation

As mentioned in section 2.1.1, the antenna structure is simulated and optimized by using CST MWS^{TM}, which is a full wave simulator based on a finite integration technique (FIT) method in time domain [51]. The key idea of this method is, in the finite discretization, to use the integral form of Maxwell's equations rather than to use the differential form [18][19]. In addition to that, the FIT can be also used to perform frequency domain simulation, to verify the time domain method or vice versa.

Table 2.4. Sources of simulation error and inaccuracy.

	Error and inaccuracy	**Prevention**
1	Geometry error	Careful checking of the structure dimension, especially if the structure is imported from other software.
2	Material parameters	Most of the material has different characteristics for different frequency bands. Only accurate and up-to-date data can result in an accurate simulation.
3	Source of excitation	The type of the excitation port has to be chosen carefully. A waveguide port may give the most representative result but with less flexibility. Moreover, the size of the port has to be chosen with care and verified with an analytical theory.
4	Environment	The background material can influence the radiation pattern and input impedance. Objects that are placed near the measured structure may derail the result.
5	Discretization error	The trade-off has to be taken for long and accurate simulation or short and less accurate simulation. The electromagnetic fields have to be sampled sufficiently in space, while the Courant stability criterion demands the time discretization proportionally to the space discretization.
6	Truncation error	Time domain signals inside the simulation environment ideally decays to zero after some time since the excitation pulse is applied through the port. -30 dB decay can give accurate result to the scattering result. However, radiation pattern result requires -40 to -35 dB decay to give precise results.
7	Interpolation error	There always exists this error due to the calculation of the field values at location other than the grid edges.
8	Boundary condition	For simulating radiating structure such as an antenna, open space with perfectly matched layer (PML) at center frequency is recommended. This is to prevent the reflection of the electromagnetic field at the simulation environment's boundaries.

The frequency domain simulation is suitable for the domain problem with many conductors and meticulous structures, whereas the time domain simulation is suited for the domain problem with a large dimension consisting of dielectric materials or free-space. Therefore, the antenna design in Chapter 2 is solved in time domain whereas the RF MEMS switch design in Chapter 3 is solved in frequency domain. The combined problem of those as in Chapter 4 can only be simulated with a special treatment. This is mainly because a large resource, i.e. time and memory, is required.

In addition to the solver choice, some other issues have to be taken into consideration. Since the nature of a numerical model to represent the real electromagnetic behavior exhibits some errors, careful treatment has to be taken when simulating an antenna design. Some of the errors and inaccuracies including the prevention are shown in Table 2.4.

To have a believable simulation result, the choice of the stop criterion is important while at the same time, the simulation time shall not take very long duration. As mentioned in Table 2.4 point 6, -40 dB energy decay can provide precise simulation results, e.g. for both the gain and the S-parameter results. Figure 2.16 (a) gives an example of this that the energy in port 1 and port 2 (of two ports simulation) has decayed to -40 dB thus the simulation is stopped. Thereby, the duration of about 3.5 ns of the EM wave inside the problem domain has been simulated. It is counted from the first wave incident in the excitation port.

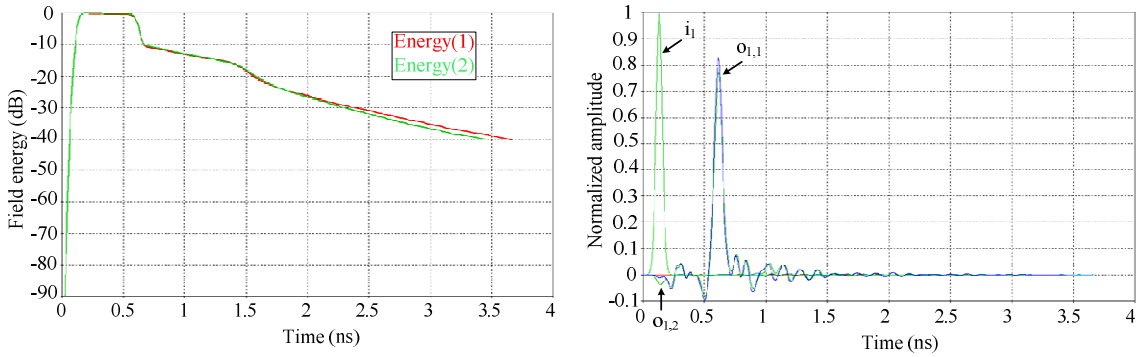

(a) (b)

Figure 2.16. Stop criterion of the transient simulation: (a) The field energy decaying over time in the simulation environment and (b) recorded incident and scattered signals over time in several simulation ports.

Figure 2.16 (b) shows the recorded incident and scattered signals over that duration for two port simulation. The reflection of the wave signal from the antenna structure and also from the feeding structure can be investigated in detail. For instance, at 0.6 ns a large amount of the reflected time signals ($o_{1,1}$) is observed at the port. This time signal is then transformed into frequency domain to obtain the S-parameter result. A multiple of reflection is also observed around that time which is mainly due to the transmission line structure. i_1 is the incident wave at the port which has a Gaussian shape. What frequency components are

included in this time signal depends on the shape and width of this Gaussian pulse. $o_{1,2}$ is the recorded mutual coupling from port 2 to port 1, when only port 2 is excited.

2.7 Antenna characterization

In this section, the final design of the antenna will be characterized. The two types of the antenna that will be shown differ in their inter-element angular distance (θ_{el}). The characterization includes the scattering parameter or the S-parameter and the realized gain performance. The realized gain includes the impact of the return loss in its gain measurement in addition to the dielectric loss, while the gain (IEEE definition) only accounts the dielectric loss. Obviously, both consider the directivity of such a structure. The directivity does not incorporate both the dielectric and the return losses.

2.7.1 Array structure with 40° inter-element angular distance θ_{el}

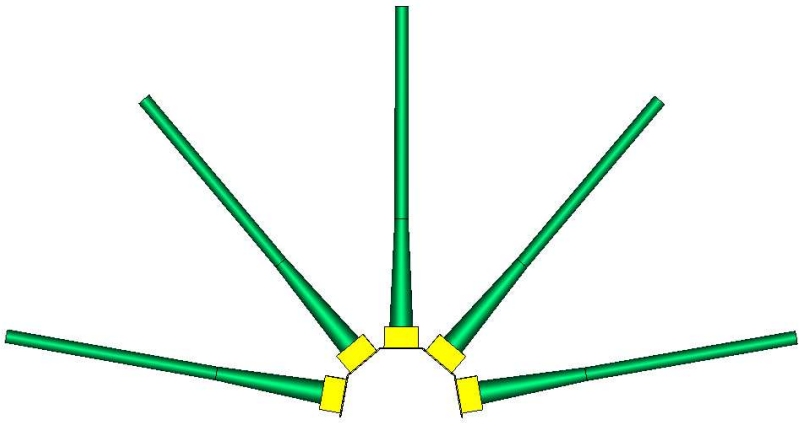

Figure 2.17. Rod antenna array with θ_{el} = 40°.

After the design iteration and the optimization in section 2.2 and 2.3, respectively, have been performed, the dimension for the final structure is obtained. The first characterization will be done for the rod antenna array with 40° inter-element angular distance (θ_{el}) (see Figure 2.17). Later on, after observing the radiation pattern for different θ_{el}'s, the suppression level about where the main lobe of the neighboring elements overlaps can be determined. Figure 2.17 is the same as Figure 1.3, but it is shown again here for the sake of completeness.

The optimized dimensions of the single-element rod antenna are shown in detail in Figure 2.18. The diameter of the circular patch ($Ø_{cp}$) is 1.524 mm. Unless otherwise specified,

the dimension's unit in this design report is millimeter (mm). The diameter of the rod tip ($Ø_{rt}$) is 1.64 mm. The inner diameter of the waveguide has to be similar to the diameter of the tapered rod at its bottom end, namely $Ø_{wg}$ = 3 mm. However during the manufacturing, the machining accuracy to fit those two structures is important. The machining accuracy will be discussed in Chapter 5. The lateral waveguide's dimensions (d_{wg} x d_{wg}) are 3.7 x 3.7 mm^2 while the LCP plane's dimensions are 4 x 5 mm^2 (d_{lcp1} x d_{lcp2}). The waveguide dimension has to allow to be machined conveniently, especially at the part where the waveguide wall is thin. This LCP dimension is designed in such a way that enough space for bending exists between the neighboring antenna elements. Furthermore, in section 2.8 the mutual coupling for different distances between antenna elements is discussed. The strip width (w_s) and the gap width (w_g) are 0.348 and 0.036 mm, respectively. The 50-Ω characteristic impedance of a CPW transmission line on the LCP substrate is obtained using those dimensions. The CPW's feed point below the patch is optimized to obtain an antenna's input impedance Z_{in} ~ 50 Ω in the 60-GHz band. The via diameter ($Ø_p$) is 0.2 mm, which has to be small enough but can still be manufactured. The smallest possible diameter to build such a via is 0.1 mm at QPI, Helmond [89].

Dimensions along the *z*-direction of the antenna structure are illustrated in Figure 2.18(b). The height of the cylindrical rod (h_{cr}) is 25 mm (or 5λ), and the height of the tapered rod (h_{tr}) is 15 mm (or 3λ). The waveguide or launcher has a height (h_{wg}) of 2.5 mm (or 0.5λ). Finally, the thickness of the LCP substrate (t_{lcp}) is 0.16 mm.

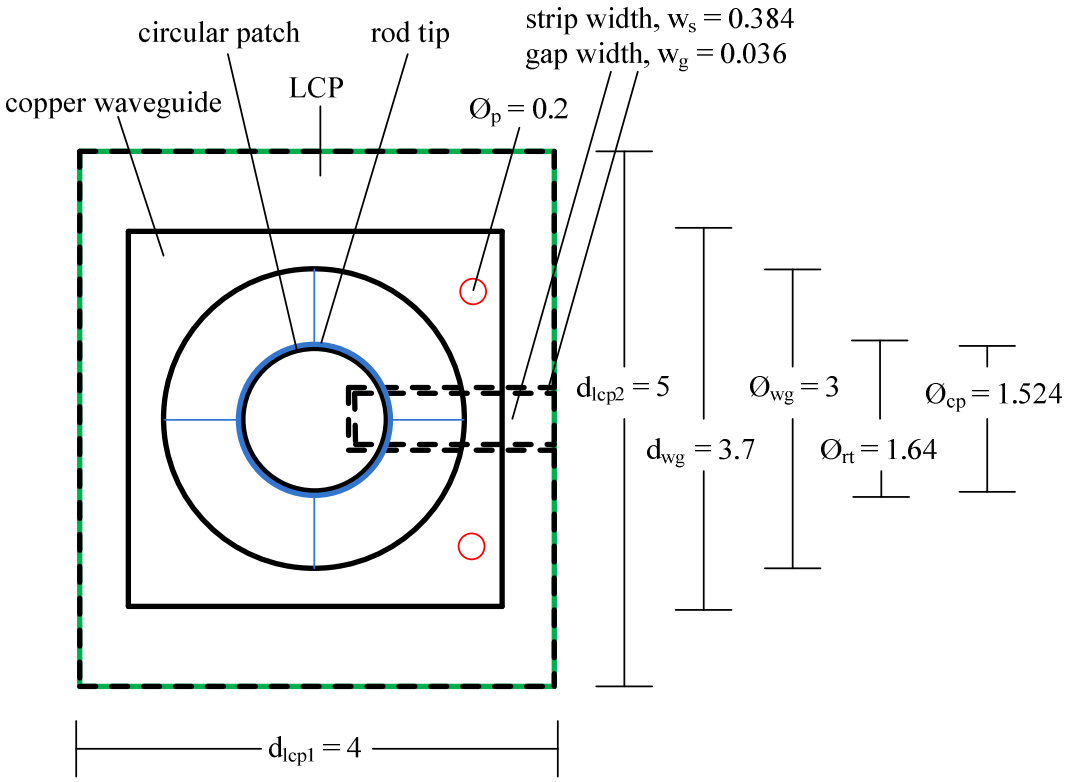

(a)

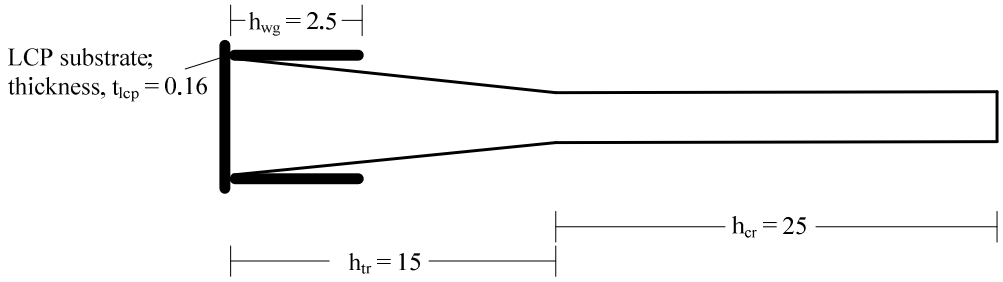

(b)

Figure 2.18. Dimension of the single-element rod antenna: (a) bird's-eye view, and (b) cross-sectional view.

2.7.1.1 S-parameter

One of the most important antenna characterizations is its S-parameter. The S-parameter can be S_{11}, S_{21}, and so forth. S_{11} is the return loss of the measured device in dB. This value is the ratio between the scattered wave observed in the port 1 and the incident wave observed in the port 1. S_{21} is the mutual coupling for most of the antenna configuration, or it can be the insertion or the isolation loss for the RF MEMS configuration. Also, S_{21} is the ratio between the scattered wave observed in the port 2 over the incident wave observed in the port 1. Only one port is excited by the time signal at a time, and the other ports are terminated with a matched load, e.g. 50 Ω. In this example, only port 1 is excited. With this knowledge, the S-parameters in Figure 2.19 can be analyzed. In this array structure, S_{11}, S_{22}, and S_{33} are the return loss for the upright rod, the 40°- tilted rod, and the 80°- tilted rod, respectively. The other two antenna elements are not simulated here, because they are symmetrical and will exhibit same performances.

The dips at the 60-GHz band are the minimum return losses for all three ports. A slight difference of the return loss results at the 60-GHz frequency band is because each single element of the array structure is meshed with a different number of finite hexahedrons. The tilted antenna element may be differently represented by hexahedrons in comparison with the upright antenna. Nonetheless, the resulting return loss for those three antenna elements is good and comparable. This is important to design an antenna system with a less return loss or reflection because more power transferred is much preferred. In addition, a reflection towards the source, which is usually RF front-end electronics, is unwanted because this reflection will distort the quality of the signal transferred. The mutual coupling for the furthest antenna elements is around -50 dB, whereas it for the closest one is around -47 dB at 60 GHz, which is considered very low. The relatively high mutual coupling for $f_o \gg 60$ GHz or $f_o \ll 60$ GHz is mainly due to the reflected wave that couples to the neighboring port.

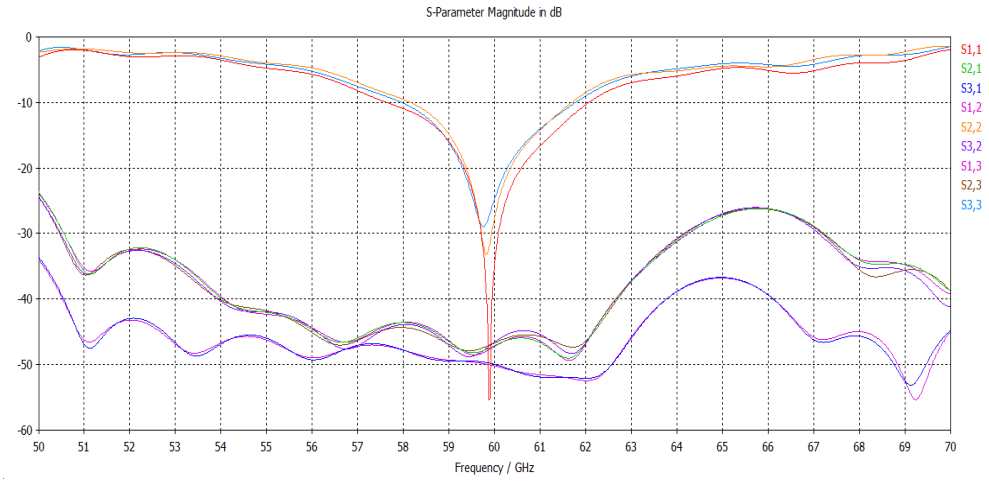

Figure 2.19. S-parameter over the frequency band of the dielectric-rod antenna array with θ_{el} = 40°.

The -10 dB bandwidth is approximately 4 GHz. Note that this value is similar to the result in Figure 2.6 in spite of the different material for the rod structure and the different substrate thickness. Previously it was a Kapton rod (ε_r =2.8) with t_{lcp} = 0.12 mm and now it is a PS rod (ε_r =2.53) with t_{lcp} = 0.16 mm. A higher ε_r usually produces a higher bandwidth, but now it is compensated by thicker LCP substrate for the PS rod case.

2.7.1.2 Radiation pattern

The radiation pattern of the antenna in Figure 2.17 is depicted in Figure 2.20. This pattern is simulated for the 60-GHz operation frequency of the rod antenna. The measured value is the realized gain. As mentioned earlier, the realized gain accounts both the return and the dielectric losses. In addition, in this CST MWS™ simulation, the conductor loss and the surface wave are included in the calculation as well. Note that the depicted patterns here are for the antenna operated in switched-beam.

The result clearly shows that the required characteristics of relative constant HPBW and realized gain, and beam symmetry are relatively uniform for each array element. The realized gain is around 18 dBi, where a slight different magnitude is due to the different meshing in the simulator as mentioned earlier. Nevertheless, this value is small, i.e. ±1dB. The sidelobe level is around – 13dB. A slight larger SLL for the middle lobe is due to the presence of the neighboring rod elements. During the simulation, to reduce dramatically the simulation time, the symmetry of the structure can be exploited. The HPBW is around 22° which meets the specification mentioned in section 1.5.2. The beams of the neighboring elements overlap at about -15 dB suppression level. This situation will result in gaps inside the scan range. Furthermore, the upright and the 80°- tilted rod has their beams overlapped at -20.5 dB suppression level.

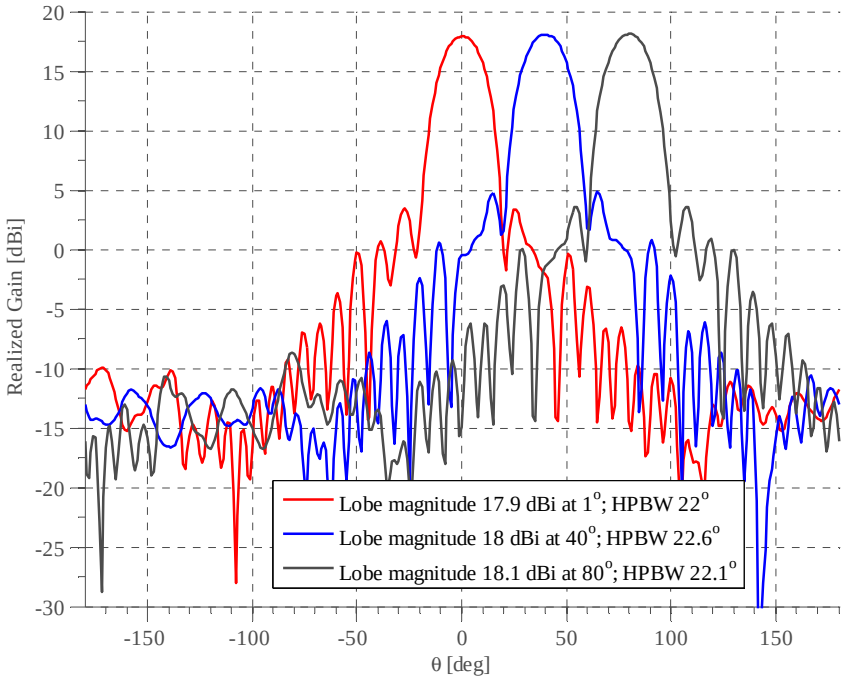

Figure 2.20. Radiation pattern of the dielectric-rod antenna array with $\theta_{el} = 40^{\circ}$.

To observe the beam symmetry, Figure 2.21 is provided. It is clearly observable that the beam is symmetrical, particularly for the main lobe. In conclusion, the pattern of a dielectric-rod antenna does not show a φ-dependence or is rotationally symmetric around the z-axis (of the rectangular coordinate system).

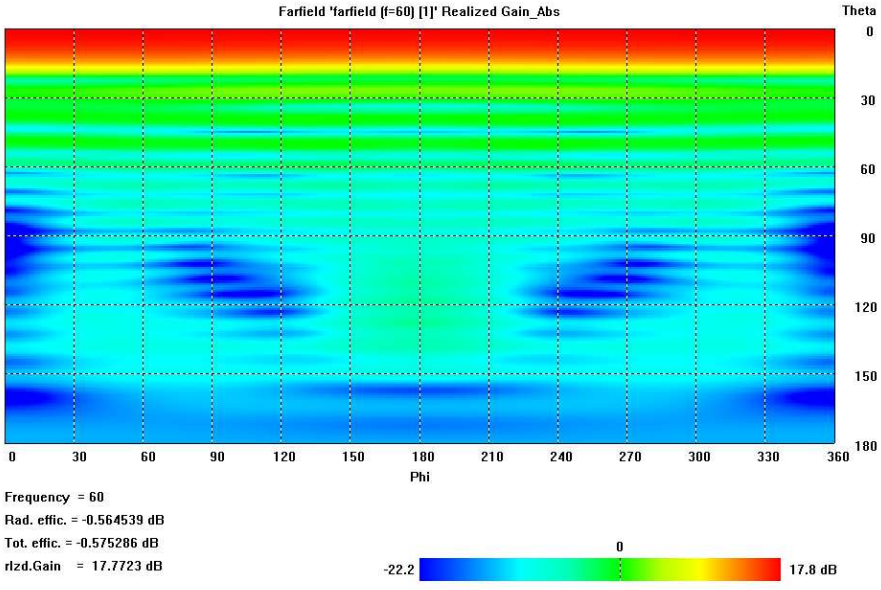

Figure 2.21. Two-dimensional radiation pattern of the rod element.

2.7.2 Array structure with 20° inter-element angular distance θ_{el}

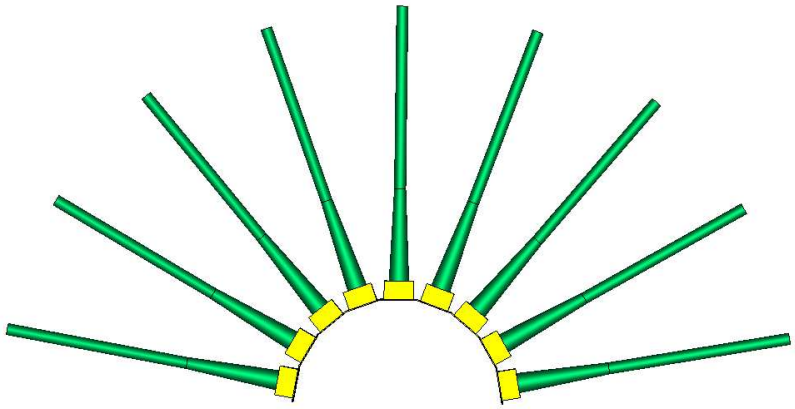

Figure 2.22. Rod antenna array with θ_{el} = 20°.

In Figure 2.22, the different array structure is presented. The 20° θ_{el} can be observed which results in 9-rod elements. The antenna characterization will be done, including the radiation pattern. It will be shown that the scan range may reach 180°.

2.7.2.1 S-parameter

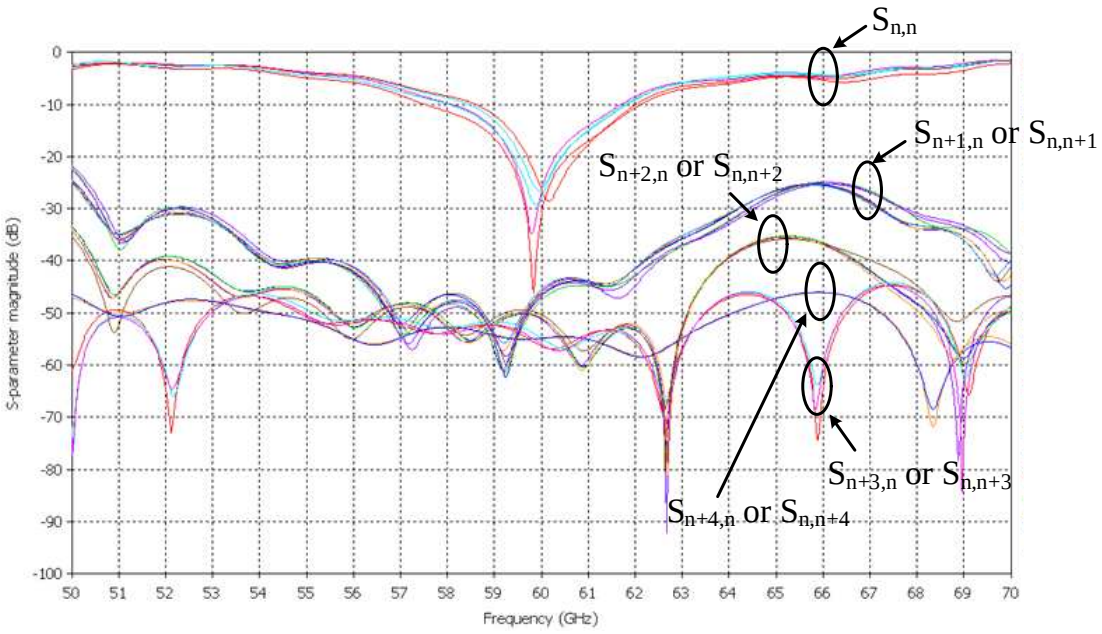

Figure 2.23. S-parameter over the frequency band of the dielectric-rod antenna array with θ_{el} = 20°.

In Figure 2.23, S_{nn} is the return loss of the antenna structure. Also exploiting the symmetry of the structure, only 5 of the antenna are simulated. Thereby, $n = 5$. The return loss compares with the previous case in section 2.7.1. The mutual coupling at the 60-GHz operation frequency for S_{21}, S_{31}, S_{41}, and S_{51} is: -45.896, -51.03, -54.858, and -54.815, respectively. However, their values are significantly small although there is an increase of the mutual coupling of about 2 dB for the neighboring antenna elements (see Figure 2.19). Later on, it will be proven that the isolation performance will be limited by the RF MEMS switch.

2.7.2.2 Radiation pattern

The corresponding radiation pattern for each array element can be seen on Figure 2.24. The realized gain is around 18.4 dBi which is larger than the result from $\theta_{el} = 40^{\circ}$. The meshing difference as mentioned earlier is the cause of the difference. The main lobe direction is observed for every element angle, θ_{el}, and the HPBW for all antenna elements is around 20°. In addition to the radiation pattern in $\varphi = 90^{\circ}$, the radiation pattern for $\varphi = 0^{\circ}$ is also included in the picture (see also Figure 2.1). Despite similar radiation performances, this radiation pattern has an additional 7 dB for $-140^{\circ} < \theta < -90^{\circ}$, i.e. a backlobe radiation. The discontinuity in the CPW line causes this backlobe radiation albeit it is only a small contribution. The effect of the CPW line sounds contradictory to one of its earlier purposes, i.e. the CPW's ground plane to reduce the backlobe radiation. However, with no CPW ground plane the backlobe radiation will increase. Therefore, it can be concluded that this small backlobe radiation is actually from the signal strip's discontinuity at the feed point.

The lobes from neighboring elements overlap at about -3 dB suppression level. There is no scan gap across the scan range. Continuous beam scanning across a broad scan range is possible by means of the conformal-rod antenna array with $\theta_{el} = 20^{\circ}$.

Figure 2.25 is presented here to investigate the pattern performance in a frequency band. The data are taken from the upright rod of the array. A frequency range from 59 to 61 GHz is being investigated; it can be observed that the realized gain is nearly the same. Hence, this can be also expected that inside the frequency bandwidth, the gain performance is similar. The HPBW may also be expected to have a similar value within the bandwidth of interest.

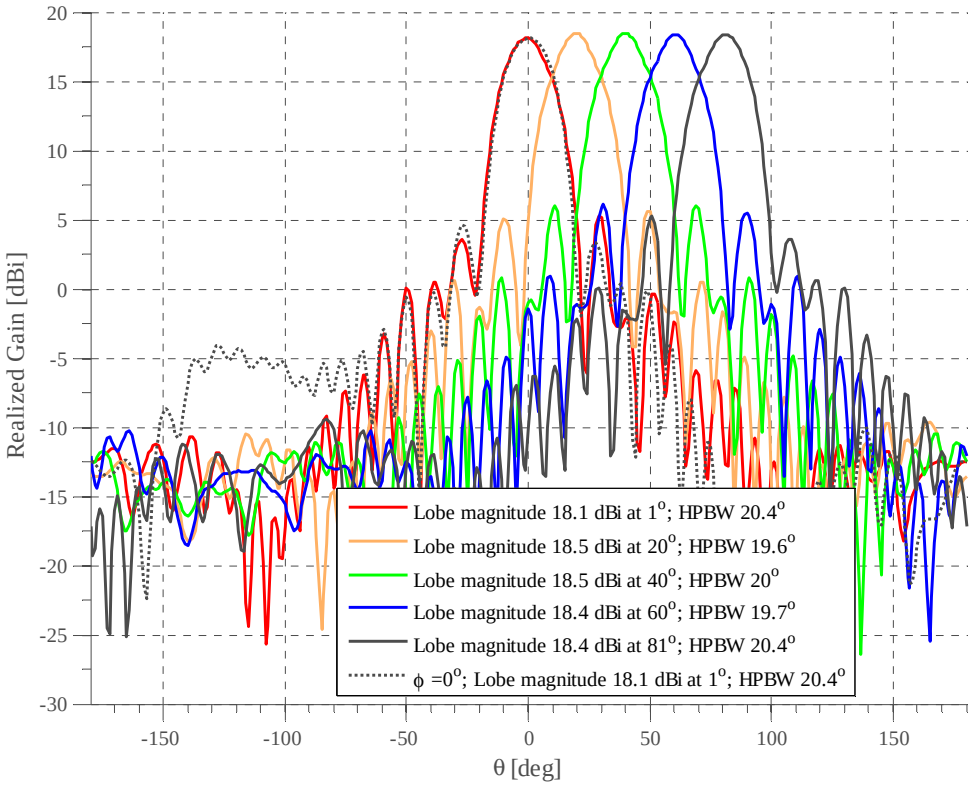

Figure 2.24. Radiation pattern of the dielectric-rod antenna array with $\theta_{el} = 20^{\circ}$.

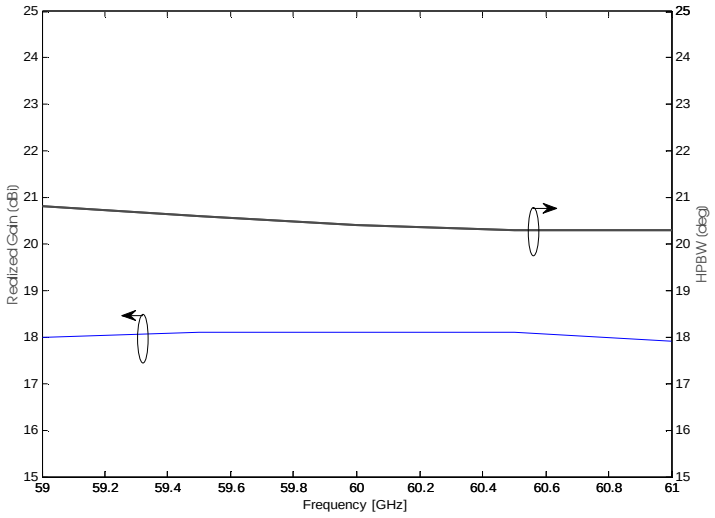

Figure 2.25. Typical realized gain and HPBW of the rod element.

To understand how the field propagates inside the rod, snapshots of the animation simulated using CST MWS^{TM} are shown in Figure 2.26. The snapshots are captured at 0.175 ns, 0.275 ns, and 0.35 ns. The electric field is animated for the array structure as in Figure

2.22 though due to the structure symmetry, only 5 elements are simulated. At the beginning of the simulation, a time signal is incident to the feeding port. This time signal contains a range of frequency components, and this time signal's magnitude has a Gaussian shape for the DC and lower frequency inclusions. This time signal then traverses the CPW feed line until it couples the circular patch. This patch resonates and thus radiates fields towards the *z*-axis. Now at 0.175 ns (see Figure 2.26(a)), the major part of the radiated field is shown in the end-fire direction, while at the same time a small backlobe radiation also occurs. The relative difference between the field that propagates towards the main lobe and towards the backlobe is around 26 dB, which is large enough to be negligible. Therefore, this dielectric rod antenna has a large front-to-back ratio.

At 0.275 ns (see Figure 2.26(b)), there are portions of the wave that are refracted inside the neighboring rod. This wave may be trapped inside the rod and thus radiates (i.e. increasing sidelobe level) or traverses the rod back to its port (increasing the mutual coupling). Obviously, the metallic waveguide can reduce the SLL and the mutual coupling since at the bottom-end, the amount of the rays with a low incident angle is large. These rays are usually refracted to the free-space earlier and couple to the next rod. However, the relative difference of the field magnitude for these weak rays to the field inside the rod core is around 26 dB. Finally at 0.35 ns (see Figure 2.26(c)), a locally plane phase-front wave radiates in the main lobe direction. These radiated waves contain all the frequency components of the aforementioned bandwidth.

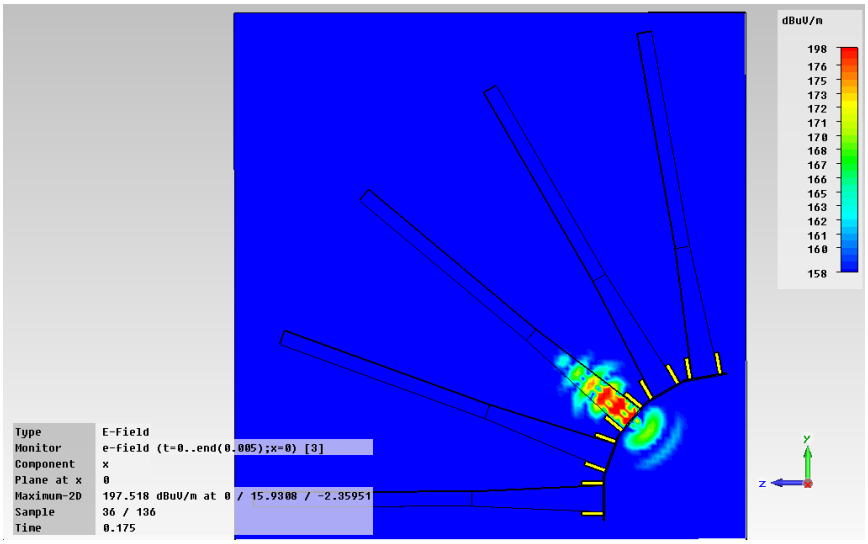

(a)

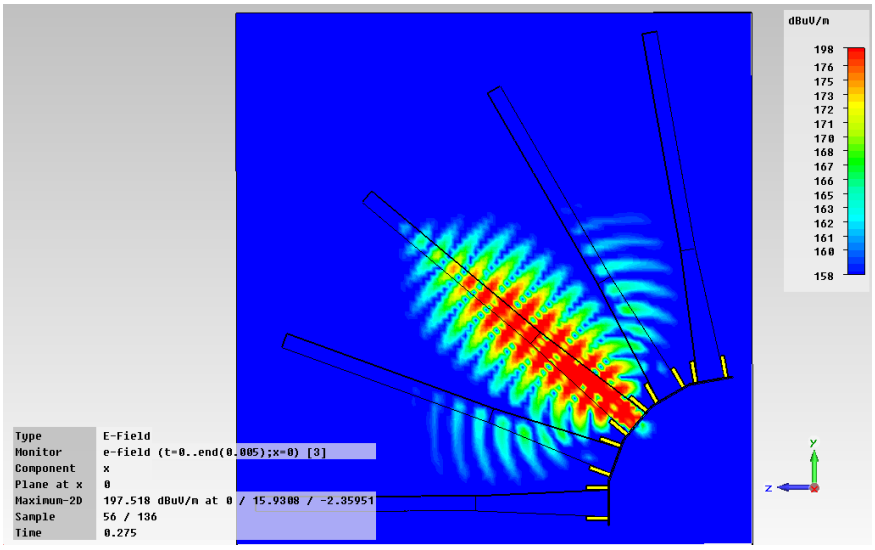

(b)

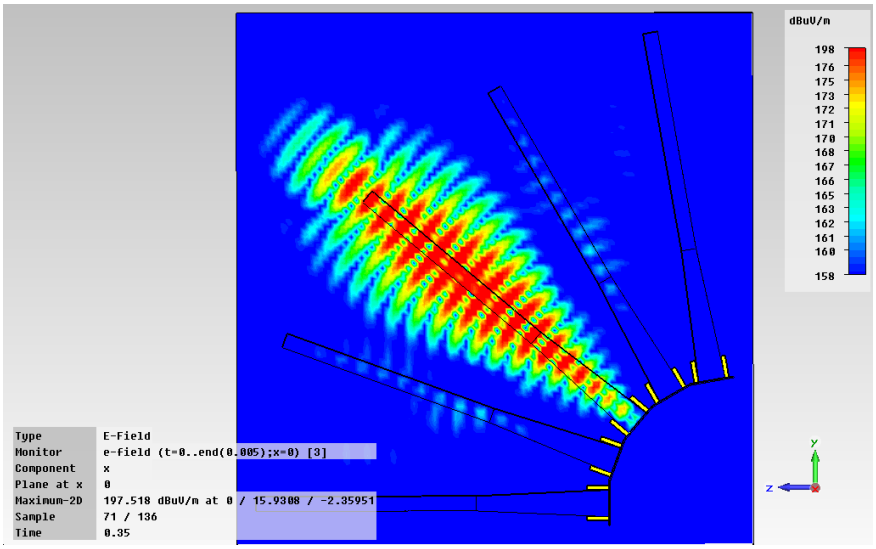

(c)

Figure 2.26. Snapshots of the electric field at (a) 0.175 ns, (b) 0.275 ns, and (c) 0.35 ns.

2.7.2.3 Polarization

The polarization of the antenna determines the polarization of the wave radiated by the antenna. In most communication systems, the radiated wave from an antenna has a linear, elliptical, or circular polarization. The polarization of a radiated wave is defined as the property of an electromagnetic wave describing the time-varying direction and relative magnitude of the electric-field vector, specifically, the extremity of the time-function vector

at a fixed location in space, and the sense in which it is traced, as observed along the direction of propagation [90].

The designed antenna is specified for a linear vertical polarization. Because of the feed position relative to the center of the antenna (see Figure 2.18(a)), the antenna has a polarization with a relative time-varying magnitude changing vertically as observed along the direction of propagation (see Figure 2.1). Also, the circular patch antenna is built for a linear polarization. Interested readers may find the information to excite a circular polarization in a circular patch in [91] and in a rod structure in [3] and [17].

The spherical coordinate system is utilized here to represent far-field components. Hence, the crosspolar (E_{cross}) and copolar (E_{co}) components are given by equation (2.28):

$$E_{cross} = \cos(\varphi)\, E_\theta - \sin(\varphi) E_\varphi \qquad (2.28)$$
$$E_{co} = \sin(\varphi)\, E_\theta + \cos(\varphi)\, E_\varphi.$$

Assumed that the tangential components are rotated by an angle φ (see Figure 2.28). Therefore for $\varphi = 0^\circ$, $E_{cross} = E_\theta$ and $E_{co} = E_\varphi$. Moreover to calculate the axial ratio (AR), the relationship is given by

$$AR = \sqrt{\frac{|E_\theta|^2 + |E_\varphi|^2 + |E_\theta^2 + E_\varphi^2|}{|E_\theta|^2 + |E_\varphi|^2 - |E_\theta^2 + E_\varphi^2|}}. \qquad (2.29)$$

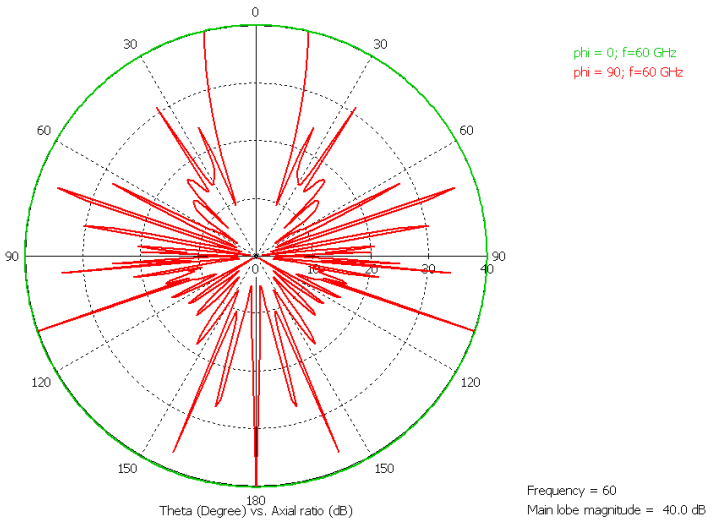

Figure 2.27. Axial ratio.

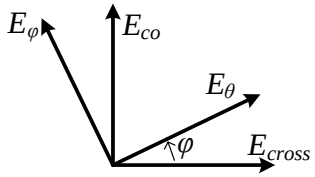

Figure 2.28. Far-field components for the spherical coordinate system.

Figure 2.27 shows the picture to measure the quality of a polarization excited by the rod antenna. The axial ratio (*AR*) is the ratio of orthogonal components of an electric field. It is observed that for φ=0°, the axial ratio is very large for all θ elevation angles (see equation (2.28)). This shows a good quality of the linear polarization of the rod antenna. Though ideally the axial ratio is infinity, 40 dB axial ratio is already very sufficient. For φ=90° and small θ's, the axial ratio is comparable to the result for φ=0°, whereas for large θ's the axial ratio is various. For certain θ, the axial ratio can be very small, e.g. < 3 dB, which in this case, a circular polarization may be excited, but only in that minor lobe direction (see Figure 2.21). Both results, i.e. for φ=0° and φ=90°, can also be observed in Figure 2.4. For φ=0°, the electric field vector has no component in the *y*-axis direction, whereas for φ=90°, the electric field vector has somehow components in both x- and y-axis direction which explain the variation of the axial ratio when is swept over θ. Moreover, the polarization result has been observed to be the same for the array structure in section 2.7.1.

2.7.2.4 Radiation efficiency

The radiation efficiency is the ratio of the power delivered to the radiation resistance to the power delivered to the resistance due to the radiation and losses [82][90]. The contribution for losses comes from:

- the conductor,
- the dielectric material, and
- the surface wave.

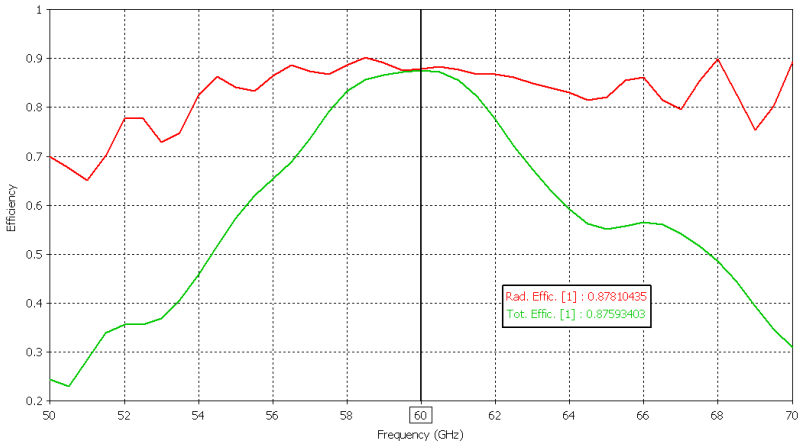

Figure 2.29. Radiation efficiency and total efficiency of the rod element.

Figure 2.29 depicts the total and radiation efficiency of the dielectric rod antenna. The total efficiency includes the impact from the return loss to the radiation efficiency. This is clearly observable that the total efficiency drops off when the return loss is larger than -10 dB

(see Figure 2.23). The total efficiency and the radiation efficiency are nearly similar at 60 GHz, i.e. around 87%, by virtue of the very low return loss at that particular frequency. This value shows that large portion of the power is actually delivered to the radiated field. Additionally, the radiation efficiency has been observed to be the same for the array structure in section 2.7.1.

2.8 Comparison of the mutual coupling of different array structures

An experimental study has been carried out on the mutual coupling of the dielectric rod antenna array. The mutual coupling is termed as S_{21} here as S_{21} is the ratio between the scattered wave observed in the port 2 over the incident wave observed in the port 1. Figure 2.30 displays the mutual coupling between two closest rods in an array configuration for different θ_{el}'s. For the simulation efficiency, without reducing the necessary accuracy of the result, the data are collected by simulating two rods only, instead of e.g. 9 elements of the rod. Figure 2.30(a) shows the mutual coupling for a frequency range while Figure 2.30(b) shows the mutual coupling for a particular frequency in this case the 60-GHz frequency band.

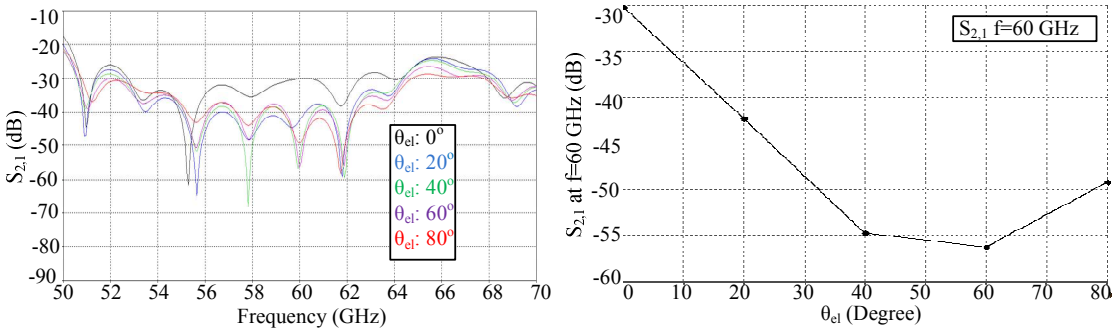

(a) (b)

Figure 2.30. Mutual coupling S_{21} between neighboring rod elements for different θ_{el}'s: (a) S_{21} magnitude over a frequency band and (b) S_{21} magnitude at 60 GHz.

From Figure 2.30(b), the mutual coupling decreases as θ_{el} increases until θ_{el} is around 50°. After this value, the mutual coupling tends to increase albeit with a small slope. This can be explained from the existence of the mutual coupling that also exists in the bottom region of the substrate. As a result of the θ_{el} increase, the power from the CPW feed line and the backlobe radiation may also couple to the neighboring port. However, the impact of those to the mutual coupling is very small for this antenna structure. Particularly for $0^{\circ} < \theta_{el} < 10^{\circ}$, the mutual coupling is observed to be relatively high.

Differently observed, the mutual coupling is investigated for different distances (d's) in Figure 2.31. This distance is defined as the distance from the metallic waveguide to the

substrate edge ($\frac{dlcp2 - dwg}{2}$) (see Figure 2.18(a)). Note that the result in Figure 2.30 is made with an unvaried d =1 mm, while the result in Figure 2.31 is made with an unvaried $\theta_{el} = 20^{\circ}$.

In Figure 2.31(b), it can be observed that for the touching metallic waveguides, i.e. d = 0, the mutual coupling equals -35 dB. When d increases, the mutual coupling becomes smaller until d is around 2 mm, and then it starts to increase and decrease again. This inconsistency can be explained by the constructive and destructive addition of the waves. The surface wave propagates inside the dielectric material as it is unintentionally guided or trapped inside that material. Hence, it depends on the size of the substrate, e.g. d. This surface wave propagates to the neighboring port and results in mutual coupling. Comparing Figure 2.30(a) with Figure 2.31(b), the contribution of the surface wave predominates when $\theta_{el} > 20^{\circ}$. For $\theta_{el} < 20^{\circ}$, the coupling that is caused by the radiation is more dominant. The coupling mechanism is that a radiated wave is refracted to the neighboring rod and is eventually observed in that rod's port. Of course, a portion of that refracted wave re-radiates and a portion is observed at the port.

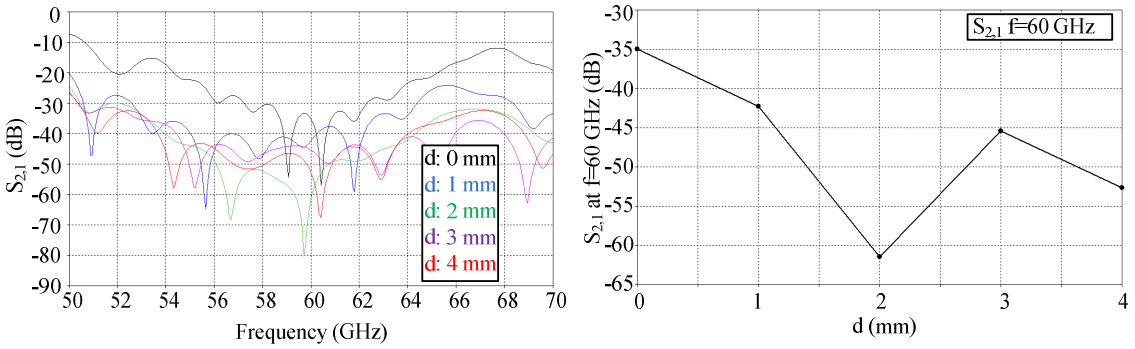

(a) (b)

Figure 2.31. Mutual coupling S_{21} between neighboring rod elements for different substrate extensions, d's. This distance, d, is measured from the waveguide edge to the substrate edge of the single-element antenna. (a) S_{21} magnitude over a frequency band and (b) S_{21} magnitude at 60 GHz.

As explained earlier, the mutual coupling is as a result of the constructive and destructive phase component of waves that is observed at a port. Therefore, this value looks fluctuating for different frequencies. Thereby, to see the necessary influence of the observed dimensions (e.g. θ_{el} and d), the average magnitude over a bandwidth may be more useful here.

Therefore, for the final design of the rod antenna at 60 GHz, $\theta_{el} = 20^{\circ}$ and d = 0.65 mm are chosen and used. The design consideration is to have a low mutual coupling, while at the same time, to have a small dimension for a conformal structure. This result has a good agreement with the result in Figure 2.23, yet a small difference exists because of different number of rod elements in the simulation, as mentioned earlier.

2.9 Design template

In this section, the design template can be used as a reference for dimensioning the dielectric-rod antenna according to the need. The template presented here is based on the performance of the antenna, a.o.:

- Directivity,
- HPBW, and
- SLL.

Based on those, one can fit the antenna dimension to the specification, e.g. as in section 1.5.2. In this general design template, no material's loss property is included in collected data. Therefore, the directivity value is used here. However, the design template for this project has been also included in this report to compare the influence of the material loss property in the template. This is provided merely for comparison and for easiness to decide the dimension when the PS material is used.

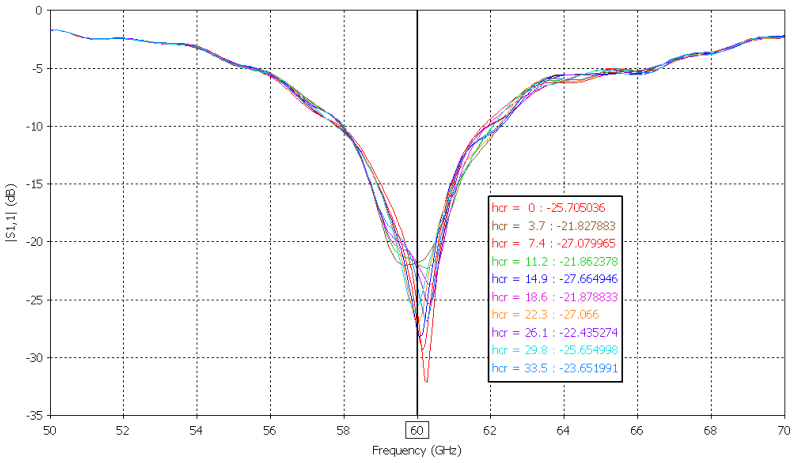

Figure 2.32. Reflection coefficient for different heights (h_{cr}) of the cylindrical rod.

First of all, the impact of different rod's height on S_{11} is depicted in Figure 2.32. Obviously, this does not largely shift the resonant point and still maintains a low return loss. The shape of the rod has been optimized, and its explanation is in section 2.3. The shape optimization reduces reflected rays inside the rod. The slightly different reflection performance of rays from the tip of the rod is responsible for different S_{11} performance as the cylindrical rod is varied. Nonetheless, when the length of the uniform cylindrical section of the rod is varied, no significant difference is observed here. This simplifies designers to use the design template without re-optimizing e.g. the feed point, etc.

Now the design template for particular material type, e.g. PS rod is shown in Figure 2.33. The height of the uniform section of the rod (h_{cr}) is varied between 0 – 33.5 mm. Figure 2.33(a) shows the gain for φ = 90° at the maximum direction (i.e. θ = 0°). The gain will

increase with increasing h_{cr}. Nevertheless, it can be expected that the gain will start to reduce after a point of a very large h_{cr}. The reason is that the waves may add destructively in the far-field region since within the rod, the phase velocity is lower than in free-space.

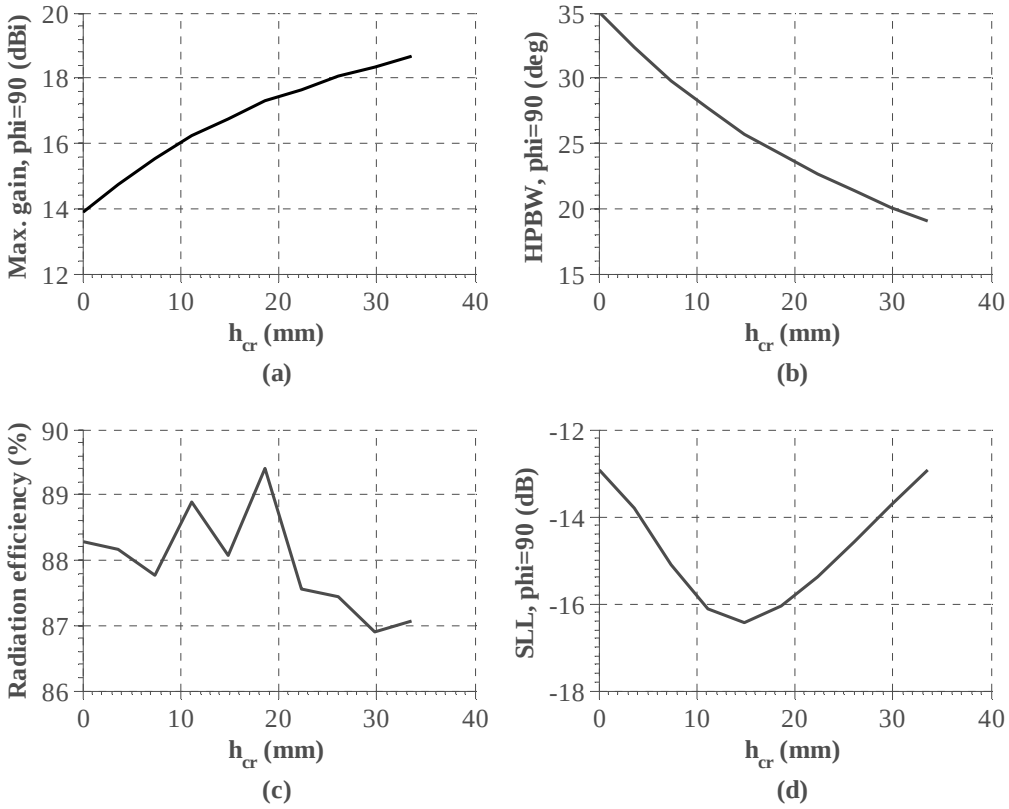

Figure 2.33. Design template for various heights of the cylindrical PS rod (h_{cr}) (see Figure 2.18(b)): (a) the gain (at $\theta = 0^{\circ}$) for $\varphi = 90^{\circ}$, (b) the half power beamwidth for $\varphi = 90^{\circ}$, (c) the radiation efficiency, and (d) the sidelobe level for $\varphi = 90^{\circ}$.

Figure 2.33(b), Figure 2.33(c), and Figure 2.33(d) show the HPBW, the radiation efficiency, and the SLL for the PS rod, respectively. Note that the gain value is used here instead of the realized gain value to have a fair comparison regardless the return loss as shown in Figure 2.32, yet if it is include, a very low return loss has a negligible impact in the final result.

The design template for the HPBW can be seen in Figure 2.33(b). This information is useful when the θ_{el} and the number of the conformal element need to be adjusted while maintaining the scan beam and the broad scan range. Moreover, its corresponding gain value can be obtained from Figure 2.33(a). Figure 2.33(c) is shown to observe the influence of the rod material's loss tangent (δ) and the incrementing rod's height to the radiation efficiency. Although the radiation efficiency is relatively the same, there is a tendency to have lower radiation efficiency when the height is incremented. The loss in the dielectric material starts to grow greater than the benefit that is obtained by increasing the rod's height.

Figure 2.33(d) shows that the SLL has its optimum value for h_{cr} = 15 mm. After that value, the SLL grows. SLL < -12 dB is considered good, though this depends on the specification and the application. For the design in this report, h_{cr} = 25 mm is being used to meet the specification in section 1.5.2.

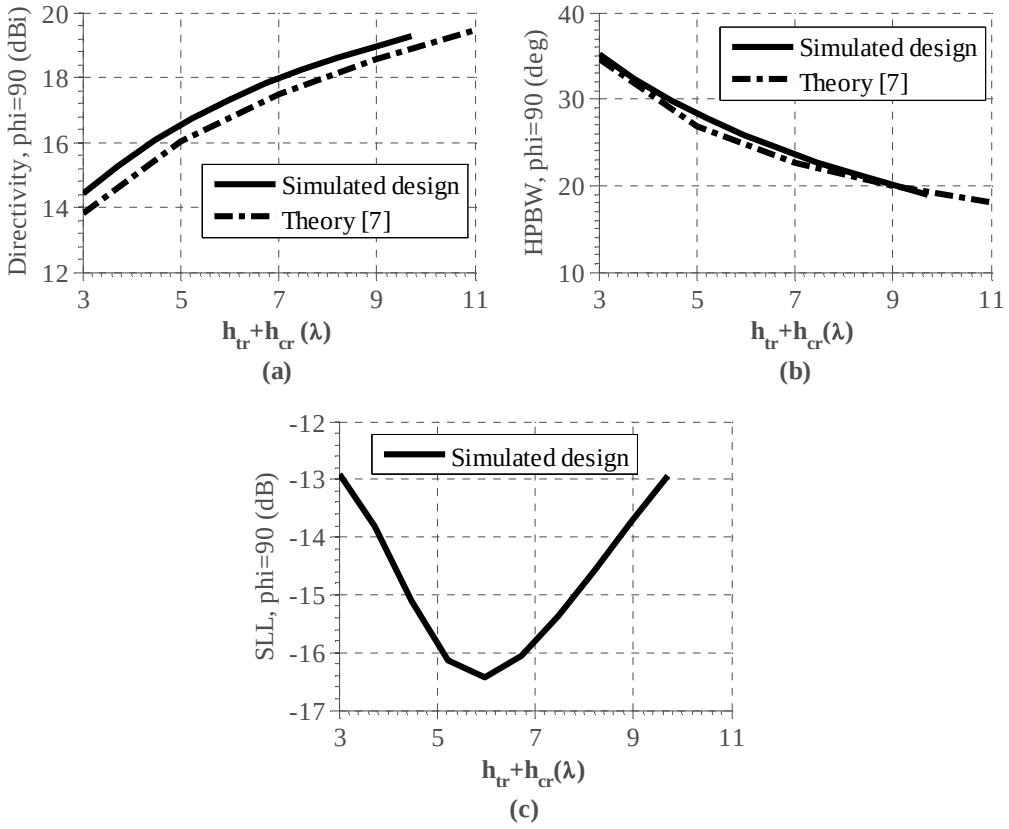

Figure 2.34. General design template for various heights of the cylindrical rod (h_{cr}): (a) the directivity (at $\theta = 0^{\circ}$) for $\varphi = 90^{\circ}$, (b) the half power beamwidth for $\varphi = 90^{\circ}$, and (c) the sidelobe level for $\varphi = 90^{\circ}$.

As mentioned earlier in this section, the general design template is given in Figure 2.34. With the measured performance disregarding the material loss, an influence of the material's loss to the performance can be investigated. Approximately 0.4 dB difference can be seen for gain and directivity values. In the HPBW and the SLL, this loss tangent of the material has no influence, which is predicted. Moreover, this design template is also applicable for various operation frequencies according to the requirement and specification.

The theoretical values for the directivity (see equation (2.5)) and the HPBW (see equation (2.6)) have also been included in Figure 2.34 for comparison. Both simulated performances have a good agreement with the theoretical approximation. About 0.4 dB difference between the theory and the simulation results for the directivity value is observed. This is because the simulated results have been obtained using the optimized shape. Thereby,

the simulated design gives better performance. This will be proven and verified through the measurement of the antenna demonstrator in Chapter 5.

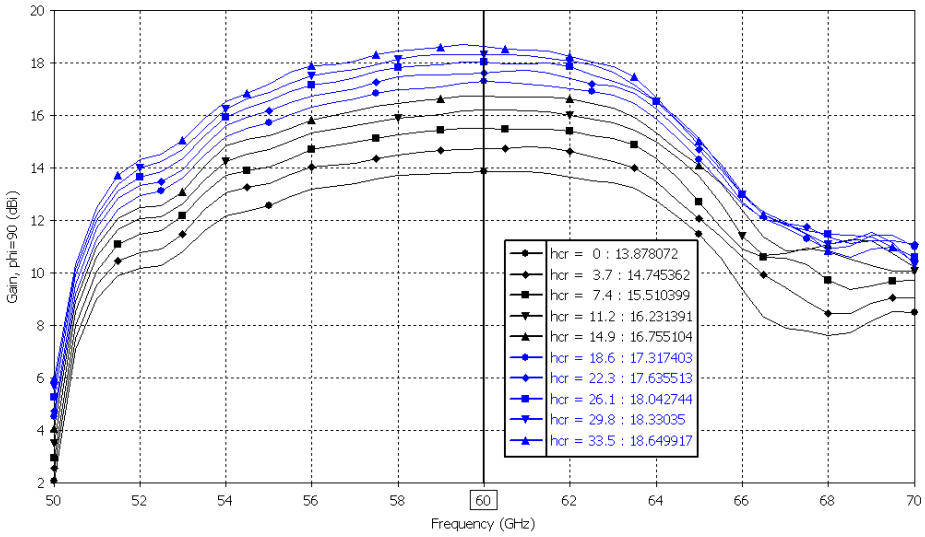

(a)

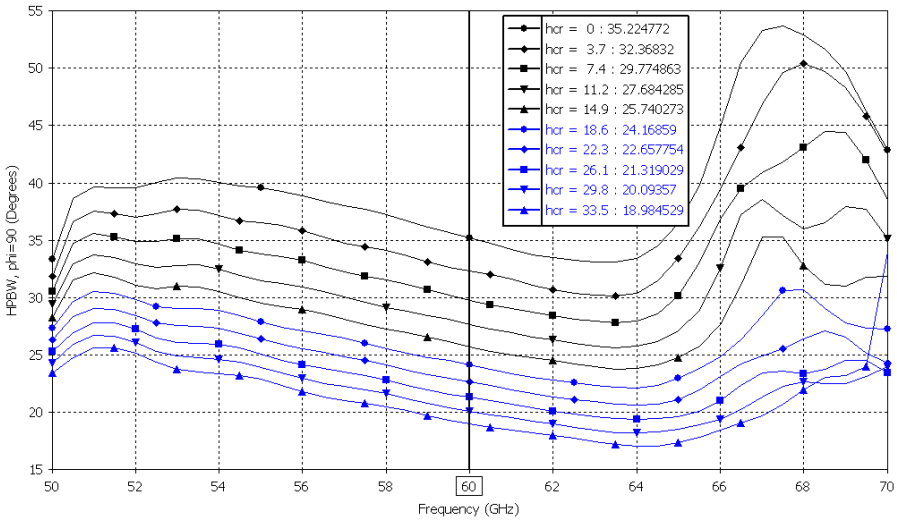

(b)

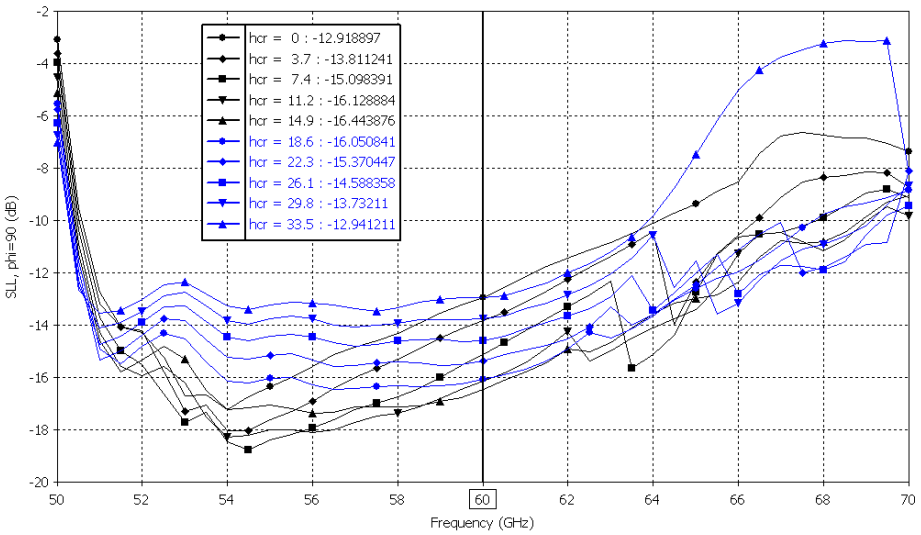

(c)

Figure 2.35. Broadband characteristics for various heights of the cylindrical rod (h_{cr} in mm): (a) maximum gain (at $\theta = 0^{\circ}$) for $\varphi = 90^{\circ}$, (b) half power beamwidth for $\varphi = 90^{\circ}$, and (c) sidelobe level for $\varphi = 90^{\circ}$.

Some pictures are also provided to see the broadband performance of the dielectric-rod antenna for aforementioned height increments. These are in Figure 2.35(a), Figure 2.35(b), and Figure 2.35(c) for the gain, HPBW, and SLL, respectively. The impact of the loss is included in the material here, i.e. based on the gain performance. Note that the design for the antenna in this report has $h_{cr} = 25$ mm.

From those figures, it can be concluded that the dielectric-rod antenna has nearly similar performances over the bandwidth of interest, in this case from 58 to 62 GHz. This also applies for all mentioned h_{cr} values. A minor remark is perhaps for the SLL in Figure 2.35(c) where a relative large variation (± 3 dB) over the bandwidth is observed, for $h_{cr} <$ 11.2 mm.

CHAPTER 3

3 Design of the RF MEMS switch in the 60-GHz frequency band

RF microelectromechanical systems (MEMS) switch increases its popularity since last decade [28]. It is because its higher performance than p-i-n diode and field-effect transistor (FET) switches. Pioneering applications up to 120 GHz for phased arrays and reconfigurable apertures in the telecommunication system and wireless communication have been realized using RF MEMS technology [26]. Wireless communication often uses RF MEMS to realize a single-pole N-throw (SPNT) switch in portable units and base stations. RF MEMS applications are not limited to these since emerging products in the area of automotive, health, instrumentation, defense, satellite, and multi-gigabit communication start to implement the RF MEMS technology in recent years [26].

MEMS switches utilize a mechanical movement to achieve a short circuit or an open circuit in the RF transmission line. Nevertheless, this does not imply that RF MEMS can only be employed at RF frequency. As aforesaid, MEMS implementations for millimeter-wave applications also gain much attention. The external force to achieve the mechanical movement can be obtained using electrostatic, magnetostatic, and piezoelectric. But for millimeter-wave applications, the electrostatic force is often used due to its high reliability and available manufacturing techniques [26].

Some advantages of the MEMS switch over p-i-n diode and FET switches are:

- Low power consumption: the electrostatic actuation may range from 20 – 90 V but does not consume current leading to very low power consumption.
- High isolation: the MEMS is miniaturized and fabricated to achieve low LC product using the available manufacturing techniques. The resulting resonance can provide high isolation in capacitive-shunt switches at millimeter-wave frequency.
- Low insertion loss: the off-state capacitance of the capacitive-shunt switch is very low due to miniaturized beam structure. This can lead to a low insertion loss.
- Good linearity: A mechanical device is a very linear device, and therefore, results in very low inter-modulation products.

On the other hand, considerations for designing the MEMS switch are:

- The cost: if the packaging is carefully planned in commercializing a MEMS product, its production cost will be significantly reduced because the major cost comes from the packaging of the MEMS. However, it is a big challenge to beat the cost of aforementioned diodes when it comes to include whole flows in commercializing the product, e.g. testing, packaging, and delivering.
- The speed: the choice of the beam material determines the switching speed, which is usually only in the order of µs. Nonetheless, counterpart diodes have reached the speed in the order of ns [96].
- Power handling: a MEMS switch cannot handle a high power with a high reliability. This is due to the self-stiction of the beam because of the high power signal. This self-stiction will also reduce the lifetime of the beam itself.
- The reliability: the challenge in the design of the MEMS structure is its switching cycles. The typical reliability of the MEMS switch is 10 billion cycles. Therefore, it is important to design a beam structure that can support a high reliability.
- The other consideration is the need to have a voltage up-converter chip to produce high-voltage drive (20-90 V).

These considerations will be discussed further in the subsequent sections of this chapter.

3.1 Background of the RF MEMS switch

In this section, the working principle of the RF MEMS switch will be explained. First of all, the RF consideration will be discussed, and then the electromechanical consideration will also briefly described. Moreover, the comparison between the ohmic-contact switch and the capacitive-shunt switch will also be discussed here.

3.1.1 RF considerations

Basically, the RF MEMS switch has two different types, namely the ohmic-series switch and the capacitive-shunt switch (see Figure 3.1). In this figure, the ohmic-series switch has the RF signal path in the left-right direction, whereas the capacitive-shunt switch has the RF signal path in the towards-away direction relative to the reader. The ohmic-contact switch normally works up to 10 GHz whereas the capacitive-shunt switch can work up to sub-millimeter-wave frequencies [30]. This is definitely why the capacitive-shunt switch is being used in this design project.

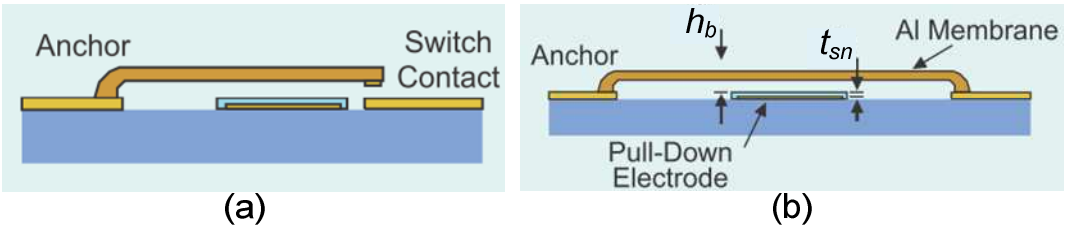

Figure 3.1. Cross-sectional view of (a) the ohmic-series switch and (b) the capacitive-shunt switch.

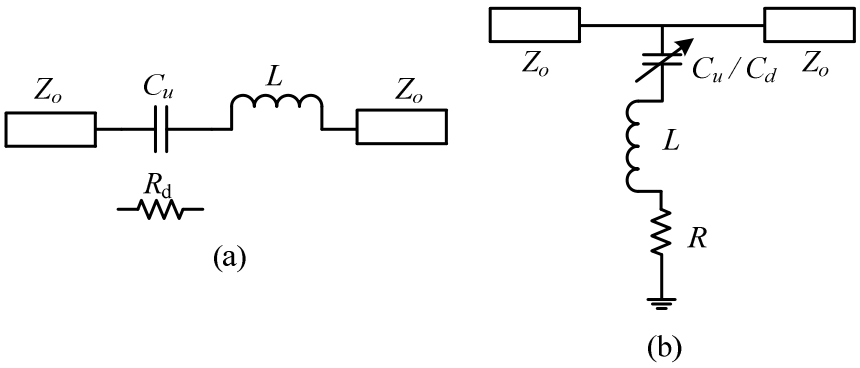

Figure 3.2. Circuit model of (a) the ohmic-series switch and (b) the capacitive-shunt switch.

The equivalent circuit of each MEMS type is depicted in Figure 3.2. The ohmic-contact switch hardly supports millimeter-wave frequencies due to its higher series resistance during its down state (R_d) which raises the insertion loss when the operation frequency gets higher. The isolation in this type of switch depends on the up-state capacitance (C_u), yet the high-isolation switch cannot be obtained for e.g. W-band applications (75-110 GHz) [27]. Perhaps, the high isolation can still be achieved by means of the cascade version of the switch but this then requires a large space. Consequently, this may also be an issue if a high-yield SPNT structure needs to be manufactured. Note that during the up-state position, the circuit exhibits the behavior of the pass-band filter. This proves that this device's isolation at

millimeter-wave frequencies is limited by how small the up-state capacitance is, whereas at, e.g., microwave frequencies, the isolation is not limited by this pass-band behavior. Also note that during the down-state position, the circuit exhibits the behavior of the stop-band filter, allowing the RF wave at microwave frequencies (i.e. lower than millimeter-wave frequencies) to propagate [66].

The capacitive-shunt switch is suitable for millimeter-wave applications because its capacitance is low in the up state (e.g. 10-50 fF). This can thus offer a low reflection coefficient as expressed in equation (3.1):

$$|S_{11}|^2 = \frac{\omega^2 C_u^2 Z_0^2}{4}, \tag{3.1}$$

where C_u is the up-state capacitance, Z_o the characteristic impedance, and ω the angular frequency.

A low up-state capacitance can be conveniently achieved by creating a small dimension of the beam, i.e. by trading off the surface area or the electrostatic force for a low up-state capacitance. However, the electrostatic force can still be improved by means of the higher actuation voltage and/or lower height of the beam (h_b). Note that in this up-state position (i.e. small C_u), the circuit (see Figure 3.2(b)) exhibits the behavior of the pass-band filter. On the other hand for the down-state position, the circuit with a high C_d (i.e. sufficiently larger than C_u) exhibits the behavior of the stop-band filter. The capacitance ratio, C_d/C_u, is one of the criteria to design a high-performance capacitive-shunt switch. The ratio value around 20-100 is acceptable for most designs [26] [28].

A low insertion loss (e.g. < 1 dB) is also realizable in this switch. This is because there is no induction and resistance in the up-state beam position owing to no metal connection. In the ohmic-series switch, the RF wave propagates when only there is metal connection giving a raise in the parasitic inductance and resistance. This contact resistance of the switch increases its insertion loss.

In the down-state position of the capacitive-shunt switch, the capacitance is higher now (e.g. hundreds of fF) but does not influence much the isolation except for the inductance [27]. This inductance has to be sufficiently low to achieve the high isolation at millimeter-wave frequencies. This isolation is expressed in equation (3.2):

$$|S_{21}|^2 \cong \begin{cases} \dfrac{4}{\omega^2 C_d^2 Z_0^2}, & \text{for } f \ll f_0 \\ \dfrac{4R_s^2}{Z_0^2}, & \text{for } f = f_0 \\ \dfrac{4\omega^2 L^2}{Z_0^2}, & \text{for } f \gg f_0, \end{cases} \tag{3.2}$$

where

$$f_0 = 1/\left(2\pi\sqrt{LC_d}\right), \tag{3.3}$$

where L is the inductance and R_s is the series resistance. It can be clearly observed that at the resonant frequency (f_o) the isolation is independent of the down-state capacitance and is limited by the series resistance of the beam material. This series resistance has to be low enough to give a high isolation at the resonant frequency. From equation (3.3), the resonant frequency of the capacitive-shunt MEMS switch is determined by the LC product. To compare this with the case for the series-contact MEMS switch, equation (3.4) is provided:

$$f_0 = 1/(2\pi C_u R_s). \tag{3.4}$$

From that equation, it can be seen that the resonant frequency is not inversely-proportional to the root-squared of the capacitance like in equation (3.3). Therefore, the capacitance needs to be very small, which requires a very small beam structure, if this ohmic-contact MEMS switch is intended for millimeter-wave applications. This may reduce the surface area and consequently reduce the electrostatic force that can be achieved. Moreover, the up-state isolation of this ohmic-series MEMS switch is expressed in equation

$$|S_{21}|^2 = 4\omega^2 C_u^2 Z_0^2, \tag{3.5}$$

which the isolation is proportional to the power of the angular frequency. This clearly gives much more challenge to build the ohmic-contact MEMS switch at millimeter-wave applications compared to the case of the capacitive-shunt MEMS switch in equation (3.2). Therefore, the capacitive-shunt MEMS switch is used in this design project.

In Figure 3.1(b), a t_{sn} thin silicon nitride (Si_3N_4) is deposited on the conductor strip to prevent the short contact between two electrodes. Consequently, the capacitance of the MEMS capacitor will be different for the up and down states dependent on the relative permittivity and the thickness of the dielectric material. Si_3N_4 has relative permittivity (ε_r) of 7.6 and loss tangent (δ) of 0.003. Its thickness is 0.15 µm which is sufficient enough to produce very high capacitance to give a high isolation for frequencies lower than the resonant frequency (see equation (3.2)). In addition, its loss tangent is also low which can facilitate low-loss wave propagation during the up state of the beam.

The formula in equation (3.2) can also be derived from the total impedance (Z_{total}) in equation (3.6):

$$Z_{total} = R + j\omega L + \frac{1}{j\omega C}, \tag{3.6}$$

where all the lumped element models are taken into account. The approximated formula of the total impedance for particular frequency range is thus:

$$Z_{total} \cong \begin{cases} 1/j\omega C, & \text{for } f \ll f_0 \\ R, & \text{for } f = f_0 \\ j\omega L, & \text{for } f \gg f_0 \end{cases} \quad (3.7)$$

where f_o is the resonant frequency; C, R, and L are the capacitance, resistance, and inductance. Finally, this Z_{total} determines the S-parameter magnitude, i.e. the isolation, insertion loss, and reflection of the MEMS switch.

Finally, in this RF perspective, the MEMS component behaves like a RLC circuit with negligible *R* and *L*. Thereby, the up-state capacitance, C_u, is given in [30]:

$$C_u = 1.4\frac{\varepsilon_o A}{h_b + t_{sn}/\varepsilon_r}, \quad (3.8)$$

where C_u is assumed to be 40% larger than the parallel plate value due to fringing fields. *A* is the area of the electrode under the beam. For the RF perspective, it is the area of the signal strip under the beam. Furthermore, the down-state capacitance, C_d, is given by:

$$C_d = R_A . \frac{\varepsilon_o \varepsilon_r A}{t_{sn}}, \quad (3.9)$$

where C_d is assumed as for the parallel plate value and there is no influence due to surface roughness (R_A) of the dielectric. In reality, the dielectric surface is not flat. In this case, R_A can be defined as e.g. 0.65.

3.1.2 Electromechanical considerations

The discussion in this section will be focused on the capacitive-shunt MEMS switch. The fixed-fixed membrane in this switch type is modeled as a mechanical spring, with an equivalent spring constant (*k*). This *k* is given by [34]:

$$k = 32Ew\left(\frac{t}{l}\right)^3\left(\frac{27}{49}\right) + 8\sigma(1-v)w\frac{t}{l}\left(\frac{3}{5}\right), \quad (N/m) \quad (3.10)$$

where *E* is the Young's modulus, σ the residual stress, and *v* the Poisson ratio of the beam material. The discussion in these parameters can be found in [97]. *l*, *w*, and *t* is the dimension of the beam as depicted in Figure 3.5, i.e. $l = d_{b1}$ = the length of the beam; $w = d_{b2}$ = the width of the beam; and $t = t_b$ = the thickness of the beam. The effective mass of the beam (*m*) is given in [30]:

$$m = 0.4\rho lwt, \quad (kg) \quad (3.11)$$

where ρ is the mass density of the beam material. Because the beam is fixed at both ends, the mass of the beam is reduced by 60%.

The actuation mechanism is obtained using the electrostatic force between the parallel plates in the MEMS structure. The electrostatic force is thus given by [26]:

$$F_d = \frac{QE}{2} = \frac{CVE}{2} = \frac{CV^2}{2\left(h + \frac{t_{sn}}{\varepsilon_r}\right)} = \frac{\varepsilon A V^2}{2\left(h + \frac{t_{sn}}{\varepsilon_r}\right)^2}, \qquad (N) \tag{3.12}$$

where Q is the electric charge, C the capacitance, E the electric field, V the drive voltage, h the instantaneous gap distance, and F_d the electrostatic force moving towards the down direction. For the electrostatic perspective, A is the area of actuation pads under the beam. t_{sn} is, as described in Figure 3.1, the thickness of the dielectric material (Si_3N_4) deposited on the conductor strip. The dominator in equation (3.12) is due to the fact that the materials between the parallel plates consist of air and Si_3N_4.

The electrostatic force produced from equation (3.12) is very low, but this is sufficient for MEMS-switch actuation. The reason is that, as the switch is pulled down to the bottom plate or electrode, the gap is reduced, and the pull-down force on the switch increases. However, there is still a pull-up force (F_u) due to the spring constant, k, of the switch. It is given by:

$$F_u = k(h - h_b), \qquad (N) \tag{3.13}$$

where h_b is the initial height of the bridge, and k is given by equation (3.10). Equating equation (3.13) with (3.12) will result in a cubic equation in h which gives a stable position. Subsequently, to collapse the switch to the down-state position, the pull-down voltage (V_p) is given by [26][30][97]:

$$V_p = \sqrt{\frac{8kh_b^3}{27\varepsilon_o A}}. \tag{3.14}$$

Moreover, the bias voltage necessary to hold down the voltage (V_h) is given by:

$$V_h = \sqrt{\frac{2k(h_b - t_{sn}){t_{sn}}^2}{\varepsilon_o A}}, \tag{3.15}$$

where h_b, as mentioned earlier, is the gap between the beam and the dielectric in the up-state position.

As discussed earlier, one of the important considerations is the switching speed. Therefore, the switching time (t_s) is defined as in the following equation [34]:

$$t_s = 3.67\ \frac{V_p}{V_s\sqrt{k/m}}, \tag{3.16}$$

where V_p is the pull-down voltage, V_s the drive voltage, k defined in equation (3.10), and m defined in equation (3.11). $\sqrt{k/m}$ is actually the resonant frequency, ω_o, of the second-order system [26]:

$$mh'' + bh' + k(h_b - h) = F, \tag{3.17}$$

where m is the mass of the beam, b the damping coefficient of the beam, and F the electrical force defined in equation (3.12). This second-order system follows the standard Newtonian's mechanics, specifically d'Alembert's equation of motion [26].

3.2 SP3T switch structure

The structure and dimension of the switch are pictured in Figure 3.3(a). Basically, the structure uses the 0/1-level interconnects and mainly uses FGCPW transmission line. 0/1-level interconnect has 0-level interconnection or via, which connects the MEMS's transmission line at one side with the transmission line at its opposite side, and 1-level interconnection or solder bump, which connects the transmission line to the motherboard with the MEMS chip.

The motherboard is the substrate for the antenna structure, i.e. LCP substrate. The 0-level interconnection is shown in purple circle, and the 1-level interconnection is shown in red circle in Figure 3.3. Their diameters ($Ø_{sb}$ and $Ø_{via}$) are 0.06 and 0.04 mm, respectively. These dimensions have to be small enough to support millimeter-wave frequency while not too small to be feasible to manufacture. Especially, the solder bump is difficult to apply in a very small dimension with a very high positional accuracy. The center distance between solder bump in the ground part (d_{sg}) is 0.23 mm, and the solder bump's distance between the signal and ground part (d_{ss}) is 0.15 mm. These measures are also similar and applied for the distance in the via case (d_{vg} and d_{vs}). These values are optimized with regards to the reflection performance and to keep the CPW main mode. All the ground widths (w_{gr}) are 0.453 mm which also fulfill the criterion in [91] to have a 50-Ω characteristic impedance of the conventional CPW.

While the motherboard substrate is a LCP, the substrate for the MEMS part is made from sapphire, which has a fabrication dimension (d_{sap1} x d_{sap2}) 2.3 x 2.59 mm^2. The LCP (in green color) is truncated in this figure. The complete structure of this LCP section has been displayed earlier in Figure 1.4. The sapphire material has a relative dielectric permittivity (ε_r = 9.4) and loss tangent (δ = 0.000158). Note that the orientation of the sapphire material influences in the ε_r value. For example, the cut along its optical axis has ε_r = 9.4 whereas the perpendicular one gives ε_r = 11.6.

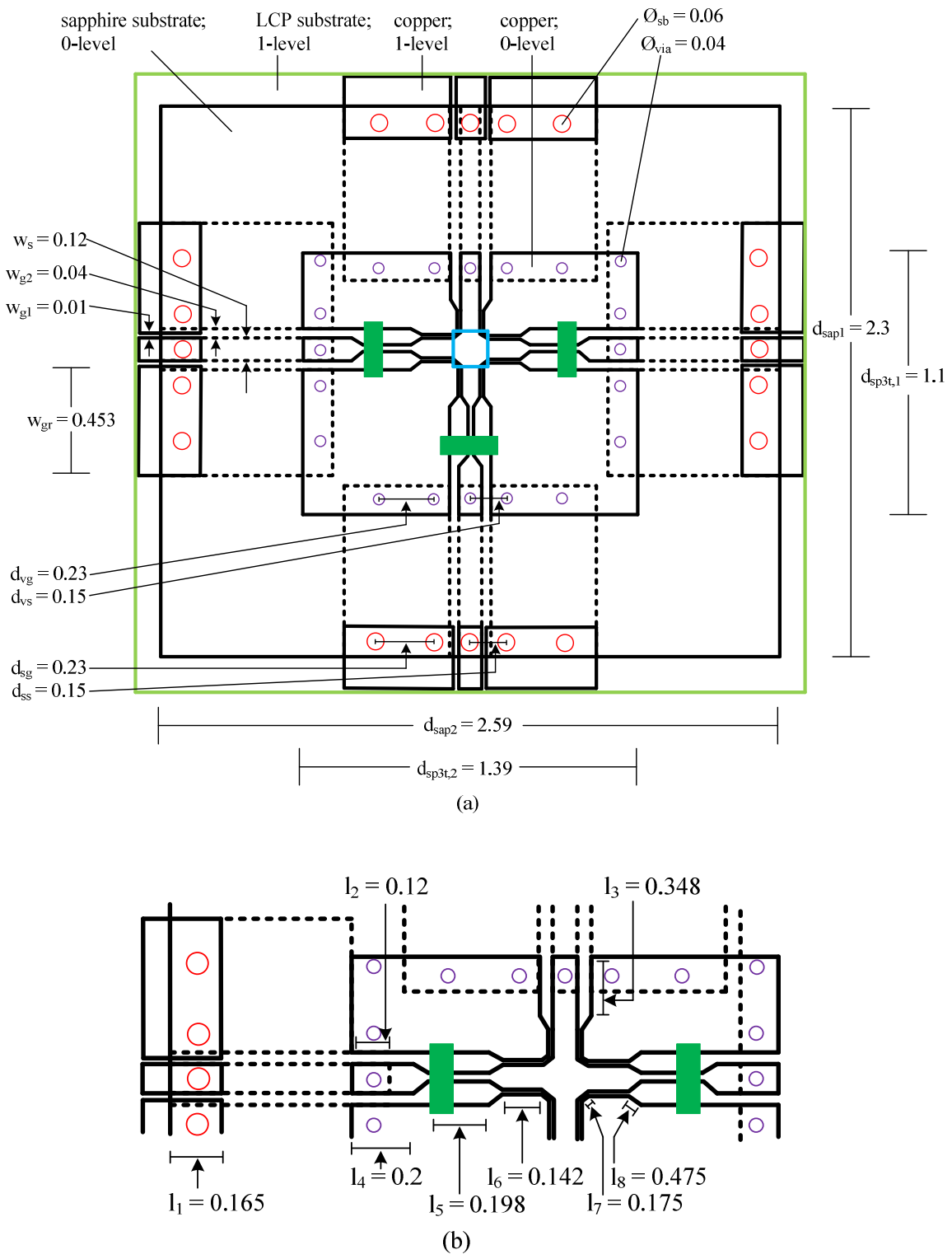

Figure 3.3. Structure and dimension of (a) the SP3T RF MEMS switch and (b) its detail in the close vicinity of the transmission line. The solid line represents the structure that faces towards the reader, while the dashed line represents the structure that faces away from the reader.

The high ε_r of the sapphire eases the design of the transmission line since the structure can be made relatively small, and especially for CPW, the gap (w_{g2} = 0.04 mm) can have a relatively wide width. This also means a positive factor for the manufacturability and repeatability of the MEMS fabrication. This gap width accompanied with the strip width (w_s = 0.12 mm) on a sapphire substrate can provide 50-Ω characteristic impedance of the transmission line. For the comparison, in the figure, the gap width (w_{g1} = 0.01 mm) on the LCP substrate has to meet to create the 50-Ω characteristic impedance of the line. All the signal and ground strips that are used in this MEMS design are made from copper with 2 µm thickness. This dimension is confirmed with the available manufacture capability.

The conductor in the MEMS part has the dimension of 1.1 x 1.39 mm^2 ($d_{sp3t,1}$ x $d_{sp3t,2}$). This comprises the ground and the signal strip and is on the 0 level. Through the via, these conductors (solid line) are connected to the conductor on the opposite or back side (dashed line) of the sapphire substrate. The beam of the MEMS itself is colored in green, and the air bridge is in blue around the SP3T's intersection (see Figure 3.5 and Figure 3.4, respectively).

The detailed dimensions of the transmission line are shown in Figure 3.3(b). The stub sections of the 1-level and 0-level interconnects (l_1 and l_2) are 0.12 and 0.165 mm long, respectively. These stubs are optimized to have a low reflection in the transition, namely the via and the solder bump. The line that goes to the single pole (l_3) in this SP3T is 0.348 mm long before the line has a transition to the line with a high shunt capacitance, i.e. narrow ground gap. This capacitive line (l_6 = 0.142 mm) has to match with the loading from the intersection in this capacitive-shunt MEMS SP3T. The transition itself should have a very low reflection when the width of the line is changed. The length of all the transitions (l_8) is 0.475 mm. The line's length that goes to every pole path (l_4) is 0.2 mm. The line for the MEMS section is made inductive with a large ground gap; this is to compensate the capacitive loading introduced by the parallel-plate structure of the MEMS when the beam is in the up-state position (i.e. signal flow). This line (l_5) has a length of 0.198 mm. The intersection structure has to provide a uniform performance for both the acute-angle arm and the straight arm. For this purpose, a compensation is made in the intersection by means of the chamfered ground with a length (l_7) of 0.175 mm. This will reduce the inductive loading which exists in the acute-angle arm and does not exist in the straight arm [66].

The air bridge dimensions are shown in Figure 3.4. The strip width (w_{s3}) and two gaps (@ w_{g3}) are spanned by 112 µm long (d_{ab1}) and 10 µm wide (d_{ab1}) aluminum air bridge. This CPW's strip is connected by a transition from a 70/30/70µm CPW. The thickness of this bridge (t_{ab}) is 1.5 µm, and it is positioned 8 µm high from the signal strip (h_{ab}). This air bridge is used for obtaining an equi-potential between surrounding ground strips, to prevent the excitation of modes other than the CPW's even mode [65] [66].

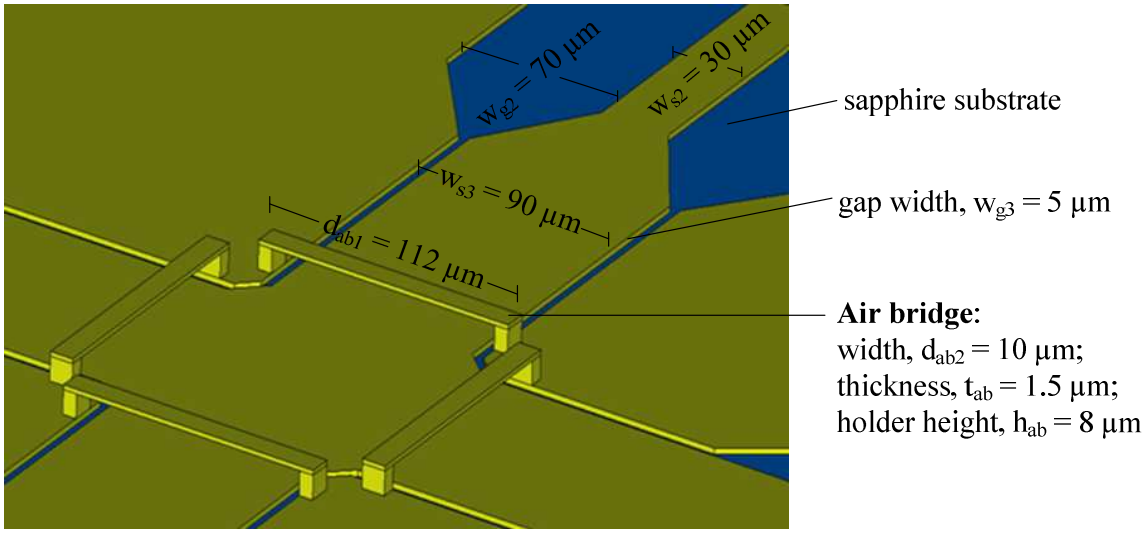

Figure 3.4. Structure of the air bridge.

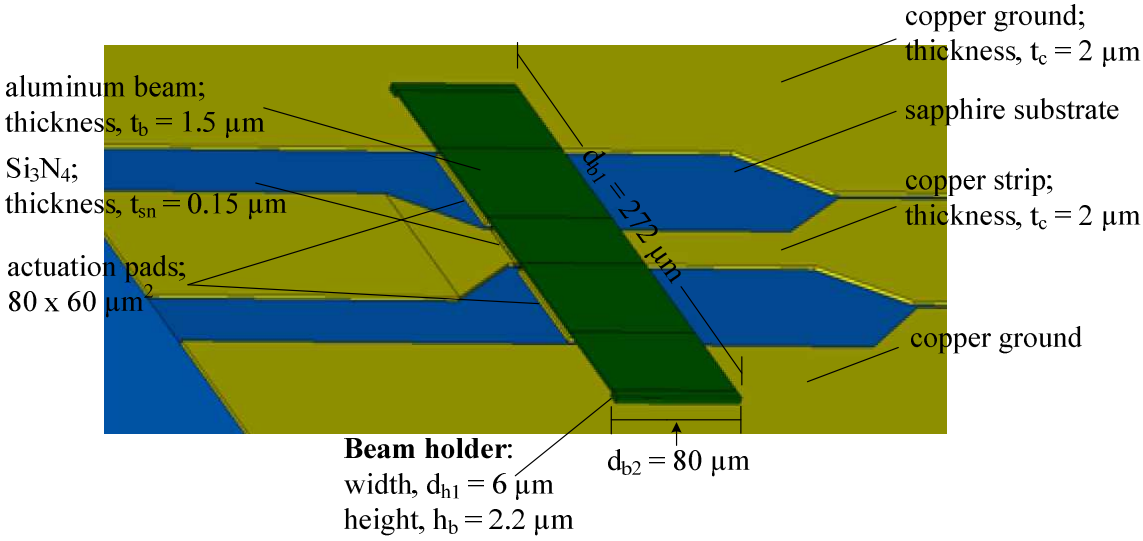

Figure 3.5. Beam structure of the RF MEMS on the CPW transmission line.

In Figure 3.5, the aluminum beam in green color is depicted in detail with its dimensions. The beam's length (d_{b1}), width (d_{b2}), and thickness (t_b) are 272 µm, 80 µm, and 1.5 µm, respectively. As mentioned earlier, a dielectric material made from Si_3N_4 is deposited on the strip conductor. Its thickness, t_{sn}, is 0.15 µm. The means for the actuation are two copper pads at each side with a dimension of 80 x 60 µm^2. In this design, the copper for the ground and signal strip has a similar thickness, t_c, of 2 µm.

The position beneath the antenna structure of the SP3T chip in Figure 3.3 can be seen clearly in Figure 3.6. The chip is colored in blue; the cap for the packaging is colored in transparent blue. The cap's height (h_c) is 200 µm and is made from the same material as the

substrate for the SP3T structure. This substrate itself has a thickness (t_{sap}) of 120 µm. From that cap's height, it provides 100 µm high of vacuum (cavity) space (h_c - t_c) where the SP3T or MEMS structure can be found. The solder ball or solder bump is made with an approximation of a cylinder structure with a diameter ($Ø_{sb}$) of 60 µm and a height (h_{sb}) of 30 µm. It is assumed that after applying a force in this solder ball (i.e. between the chip structure and the antenna's substrate), the pressure force will not change the solder ball's dimension. Also, note that this dimension has to be sufficiently small to provide broadband characteristic.

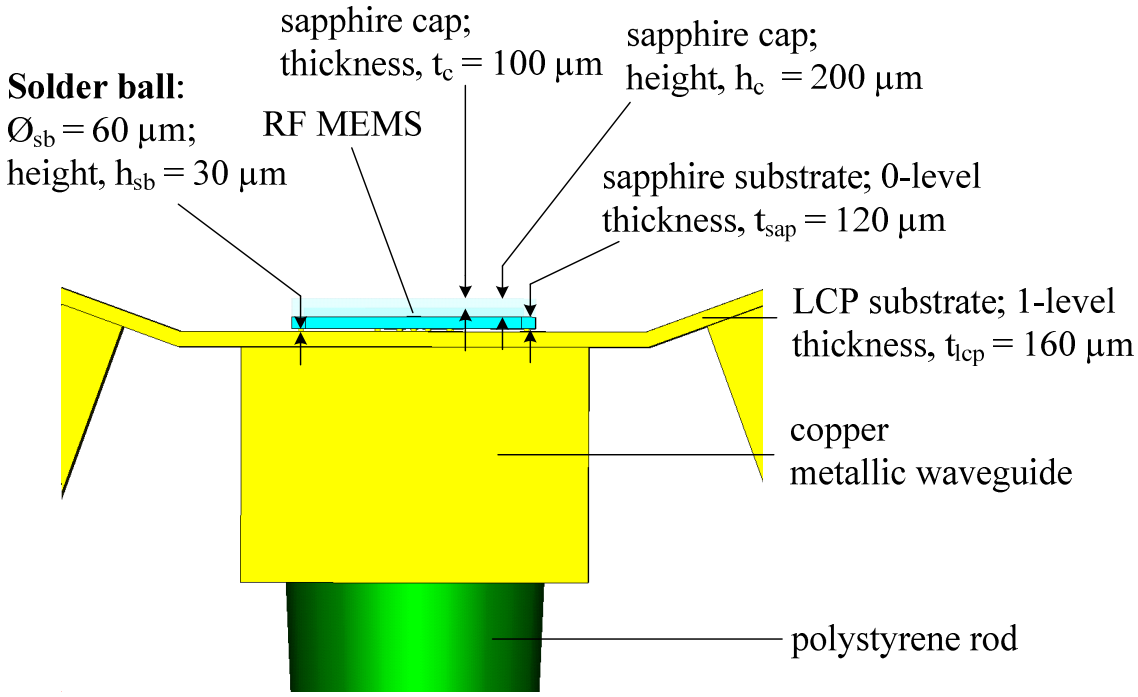

Figure 3.6. Side view of the SP3T.

In Table 3.1, parameters of the material for the high-frequency problem of the MEMS analysis are summarized. In this design project, sapphire is chosen for the switch's base substrate (and packaging cap) because of its mechanical robustness [57] and its very low loss tangent. Its relative permittivity is sufficiently large to be able to create a small structure of the chip and to reduce the radiation resistance of the switch structure. Last but not least, the chosen material has to conform to the available manufacturing technology of the material. For example, the manufacturing technology for sapphire and silicon is available at the known fab, e.g. Delft Institute of Microsystems and Nanoelectronics (DIMES) at TU Delft, whereas it is not the case for GaAs material. This condition is related to the technology flows that have to be followed to create the miniaturized structure, where each step requires certain advanced techniques, instruments, and measurement systems.

For electrostatic and mechanic problems, some material parameters are also summarized in Table 3.2. The material includes both the conductor and the dielectric or insulator. These materials are involved in the analysis and simulation of the respective problems.

Table 3.1. Material parameters for the high-frequency problem at 60 GHz.

	Relative permittivity, ε_r	**Loss tangent, δ**
Sapphire (Al_2O_3) [31]	9.4	0.000158
GaAs [31]	9.8	0.002
Silicon (Si)	11.9	0.004

Table 3.2. Material parameters for electrostatic and mechanic problems

	Young's modulus, *E* (GPa)	**Poisson's ratio, *v***	**Material density, ρ (kg/m^3)**	**Thermal conductivity (W/K/m)**	**Thermal expansion coefficient (1e-6/K)**	**Electric conductivity (S/m)**
Aluminum (Al) [51]	69	0.33	2700	237	23	3.56e7
Copper (Cu)	117	0.34	9000	401	17	5.8e7
Sapphire (Al_2O_3) [57]	345	0.28	4000	35	5.8	-
Silicon Nitride (Si_3N_4) [58]	2.8	0.27	3300	23	3.3	-

3.3 Transmission line, interconnection, and packaging

This section is meant as a supplement to the report of the transmission line structure in Chapter 2. The focus of this section is on the related structure that is being used in the design of the SP3T switch structure. The explanation for the CPW, or particularly FGCPW, itself can be found in Chapter 2.

3.3.1 90° CPW bend

In Figure 3.8, another aspect to design a CPW discontinuity, e.g. a 90° CPW bend, is pictured. Its equivalent circuit is in Figure 3.7 [94], where this right-angled bend produces G_s and C_s. This part of distributed elements increases the current flux density which occurs in the inner corner of the bend. C_p, L_s, and R_s represent the low-pass circuit that is generated for any discontinuity. To be able to operate at the high frequency band, the L_sC_p product has to be small. This part of distributed elements increases the electrical fringe field where the excess charge is accumulated. This can be solved by chamfered or mitered bend as shown in Figure 3.8. To minimize the impact of C_s and G_s, a slit can be made in the inner-corner of the bend. However, the manufacturability of such a structure is questioned, because at 60 GHz this slit dimension is very small. Therefore, the slit is not applied in this current design.

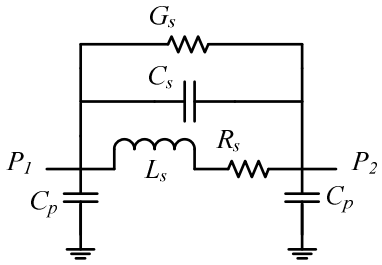

Figure 3.7. Two-port equivalent circuit of the 90° CPW bend.

Figure 3.8 compares the return loss for different chamfer factor for the signal strip's width of 120 µm. The chamfer factor is defined as in the picture that its multiplication with the strip's width determines the chamfer length. At 60 GHz, the chamfer factor of 1.483 is chosen as it has the optimum return loss (< -30 dB) for the frequency band. Its strip's manufacturability has to be taken into consideration as well.

This bend section with a chamfer factor = 1.483 introduces 0.58 dB loss at 60 GHz. Other values of the insertion loss for the corresponding chamfer factor in Figure 3.8 are summarized in Table 3.3. The shaded column is the chosen factor for the design. It can be observed that the chamfer factor of 1.88 may give slightly lower insertion and return losses but its manufacturability may also be risked due to the very narrow metal strip. Further discussion about the chamfered bend can be found in [35] and [93].

Table 3.3. Insertion loss of the chamfered bend in Figure 3.8.

Chamfer factor	0.675	1.079	1.483	1.88	2.292	2.697
Insertion loss (dB)	-0.584	-0.58	-0.581	-0.576	-0.587	-0.633

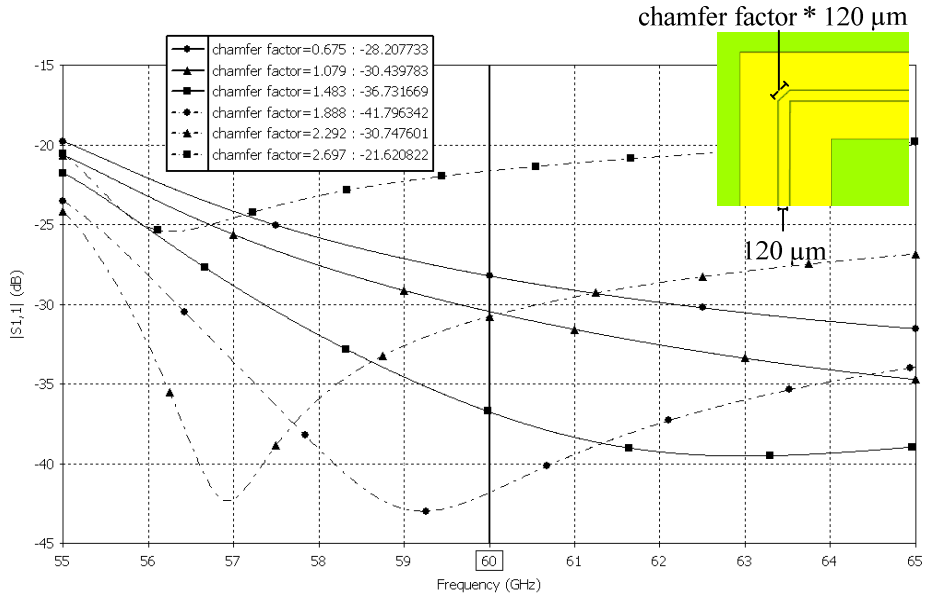

Figure 3.8. Characterization and optimization of the chamfered bend of the FGCPW transmission line.

3.3.2 Via, tapering, and SMA transition in CPW transmission line

To connect the conductor plane at the backside of the substrate to the conductor plane at the topside, vias or viaholes are used. The via is used in this project to shunt the metallic waveguide with the ground plane and also to connect the strips in the CPW line of the antenna demonstrator. Also, many vias are used for the RF MEMS switch. The via design has to put the skin effect and the inductance into consideration. As seen in Figure 3.9, a via is represented in distributed elements as serial and shunt inductances [94]. At high frequency, this reactance is large that it has to be solved by creating a via with a smaller dimension. Moreover, the stub section is usually introduced in the strip extension to further match this via.

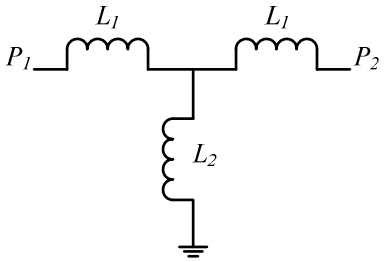

Figure 3.9. Two-port equivalent circuit of the via. P_1 and P_2 are input and output ports, respectively.

The tapering (or step discontinuity) in a CPW line is used for adapting the cross-sectional dimension of a CPW line while it still maintains the characteristic impedance of the line. In addition, the purpose of this taper section is to minimize the discontinuity during the size transition. The angle of this size transition should be optimal enough not to introduce a significant reflection [66]. The angle range from 45° to 60° is considered to be acceptable [95].

For the antenna demonstrator, the SMA connector is used to connect the CPW line with a coaxial cable or measurement equipment. A parallel path of the ground and signal strips has to be maintained; this includes the distance and the width between strips. This is to improve the matching condition and insertion loss for the transition from a cladding substrate (coaxial probe) to a substrate-air (CPW line) type of dielectrics [9]. Figure 8.3 in the Appendices shows how the surface current in a transition applies. It can be observed that the outer and lossy conductor acting as the ground of the connector may not perfectly be parallel to the signal conductor at the center of the conductor. Each finite section in a transition may have slightly disturbed characteristic impedance where the reflection may occur. An optimized connector can be found in literature [8], though it is difficult to find this product in the market. A symmetrical positioning of the SMA connector using soldering material may suffice to maintain parallel paths.

3.3.3 λ/4 transmission line

In the design of the SP3T switch, three λ/4- or quarter-wavelength transmission lines are required. Each quarter-wavelength line will invert the load impedance. The well-known formula for the input impedance at certain length (l) is given by [99]:

$$Z_i = Z_o \frac{Z_L + jZ_o \tan(k_p l)}{Z_o + jZ_L \tan(k_p l)}, \tag{3.18}$$

where Z_L, Z_o, and Z_i are the load impedance, the line's characteristic impedance, and the input impedance, respectively. Also, k_p is the propagation constant. Suppose that the length is a quarter wavelength, $l = \lambda/4$. Consequently, $k_p l = \pi/2$ and equation (3.18) becomes:

$$Z_i = Z_o^2 / Z_L. \tag{3.19}$$

Because the impedance is normalized to Z_o, then equation (3.19) shows that a quarter-wavelength transmission line inverts the load.

The application of this quarter-wavelength transmission line in the designed SP3T switch is to invert the loading of the down-state position of the beam, which is, for very low resistance, the load impedance can be approximated as a short circuit (zero-load impedance). In this way, the wave in the intersection (see Figure 3.3) sees the closed circuit (i.e. down-state beam) as an open circuit (∞-load impedance).

3.3.4 Packaging

RF MEMS components are very fragile and require packaging. There are two types of packaging, namely the wafer-level packaging and single-chip packaging. The wafer-level packaging is intended for a single MEMS switch or other simple devices such as varactor. For the SP3T MEMS switches which have three beams structure and the transmission line, a single-chip packaging is preferred. As seen in Figure 3.6, the single-chip packaging is designed which can allow hermetic cavity sealing. This cavity is to allow the movement of the beam, whereas the hermeticity is required to prevent cancellation of the spring force by water droplets and other contaminants on the beam [34]. In this design, the hermeticity is also assured by creating vias (instead of conventional transmission line) to connect the RF MEMS structure with outside world [26].

Unlike the wafer-level packaging, the single-chip packaging is implemented after wafer dicing, using pre-fabricated sapphire packages. Pre-fabricated packages require hermetic cavity sealing through clogging, shedding, and soldering of the bump as explained in Figure 3.6, and welding.

3.4 RF MEMS characterization

In this section, the characterization of the SP3T MEMS structure is reported. The RF MEMS switch, as mentioned earlier, is based on capacitive-shunt structure. In Figure 8.5 in the Appendices, the bird's-eye view of this structure is provided, to give a clear drawing of the SP3T. It is also comparable to the structure in Figure 3.3. This characterization is obtained using CST MWS^{TM}, a full-wave EM simulator.

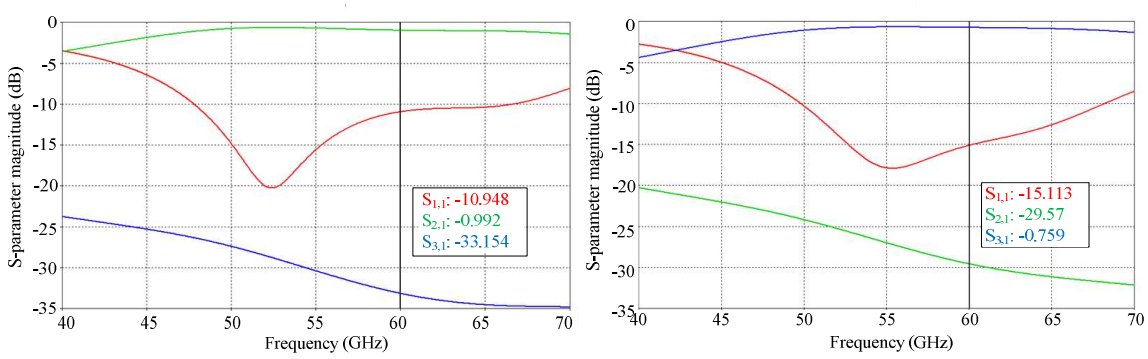

(a) (b)

Figure 3.10. S-parameter over a frequency band of the SP3T RF MEMS: (a) the right-angle arm and (b) the straight arm.

In Figure 3.10, the S-parameter in a frequency range from 40 to 70 GHz is shown for both the right-angle arm and the straight arm. The straight arm means for the signal path from facing ports. One of the ports must be the port that is connected to the RF front-end circuits. On the other hand, the right-angle arm is for the signal path from perpendicular ports. The performance of the straight arm is slightly better than the right-angle arm. The optimization has been performed by introducing a mitered section of the ground strip as shown in Figure 3.3(b) (see l_7).

Table 3.4. Comparison of RF MEMS switches: 11-GHz OTS product vs 60-GHz design.

	Insertion Loss S_{21} (dB)	**Insertion Loss S_{31} (dB)**	**Isolation S_{21} (dB)**	**Isolation S_{31} (dB)**
RMSW 220 at 11 GHz (MEMS only) [98]	-0.6	-0.6	-20	-20.5
Designed MEMS at 60 GHz (including vias and packaging interconn.) *	-0.76	-0.99	-29.5	-33.2

The -10dB bandwidth of this SP3T ranges from 50 to 67 GHz which already includes the ISM band around 60-GHz frequency. The insertion loss is -0.992 and -0.759 dB for the right-angle arm and the straight arm, respectively. Moreover, the port isolation is -33.154 and -29.57 for the right-angle arm and the straight arm, respectively. Note that these values are obtained including the impact of the transition and packaging structures. For example, the insertion loss for the 0-level structure (only MEMS structure) is -0.445 dB, which is obviously better when there is no influence from the interconnection and chip packaging. Note that the convention for the negative value of the insertion loss and isolation applies as mentioned in section 0.

These obtained S-parameters are summarized and compared with the available market product for lower-band applications, e.g. at 11 GHz. in Table 3.4. It is observed that the designed MEMS structure exhibits better performance for the isolation even at 60 GHz frequency (i.e. higher frequency), though the design already includes the interconnection and hermetic packaging. An acceptable lower performance for the insertion loss is mainly due to the interconnection, e.g. via and solder bump. As will be discussed later in Chapter 5, the isolation between switched-beam antennas using this designed MEMS is limited in the MEMS part (~ -30 dB), while in the antenna part, the isolation is about -40 dB. Therefore, pushing for a lower isolation in the antenna part is not necessary.

Simulation snapshots of the H-field (or surface current) are shown in Figure 3.11(a) and (b) for the straight arm and the right-angle arm, respectively. It can be seen that the signal can be switched to the appropriate path with less reflection.

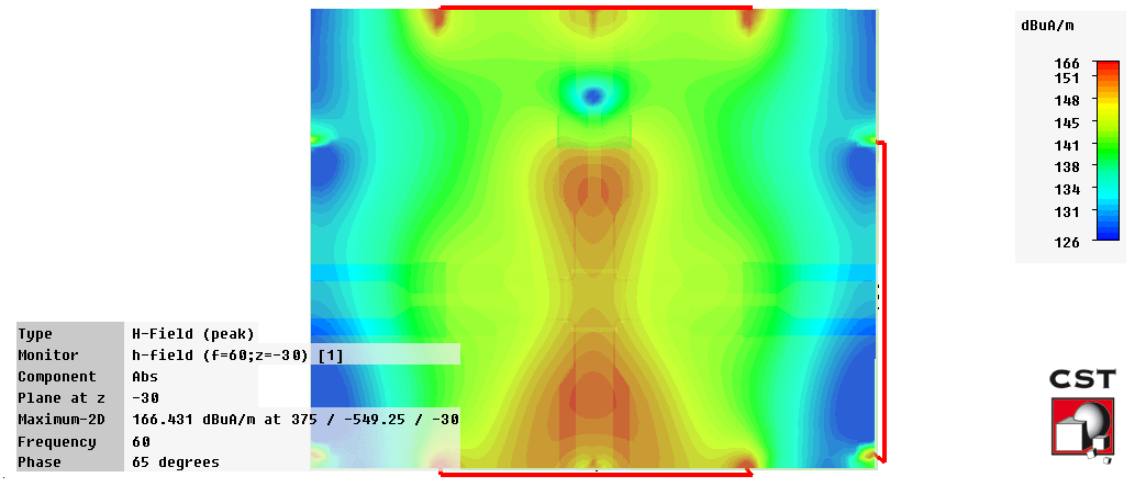

(a)

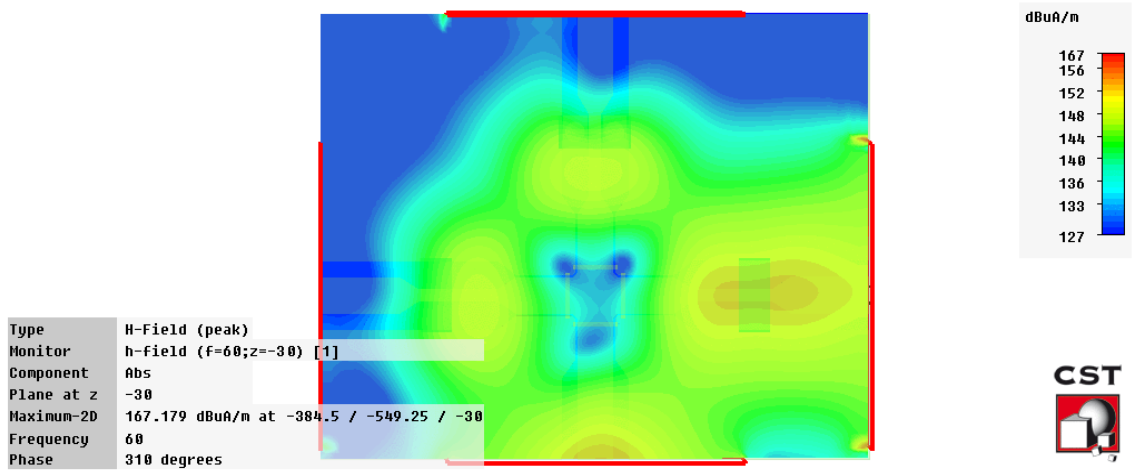

(b)

Figure 3.11. Simulation snapshots of the SP3T RF MEMS: (a) the straight arm and (b) the right-angle arm.

The capacitance and inductance of the beam in both up-state and down-state positions are extracted from the impedance matrix (Z-matrix) during the simulation. It can be observed from the curve at 60 GHz that the down-state capacitance, C_d, is 1.56 x 10^{-12} F or 1.56 pF. Also, the down-state inductance, L_d, is 4.5 pH. By means of equation (3.3), the resulting down-state resonant frequency is at 60 GHz. Moreover, this L_d is low enough to give a good port-to-port isolation for frequency larger than the resonant frequency, f_o. At the same time, the C_d is large enough to give the isolation for frequencies smaller than f_o. At f_o, the isolation is determined by the series resistance of the beam material, as explained in equation (3.2).

During the up-state position, the inductance (L_u = 147 pH) is also higher than during the down-state position. This inductance is not the inductance that is due to the metal connection but, instead, the inductance due to the CPW's structure which has large gaps and

narrow signal strip. Moreover, to have a low insertion loss a low capacitance (C_u) is necessary during the up-state position. This C_u at 60 GHz is 47.6 fF, which is sufficiently low. Consequently, the capacitance ratio (C_d/C_u) is 32.73, which is an acceptable value ($20 < C_d/C_u < 100$) for a design of the MEMS switch [26] [28] (see section 3.1.1).

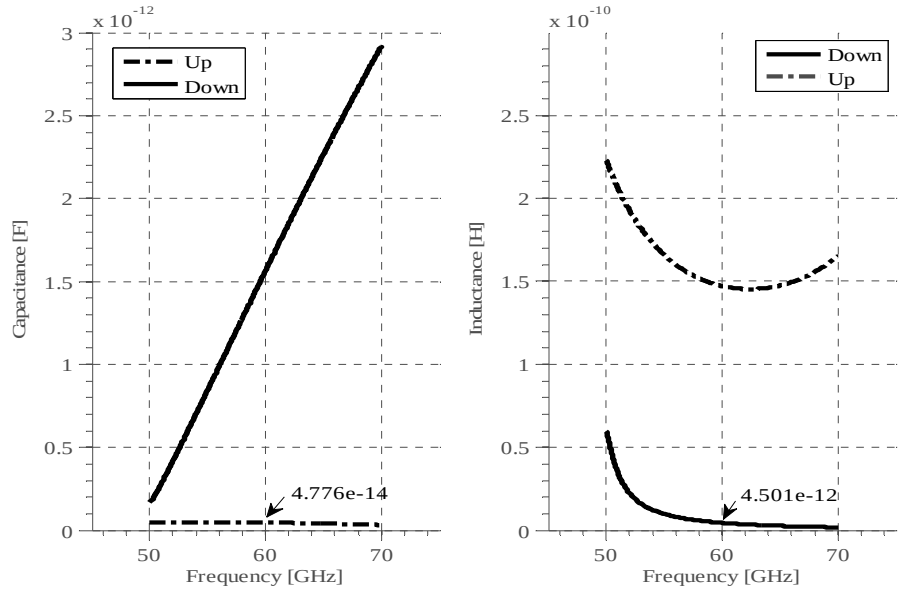

(a) (b)

Figure 3.12. (a) Capacitance and (b) inductance of the MEMS beam in up- and down-positions.

Using formulas (3.8) and (3.9), C_d and C_u are 1.077 pF and 14.4 fF, respectively. The value for C_d is slightly less than the simulated C_d. The reason is that for particularly used parameters, i.e. A (i.e. the area of the signal strip under the beam), ε_r, and t_{sn}, the down-state resonant frequency occurs at 56 GHz, as confirmed in Figure 3.10(b). At 56 GHz, C_d is around 1 pF, which is in a good agreement with the result from equation (3.8). With this optimization for the S-parameter, the isolation at 60 GHz can be down to -30 dB for both the right-angle and straight arms.

Note that this calculated example is for the straight arm and assumed to consider no dielectric's surface roughness. The optimized dimension of the SP3T here is also to give good performances for both the right-angle and straight arms. Eventually, the dimension for the $\lambda/4$ transmission line has to be considered, to give a broadband characteristic of the SP3T for both the right-angle and straight arms. $\lambda/4$ is around 400 µm, which is the chosen dimension for the arm's length in Figure 3.3(a).

In Figure 3.13(a), the true-time-delay characteristic of the MEMS is shown. For both arms, over the frequency range from 40 to 70 GHz, the transmission phase is linear. The green color is the transmission phase for the right-angle arm, where there exists a small

derailment for f > 60 GHz. In Figure 3.13(b), the group delay (in ns) is displayed for the straight arm. It can be observed that this RF MEMS switch has an almost identical group delay over the frequency band. At 60 GHz, the criterion for an identical group delay is if its variation is less than 4 ps for a bandwidth [100]. This result for the right-angle arm is also similar.

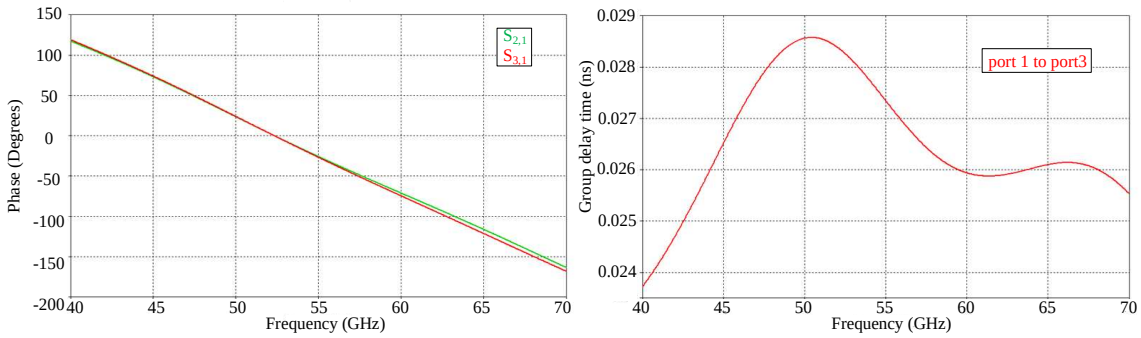

(a) (b)

Figure 3.13. (a) True-time-delay (TTD) characteristic of the RF MEMS switch; and (b) Group delay time of the RF MEMS switch.

3.5 Actuation voltage

In this section, the electrostatic and mechanic problems of this RF MEMS design are simulated using CST MPhysics Studio™. To simulate the electrostatic and mechanic problems, the material properties in Table 3.2 have to be included. This may include the electromagnetic, thermic, and mechanic properties. The DC voltage has to be defined which will actuate the aluminum beam through actuation pads right under that beam. For example, a source with 90 V_{dc} is used to feed two parallel pads in Figure 3.14. The potential distribution on the substrate's surface can be seen.

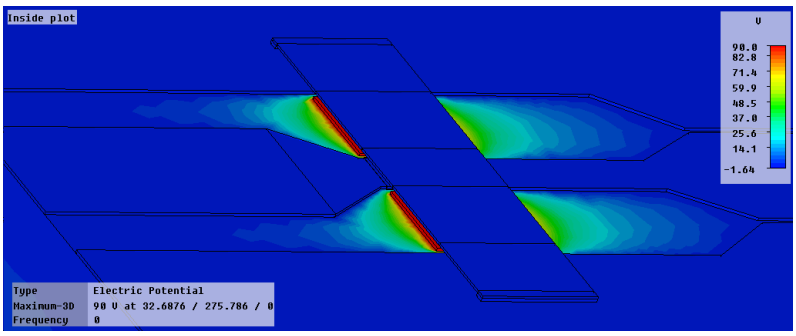

Figure 3.14. Actuation DC voltage to produce electrostatic force between actuation pads and aluminum beam.

From the simulation, this actuation voltage (90 V_{dc}) will produce a static capacitance of 133 fF under the bridge that causes electrostatic force. This electrostatic force is calculated over the pad's area that is under the beam only. Different electrostatic forces for different V_{dc}'s are summarized in Figure 3.15(a). The electrostatic force in the amount of 74 µN is observed (for 90 V_{dc}).

Using equation (3.20), the traction can be found. For corresponding V_{dc}, the traction is also shown in Figure 3.15(a).

$$\text{Traction} = \text{Electrostatic Force} / \text{Area}. \tag{3.20}$$

To simulate this mechanic problem, the displacement boundary and the traction boundary have to be predefined. For example, displacement boundaries are defined as the area where there are fixed supports or zero displacement areas of the beam. Beam holders at each side of the beam are fixed supports in this fixed-fixed MEMS design. Furthermore, the traction boundary is the area in the beam that is influenced by the actuation voltage.

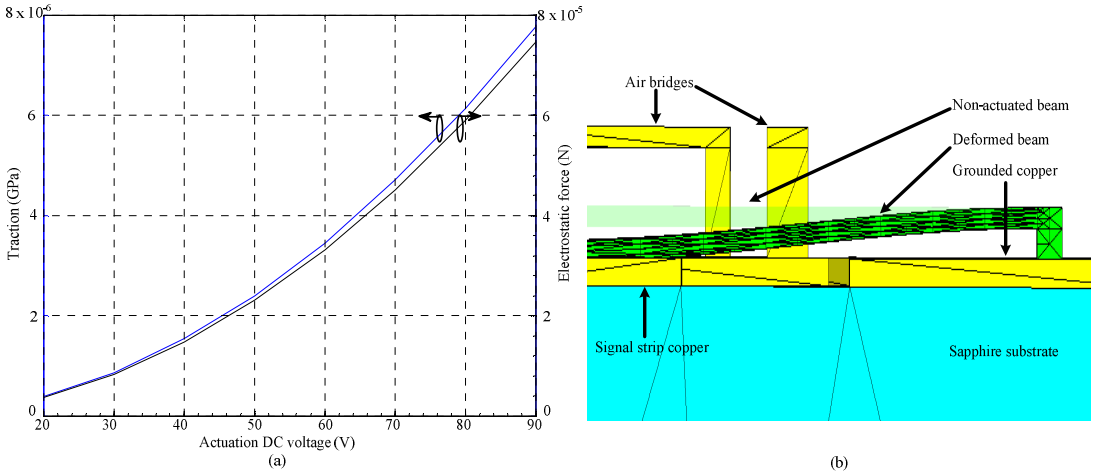

Figure 3.15. Results of mechanic and electrostatic simulations: (a) the electrostatic force and its corresponding traction by applying the actuation DC voltage, (b) a deformed aluminum beam touching the signal conductor by, e.g., applying 90 V_{dc} in actuation pads (see Figure 3.14)

It is assumed in this simulation that only the area, which is exactly above the actuation pad, is defined as the traction boundary. In Figure 3.15(b), the deformed beam is achieved after applying 90 V_{dc} in the simulation. The figure only shows half structure of the beam for the sake of conciseness. Essentially, it can be seen that the beam touches the signal strip on the CPW transmission line. This definitely shows a down-state position of the switch's beam. The zero displacement area is the area nearby the beam holder where no beam's deformation exists.

Last but not least, the switching time needs also to be calculated here to see the switching speed of this MEMS structure. Using equation (3.10), (3.11) and (3.16), the switching time, t_s, can be obtained for the aluminum beam. Most of material parameters have

been summarized in Table 3.2. The residual stress, σ, is approximated as zero when the aluminum beam is etched on the ground substrate [101]. This zero approximation is possible since the beam structure always returns to the initial position (when it is not actuated) owing to the fixed position of the etched beam holder. The resulting switching time, t_s, is then 5.4 μs for 90 V of both V_p and V_s. This switching time is an acceptable value for a MEMS switch. Also, in [26], it is stated that the practical limit of switching time will be around 1 μs for high-reliability operation.

CHAPTER 4

4 Prototype of the switched-beam antenna array

In Chapter 2, the dielectric-rod antenna array has been designed and optimized through the simulation. Its structure is made conformal that it can provide a broad scan range. In Chapter 3, an SP3T has also been designed. Its switch type is the capacitive-shunt RF MEMS. Both the antenna structure and the switch structure are designed for millimeter-wave applications, particularly at 60 GHz. In this chapter, the prototype of the switched-beam antenna array will be realized. It is basically a combination between the designed antenna and switch structures. To give an idea about the 60-GHz system and where the antenna and switch are found, Figure 8.8 in the Appendices is provided. Eventually, the sensitivity of the antenna structure to manufacturing tolerances is discussed as supplementary to the discussion in Chapter 2.

4.1 Integration of the antenna and RF MEMS

The RF MEMS switch has to be placed as close as possible to the antenna. This is to limit the loss that is created by the transmission-line part. The source of this loss can be from the conductor, the dielectric, or even the radiation. Figure 4.1 is again provided to give an overview of the integrated antenna and switch structures. The blue-colored box is the SP3T chip. The yellow lines are structures that are made from metallic conductors, e.g.

transmission line, waveguide. The red-colored cylinder is the base of the rod structure, while the LCP substrate is colored in light green.

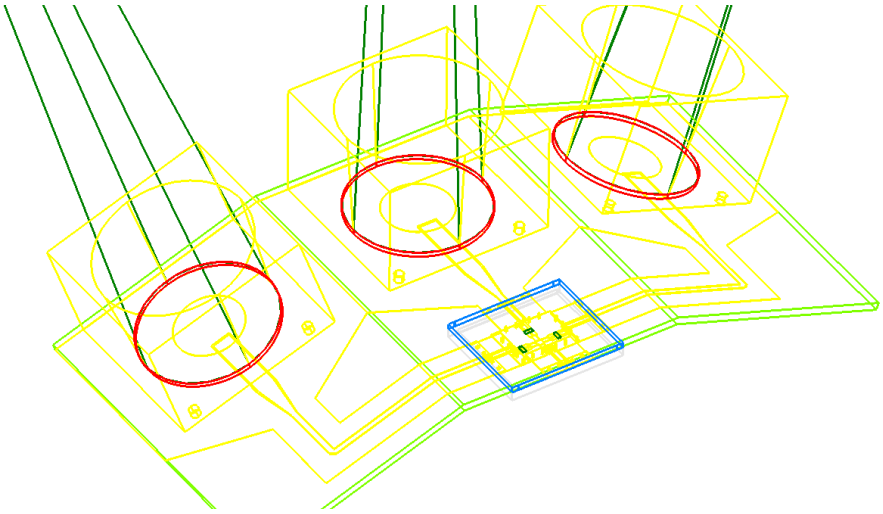

Figure 4.1. Structure of the integrated antenna and SP3T.

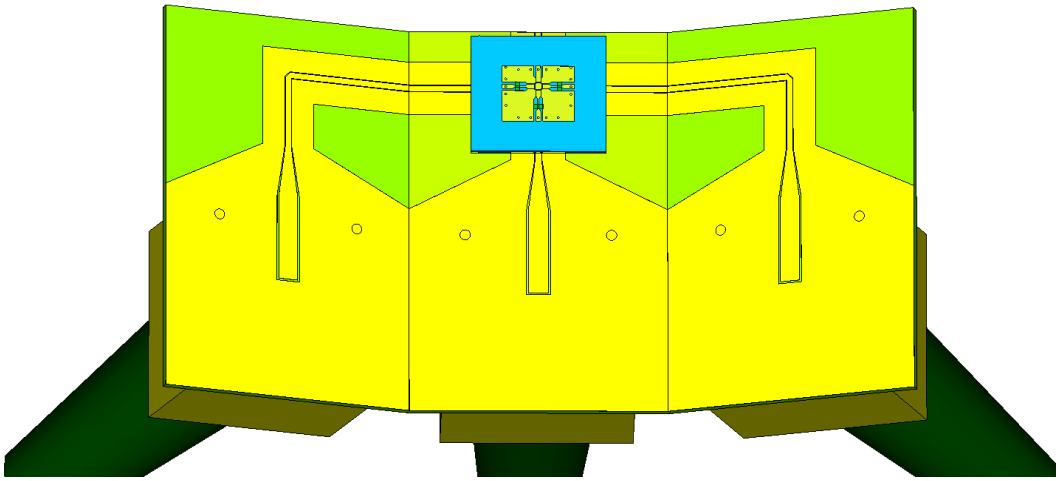

Figure 4.2. Bottom view of the integrated antenna and SP3T.

Figure 4.2 is also provided as the bottom-view of this integrated antenna and switch. It can be seen that the short arm on the switch goes to a port (obviously, it is first connected through via and solder bump). Likewise, the right-angle arms are connected to the 20°-tilted rod antennas, whereas the straight arm is connected to the upright rod antenna. It can also be seen a transition of the transmission line is used to adapt the narrow strip from the switch structure to the broad strip for the patch excitation.

The challenge to realize combined structures is how to have low reflection during the transition from one structure to another. To optimize the combined structure, the simulation is highly important and necessary here. Also, how to simulate a relative large structure mainly made from dielectric material and a very small, full of metallic structure, and having high ε_r substrate is very challenging. The reason is that the earlier one can be effiently solved by

transient (time) domain solver, whereas the latter one is efficiently solved only by the frequency domain solver of CST MWS^{TM}. The combined simulation then needs advantageous properties from both solvers. If this combined structure is solved by the frequency domain solver, a large number of tetrahedrons will be required which may exhaust the memory resource. It is also experienced that to finish the simulation with certain convergence criteria took very long duration of the simulation. On the other hand, if this combined structure is solved by the time domain solver, the simulation's accuracy may be degraded or the stability criterion is violated because the mesh (hexahedron) size is, e.g., too large. A localized meshing technique can be used to solve this issue, by individually assigning the number of mesh for each feature in the simulated structure. How dense the mesh is definitely dependent on how much concentrated fields there are at that particular region.

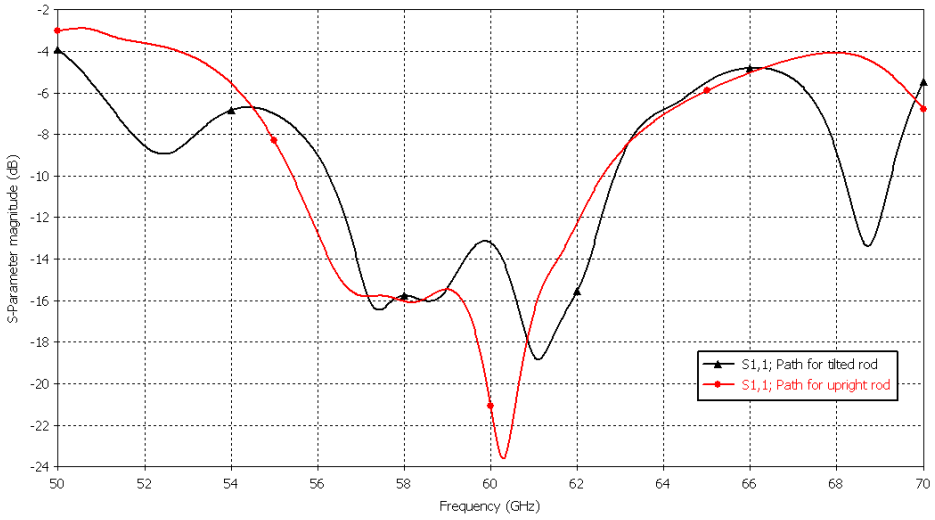

Figure 4.3. S-parameter over the frequency band of the integrated antenna and SP3T. The black-colored line is for the case when the MEMS path for the tilted rod is on (while other paths are off), whereas the red-colored line is for the case when the MEMS path for the upright rod is on.

For this combined structure, the antenna performance is limited by discontinuities found in the transition and the bending section (for both the transmission line and the LCP susbtrate). For each antenna and switch structure, the performance of the return loss is already reported in Figure 2.23 and Figure 3.10, respectively. In Figure 4.3, the return loss for the combined structure is depicted. Low return loss (S_{11} < -10 dB) is observed around 60 GHz. Few dips are found at 52 and 69 GHz; these are influenced by the corresponding switch's return loss performance and the taper discontinuity of the transmission. The difference between the curves for the tilted and upright case around 60 GHz is due to bends from both

the transmission line and the conformal structure. It is also illustrated there that the tilted rod antenna has slightly larger return loss around 60 GHz than the straight rod.

Most importantly to compare the performance between the tilted and upright rod, the gain and radiation performance are presented (see Figure 4.4). As can be expected, the tilted rod antenna has lower realized gain (16.645 dB) than the upright one (18.039 dB). A difference of about 1.4 dB is observed which is due to the longer transmission line (i.e. larger insertion loss) to reach the respective antenna's feed point. Therefore, for creating such a conformal structure for more elements (e.g. > 3), a uniform length of the transmission line is preferable. The reason is that to take into account the EIRP restriction. For instance, if one antenna is superior to the other antennas in a switched-beam array, the EIRP restriction will be applied based on the largest gain that the antenna can achieve.

Additionally, the sidelobes of the upright rod antenna are slightly larger than the sidelobes of the tilted one. This is because of the coupling of radiated fields to neighboring rods (see Figure 2.26 (b) and (c)). These fields then re-radiate. Nevertheless, these sidelobes are still -13.7 dB from the peak magnitude of the main lobe. Besides, the HPBW is around 21.7°.

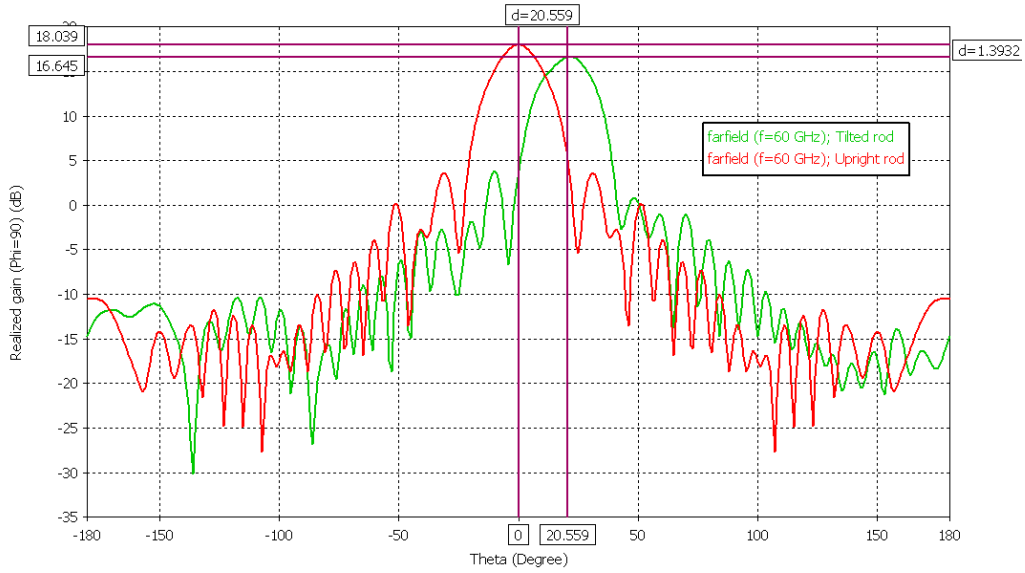

Figure 4.4. Radiation pattern of the rod antenna array with SP3T at 60 GHz.

To see the radiation pattern for different frequencies in the bandwidth of interest, Figure 4.5 is provided. The case for the upright rod antenna is used here. The pattern and realized gain for several frequencies are found to be almost equal (i.e. only maximum 0.5dB difference exists). In the black-colored curve, the pattern for $\varphi = 0^{\circ}$ is also illustrated, which clearly shows the impact of the CPW's discontinuity on the pattern at $-70 < \theta < -180$. The antenna efficiency is 88% (for the upright rod). In Figure 4.6, the broadband realized gain and HPBW are summarized. Interestingly, there is a discrepancy as large as 3.5° between the HPBW for the tilted and upright rod antenna. This is because of the antenna's position giving

different presence of neighboring rods. As mentioned earlier, some fields may be coupled to other rods resulting in larger sidelobes but narrower beam and vice versa. From the figure, it can be concluded that for the given bandwidth, the performance is nearly uniform. Eventually, it can be expected for a small frequency range other than given in that figure, the performances remain similar.

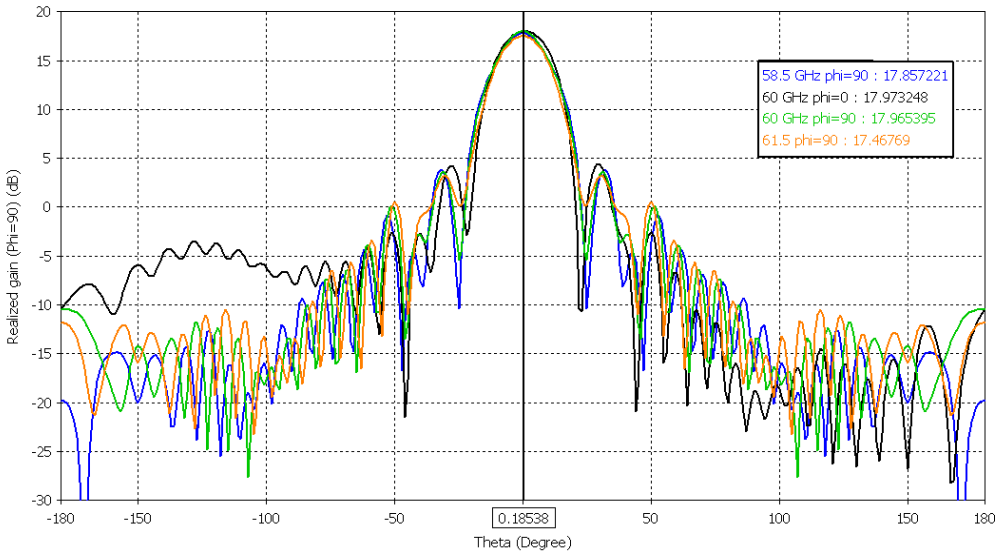

Figure 4.5. Radiation pattern of the integrated antenna and SP3T in a frequency range from 58.5 to 61.5 GHz.

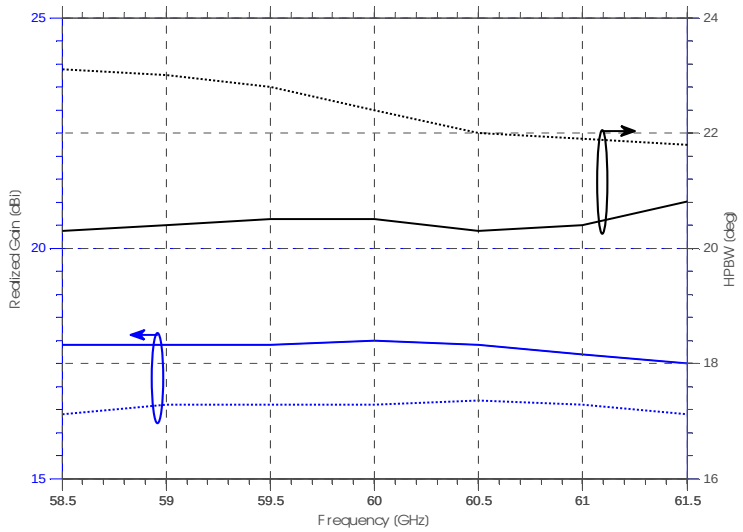

Figure 4.6. Realized gain and HPBW of the integrated antenna and SP3T in a frequency range from 58.5 to 61.5 GHz.

__ : Upright rod; …. : Tilted rod

4.2 Sensitivity of the structure

Some considerations about the sensitivity of the structure are given in this section. The simulation is used to investigate the impact of manufacturing tolerances on antenna performances. Two examples of the most sensitive part in the antenna structure are the patch dimension and the feed position. A sensitivity discussion may also arise from the substrate's ε_r variation. It has been reported in [59] that a permittivity variation ± 0.035 occurs for the LCP material, with its nominal value of 3.093. This is of course slightly different than the nominal value that is used here, i.e. 3.1, but either this permittivity discrepancy or permittivity variation does not significantly influence the resonant frequency. Also, in [59], the LCP panel homogeneity is within 1 % which results in permittivity uncertainty. Nonetheless, this uncertainty is still within the same order as the permittivity variation.

On the contrary, the sensitivity is prone to manufacturing tolerances. Examples are the dimension of the radiator and the position of the feed line, which are often the subject to manufacturing tolerance. Especially, since the structure also uses a standard, low-cost, planar manufacturing technology in which tolerances can be relatively large [50]. In addition to that, the structure also contains three-dimensional structures, namely the rod and the launcher. These structures have to be machined and moulded into a particular shape. A different material for building those structures may be more susceptible to tolerances than if it is built from another material. For example, Teflon material is more susceptible to tolerances than PS material is, while Kapton material is superior to both mentioned materials. PS material is chosen in this design because of its good dielectric properties and less prone to tolerance. Figure 2.11 can also be used to illustrate the influence of the manufacturing tolerance to the antenna performance.

The tolerance that is coming from planar parts is pictured in Figure 4.7 and Figure 4.8. The earlier figure shows the influence of the manufacturing accuracy for the patch dimension on its resonant frequency. For the reason that the rod section is excited by a circular patch, the tolerance in that patch dimension may shift the whole antenna's resonant performance. For example in the figure, a radius of 0.777 mm results in a shifted resonant frequency to 58.8 GHz instead of 60 GHz for a radius of 0.762 mm. Additionally, for a radius of 0.747 mm, not only is the resonant frequency shifted, the return loss performance also slightly degrades. A perturbation of ±15 µm is used here as the worst case in the manufacturing process [50]. In the latter figure, the tolerance from the feed position is depicted. It can be clearly seen that the variation of ±15 µm does not necessarily shift the resonant frequency. Only, the return loss is varied within an acceptable range. This means that the antenna impedance is not sensitive to the variation of the feed position. For additional information, the variance of the feed position can be often found if multilayered structure is being used. This is mainly due to the misalignment in positioning layers resulting in a perturbed feed position. However, in this design, only one layer substrate is used to avoid this issue.

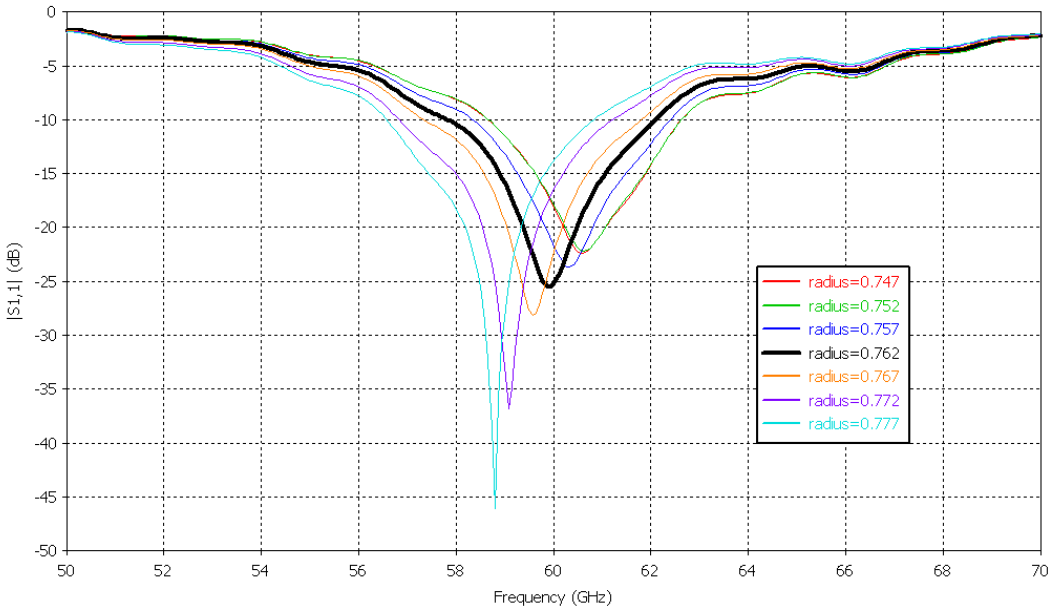

Figure 4.7. Tolerance analysis of the reflection coefficient. The patch radius ($Ø_{cp}/2$) is perturbed with δ_{max} = ±15 µm. The black-colored line is the nominal design.

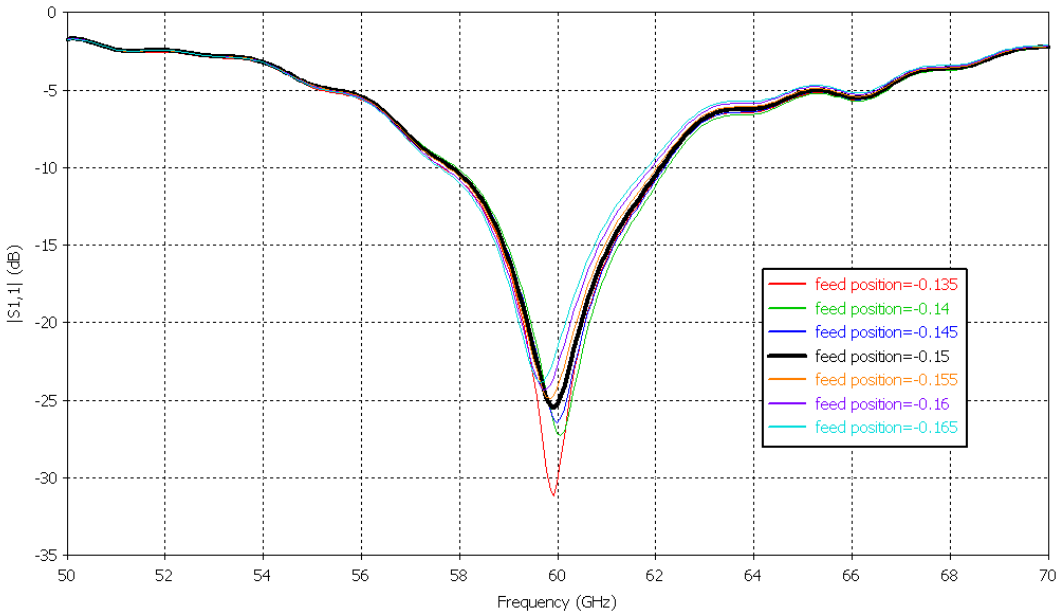

Figure 4.8. Tolerance analysis of the reflection coefficient. The nominal feed position is perturbed with δ_{max} = ±15 µm, and the black-colored line is the nominal design. This feed position is relative to the center of the patch (see Figure 2.13).

CHAPTER 5

5 Fabrication and measurement

An antenna demonstrator is used as a proof-of-concept design. It is a realization of the switched-beam rod antenna to demonstrate its feasibility. The resonant frequency of this antenna demonstrator is 11 GHz. For the antenna structure, its dimensions are inversely proportional to its operation frequency. Hence, for a higher operation frequency (i.e. 60 GHz), the antenna dimension is proportionally smaller; assuming that the material properties (ε_r and δ) are frequency independent. The detailed structure and dimensions of the manufactured antenna are shown in Figure 8.2 in the Appendices. The manufactured structure is shown in Figure 5.1. Its inter-element angle, θ_{el}, is $\sim 30^{\circ}$. The measurement results shown in this chapter are obtained from measurement equipments in the Electromagnetics laboratory of TU/e.

5.1 Consideration for manufacturing the antenna structure

The dielectric material for the planar structure is chosen to be Nelco NX 9294 instead of LCP. The reason is that to build the 11-GHz antenna demonstrator, the substrate is required to be thick to have a sufficient bandwidth (or a proportional bandwidth with the 60 GHz design). However, the available thickness of the LCP panel in the manufacturer (QPI) is very thin (i.e. approximately 100 µm) that to have around 600 µm requires several stacked panels. This will enlarge the probability that blistering will occur. The blistering is several

hollow sections filled with air between stacked LCP panels [68] [69]. The antenna performance will be degraded due to this problem. Therefore, a single panel NX 9294 which has ε_r = 2.94 ± 0.04 or almost equal to the LCP's relative permittivity is used here. Its δ is 0.0022 at 10 GHz which is also quite low. Because of the advantage of the CPW line, it is very convenient to adapt to its dimensions with the new material. This adaptation is to maintain 50-Ω characteristic impedance of the line. The antenna dimensions adapted to the new material with slightly different ε_r will definitely make manufactured dimensions slightly less proportional to the 60-GHz antenna dimensions.

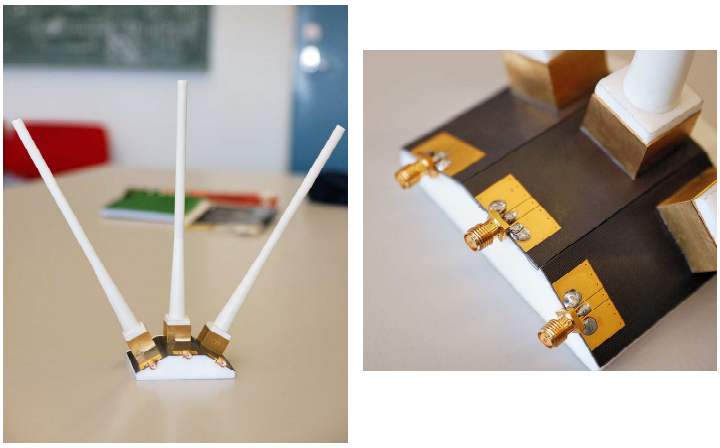

(a) (b)

Figure 5.1. The manufactured dielectric-rod antenna array: (a) 3 rod elements made from Polystyrene and (b) the SMA connector connected to the FGCPW.

The foam material is used in the structure as a holder for the PS rod and as a foundation material for a support stand (see Figure 8.2 in the Appendices). The type of the foam is Rohacell® RC 31 HF from Evonik Röhm GmbH. Its ε_r is 1.046, and its δ is 0.0017 at 10 GHz. The adsorption of up to 25% water vapour leaves the dielectric properties of this material unchanged [102]. This makes this material suitable as radome material to give a strong protection to the structure of the rod antenna. For the demonstration, the radome is not manufactured. It is because the available thickness of the owned foam material is much less than what is required to build the radome for the respective antenna. Also, this allows to see the physical construction of the design. However, since its very low, i.e. near-to-vacuum, permittivity material and its low loss, its implementation will not significantly influence the performance of the antenna. In section 5.2, this foam material is characterized to verify its performance at 11 GHz.

A matched transmission line throughout the coaxial line, SMA connector, and CPW line deserves great attention. The careful design of, especially, the matched connector is to suppress significant field discontinuity in the transition interface. A smooth transition is necessary to bridge between the evenly distributed electromagnetic fields at the coaxial end and the highly concentrated fields of even mode in the CPW. As a result, the transition interface exhibits less frequency dependency, i.e. the soldering/transition is not the limiting factor of the overall system performance. Some design considerations related to the SMA

connector may refer to the work in [8] and [9]. In [8], the 50 ohms line impedance is maintained by proper variation of the inner conductor diameter and its offset at the cross section.

For the convenience of the measurement, the transition of the CPW from the one side of the substrate to the other side is necessary. This becomes more important if the antenna is going to be measured using GSG probe which can only have a probing access from the upper side of the substrate. The transition from the lower side to the upper side of the substrate uses several vias with a diameter of 0.25 mm. These vias are separated one to another by a distance of 3 mm (see Figure 5.1(b)).

5.2 Characterization of the foam material

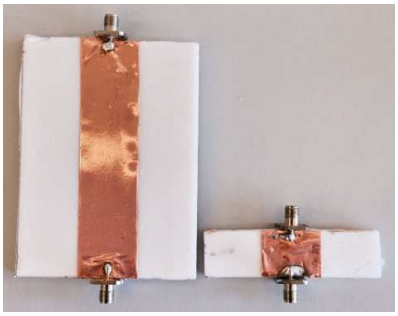

Figure 5.2. Two microstrip lines (10.06 and 1.94 cm) for characterizing the foam.

The foam material RC 31 HF will be characterized by means of the two-microstrip-line method [63]. The purpose of this characterization is to obtain the material's ε_r at 11 GHz. This measurement is also to give a feedback to Evonik about their foam product. From the name of the method, two microstip lines are used here whereby a difference in physical lengths Δl_p is applied (see Figure 5.2). The difference in electrical lengths, Δl_e, or, equivalently, the transfer phase difference, $\Delta\phi$, is given by:

$$\Delta l_e = \sqrt{\varepsilon_{eff}}\Delta l_p \quad \text{or} \quad \Delta\phi = \frac{2\pi f(\Delta l_p)}{c}, \tag{5.1}$$

where ε_{eff} is the effective permittivity, f the frequency, and c the speed of light. The advantage of this method is its capability to cancel out the corrupting effect of connectors because all four corresponding transitions and any associated reactances are identical.

The sources of error can be from the network analyzer and the physical measurement of the two lines. Since the network analyzer is calibrated and has error-correcting techniques, this leaves the error due to the physical measurement. The percentage error or normalized error in determining ε_r is given in [63]:

$$\frac{\delta\varepsilon_r}{\varepsilon_r} \approx \frac{\delta\varepsilon_{eff}}{\varepsilon_{eff}} = 2\left(\frac{\delta\Delta l_e}{\Delta l_e} + \frac{\delta\Delta l_p}{\Delta l_p}\right). \tag{5.2}$$

It can be noted that the normalized error in ε_{eff} is approximately equal to the normalized error in ε_r. Most importantly, the error in measurement of ε_r is proportional to the percentage error in the measurement of Δl_p. Thereby, it can be improved by using a large value of Δl_p.

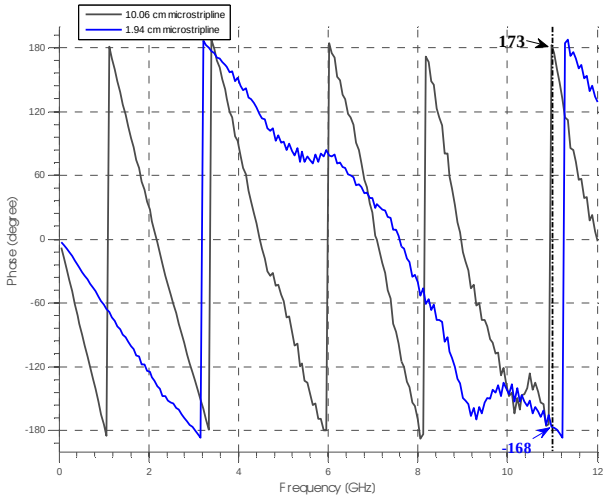

Figure 5.3. Measured phases over a frequency range in the two-microstrip-line method.

Figure 5.3 illustrates the measurement result using the aforementioned microstrip lines. The phase difference can be calculated directly from phase values at 11 GHz. Using equation (5.1), ε_{eff} is then equal to 1.0126. It can be seen that a sufficiently large difference between two transmission lines is utilized here.

The relative permittivity (ε_r) can be obtained from the effective permittivity (ε_{eff}) of a microstrip line by means of the following equation [87]:

$$\varepsilon_{eff} = \frac{\varepsilon_r+1}{2} + \frac{\varepsilon_r-1}{2}\left(1 + 12\left(\frac{H}{W}\right)\right)^{-\frac{1}{2}}, \quad \text{when } \left(\frac{W}{H}\right) \geq 1. \tag{5.3}$$

W (= 2.46 cm) is the width of the microstrip line, and H(= 0.5 cm) is the thickness of the substrate-under-test (SUT). In that equation, the influence of the strip conductor's thickness is not included. Because a thin conductor is used here, that equation is still accurate. Note that this equation is only applicable if $\left(\frac{W}{H}\right) \geq 1$. Eventually, ε_r is equal to 1.015 at 11 GHz, which is nearly the same as the provided data from Evonik for the foam material at10 GHz.

5.3 Characterization of the RMSW 220HP evaluation board

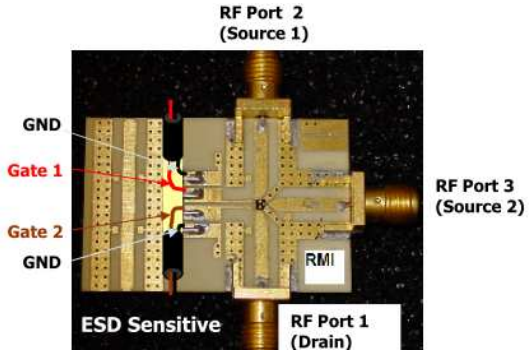

Figure 5.4. RMSW 220HP evaluation board.

In the demonstration of the switched-beam rod antenna array, a switch is required. In the design, a 60-GHz RF MEMS SP3T has been optimized using the simulation. A 90-V_{dc} actuation voltage has been tested in the simulation to be feasible to pull down the beam. In the demonstration, an evaluation board (RMSW 220HP) for the MEMS switch that has the operation frequency from DC to 14 GHz is used. This is a product from Radant MEMS, Inc. (RMI). The structure of this evaluation board can be viewed in Figure 5.4, and its performance can be reviewed in Table 3.4. Important to note that this performance is measured for the MEMS only, without considering the presence of RF SMA connectors, soldering, bondwires, and microstrip line. The source of the actuation voltage is given by either Gate 1 or 2 for signal flow in Source 1 or 2, respectively. This MEMS is ESD sensitive because it has been fabricated without any ESD protection.

5.3.1 Return loss and insertion loss

Before this MEMS evaluation board is connected to the antenna, a characterization is performed. Some results for this measurement are shown in Figure 5.5(a) and (b) for Source 2 and 1, respectively. It can be seen that the right-angle arm (Source 2) has a better performance than the straight arm (Source 1). The return loss of Source 1 is also higher than -10 dB, and the insertion loss is around -5 dB around 11 GHz. On the other hand, Source 2 has the return loss of lower than -10 dB and the insertion loss of -3 dB (i.e. loss of 3 dB). Therefore, during the demonstration, Source 2 will be used because of its better performance. Note that the insertion loss of the sole MEMS is 0.6 dB (see Table 3.4), which is 2.4 dB better than the MEMS in this evaluation board.

Most importantly, the measurement equipment (VNA) has to be calibrated before performing the measurement. The 2-port calibration is performed for a particular frequency range.

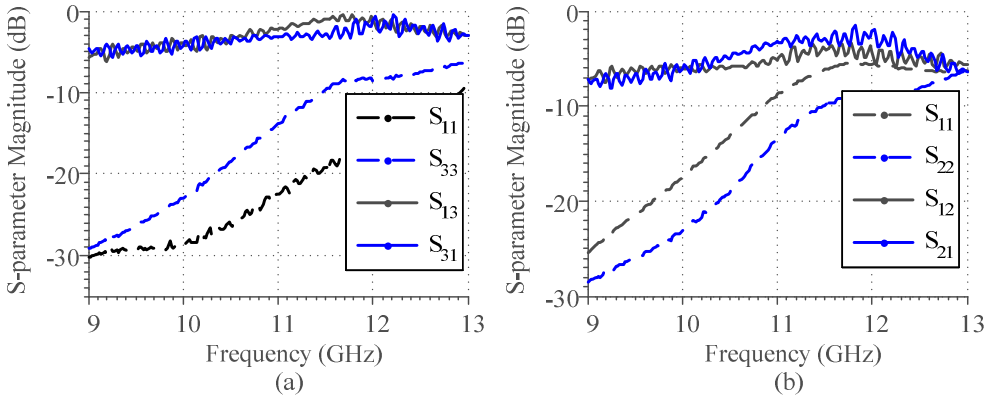

Figure 5.5. Measured return and insertion losses for both (a) the right-angle arm and (b) the straight arm. S_{11}, S_{22}, and S_{33} are return losses and S_{13}, S_{31}, S_{12}, and S_{21} are insertion losses (see Figure 5.4).

5.4 Characterization of the conformal rod antenna

In this section, the S-parameter and radiation pattern of the dielectric-rod antenna array will be characterized. The measurement results of the manufactured antenna (see Figure 5.1) will be presented and compared with the simulation result (see also simulation results in Figure 8.4 in the Appendices). The HPBW and realized gain will be discussed for that antenna.

5.4.1 S-parameter

In Figure 5.6, the S-parameter magnitude of the antenna is measured, which includes the return loss (in figure (a)) and mutual coupling (in figure (b)). The return loss for all three elements of the array shows a resonance at 11.2 GHz which is in a good agreement with the simulation result which has the resonance at 11 GHz. This frequency shift of about 1.8 % is as a result from a.o.:

- permittivity variation of the planar substrate (see section 5.1) and the rod's material;
- manufacturing accuracy (see Figure 4.7 and Figure 4.8) and surface roughness.

However, the permittivity variation usually contributes more to the caused shift because the accuracy of the manufacturer is ± 15 µm, which is relatively small for the 11-GHz frequency band.

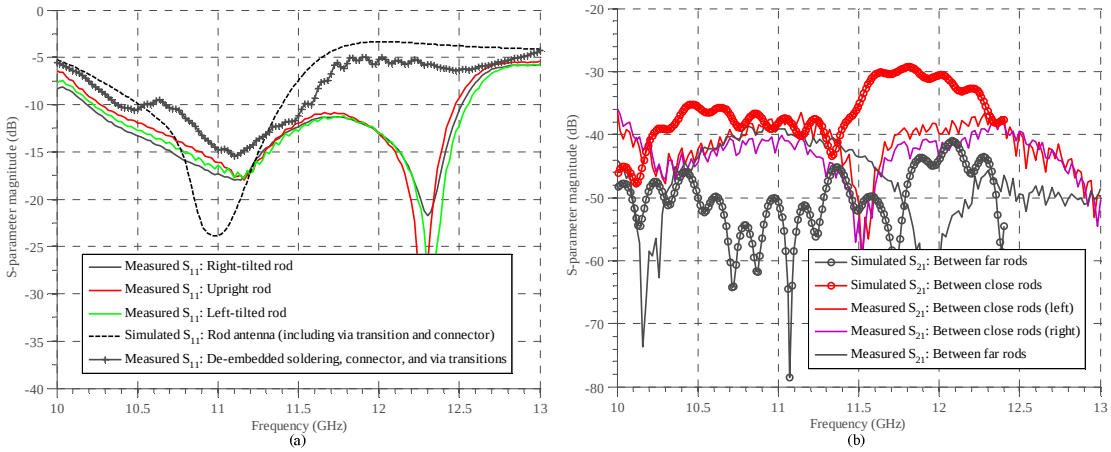

Figure 5.6. Comparison between the simulation and measurement for both (a) return loss S_{11} and (b) mutual coupling S_{21}. TRL-calibrated S_{11} is also given in figure (a).

At 12.3 GHz, there is a resonance dip which is caused by the soldering of the SMA connector. The cause of this peak can be shown by performing the TRL calibration [50][62][64]. This TRL calibration can de-embed the soldering, via transition, and SMA connector from the measured antenna system. This also means that this TRL calibration creates a new reference line in the measurement. This reference line is placed as close as possible to the characterized antenna. Thereby, after the calibration, what is measured is only the antenna. This calibration is performed using the VNA. Open, thru, and line configurations for the calibration of the transmission line are shown in Figure 5.7. Note that these configurations are unique and only for this manufactured antenna. After this calibration is performed, the dip at 12.3 GHz is removed as shown in the figure. Subsequently, the antenna bandwidth of 800 MHz is obtained. Most importantly, these TRL configurations may still introduce the uncertainty in the measurement because there is still the soldering part. However, the measured antenna can be accurately characterized using this calibration.

The mutual coupling between antenna elements is also measured, and the result is shown in Figure 5.6(b). The simulated and measured results are in a good agreement, especially between close rods (e.g. between tilted and upright rods). The mutual coupling of -40 dB at 11.2 GHz is considered sufficiently low for the switched-beam operation. This value is limited by the isolation of the RF MEMS switch which is only -20 dB. However, in Chapter 3, the 60-GHz SP3T has been designed with -30 dB isolation. Furthermore, the mutual coupling between far rods is -40 dB while the simulation result gives around -50 dB. For this weak signal, the impact of the VNA's noise floor becomes significant, yet the measurement has shown a good isolation between antenna elements.

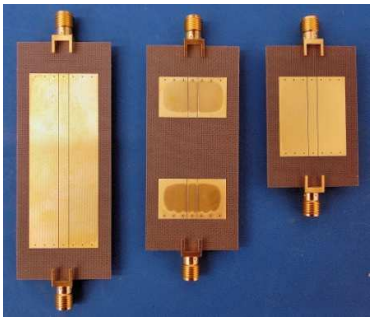

Figure 5.7. (left to right) Line, open, and thru configurations for the TRL calibration of the transitions.

5.4.2 HPBW, far-field pattern, and antenna gain

In this section, the radiation pattern of the manufactured antenna will be measured. The measurement is performed in an anechoic chamber (see Figure 5.14(b)). First, the gain of the antenna at the operation frequency (i.e. 11.2 GHz) is measured and calculated. Figure 5.8 shows the received power for different communication setups. A horn antenna with an unknown gain is used for measuring the antenna.

The loss in the cable and the gain of the horn antenna can be measured by means of Friis equation:

$$P_r = P_t + G_t + G_r + 20\log_{10}\left(\frac{\lambda}{4\pi R}\right), \tag{5.4}$$

where P_r is the received power, P_t the transmitted power, G_t the gain of the Tx antenna, G_r the gain of the Rx antenna, λ the wavelength, and R the distance between the antennas. The transmitted power is -10 dBm at 11.2 GHz. By using the information in the black-colored curve in Figure 5.8, the cable loss at 11.2 GHz is -15.06 dB. This cable loss will be included in equation (5.4) in the calculation of the antenna gain. The received power using two identic horn antennas can be observed in the blue-colored curve. By using equation (5.4), the gain of the horn antenna at 11.2 GHz is 17.53 dBi. R is 2.64 m, and the cable loss has been included in the calculation. Eventually, the gain of the rod antenna can be calculated using the same procedure. The gain for each of the antenna element can be seen in Figure 5.9. Note that this maximum gain (i.e. ~17 dB) is slightly smaller than in the 60-GHz design (i.e. 18 dB). This is due to the additional loss from the transmission line that is made large enough to give some spaces for measurement convenience and to have a stable structure.

The measured radiation pattern for each antenna element is in a good agreement with the simulation. 20°, 22°, and 22° are the measured HPBW for left, upright, and right rod, respectively. In the simulation, the HPBW is 22.8°, 22.9°, and 22.8°, respectively. The gain of the simulated and measured antenna is also almost similar. There is still a small reflection in the anechoic chamber which can be verified by the fluctuating value in Figure 5.8. This may

explain the gain discrepancy between the simulated and measured antenna. The SLL between the simulation and the measurement is also in a good agreement, which is around -17 dB.

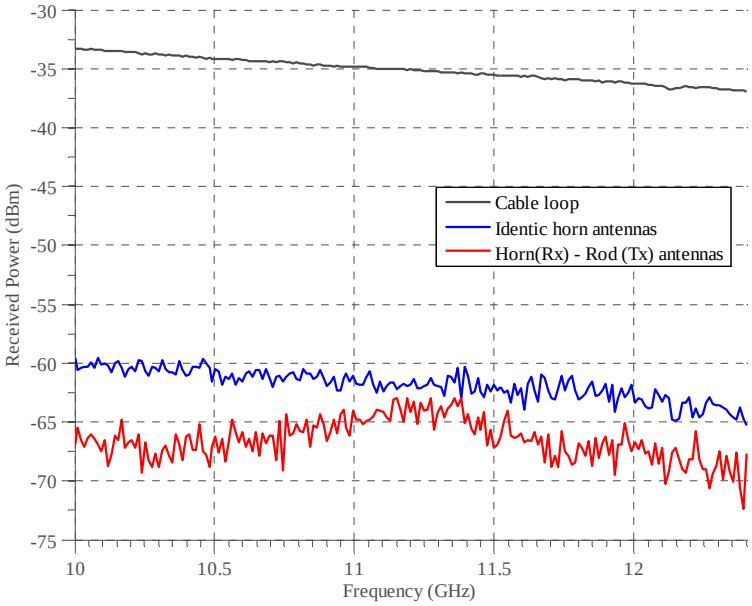

Figure 5.8. Measurement result of the received power for the gain measurement.

Moreover, the measured gain of each antenna element is also almost similar. This variation is caused by the manufacturing accuracy in creating the rod structure. It has been reported by GTD that the inaccuracy of 1 – 2 mm in the rod diameter exists. This deformation mainly occurs at the bottom of the rod. The reason is that a wide cross section of the rod may allow the air fills between PS materials during the molding process. After the temperature is decreased, a reduced diameter occurs at the rod base. This deformed material has also been simulated to verify the occurred variations.

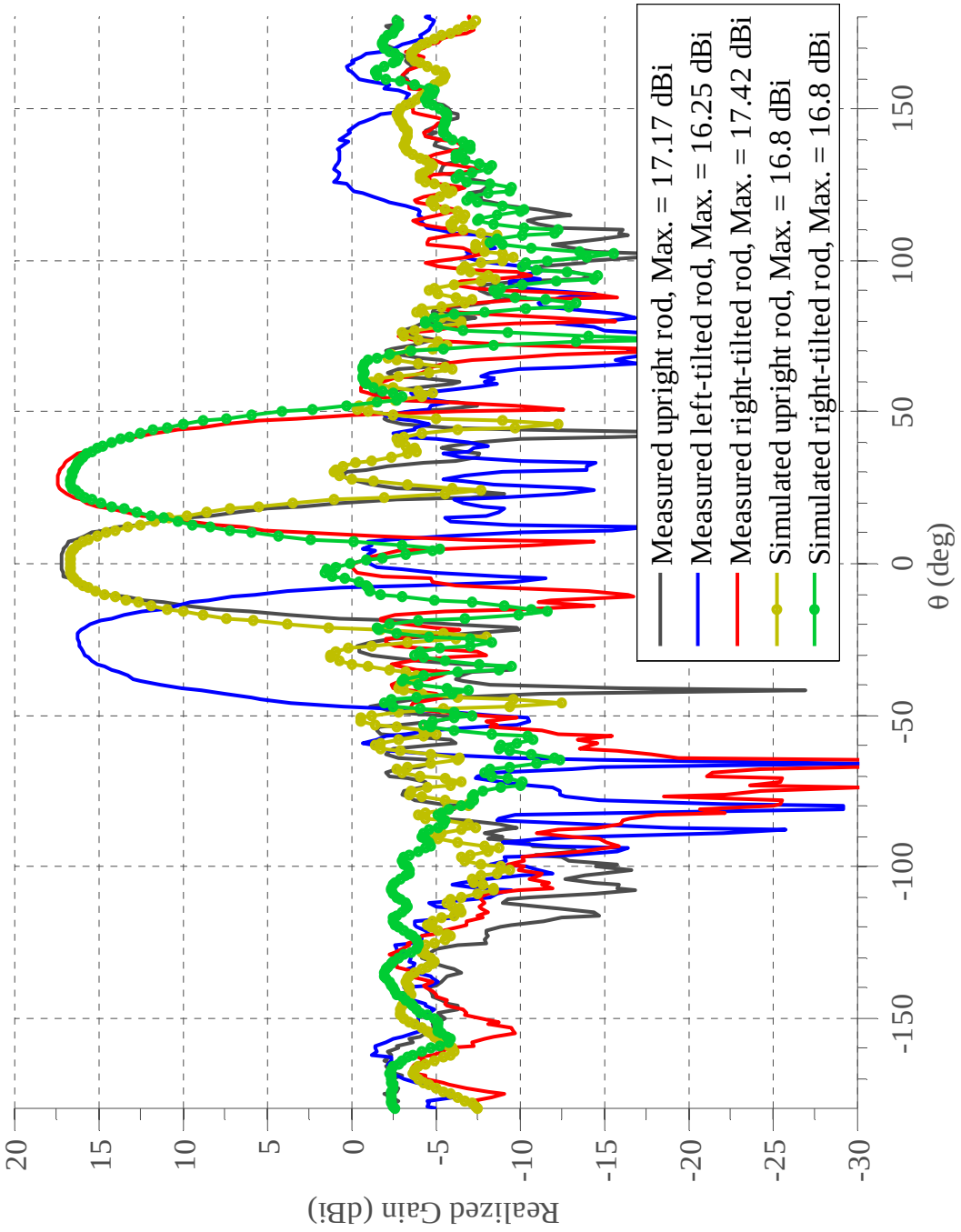

Figure 5.9. Measured radiation pattern of the conformal dielectric-rod antenna array. Simulation results are also given for the comparison.

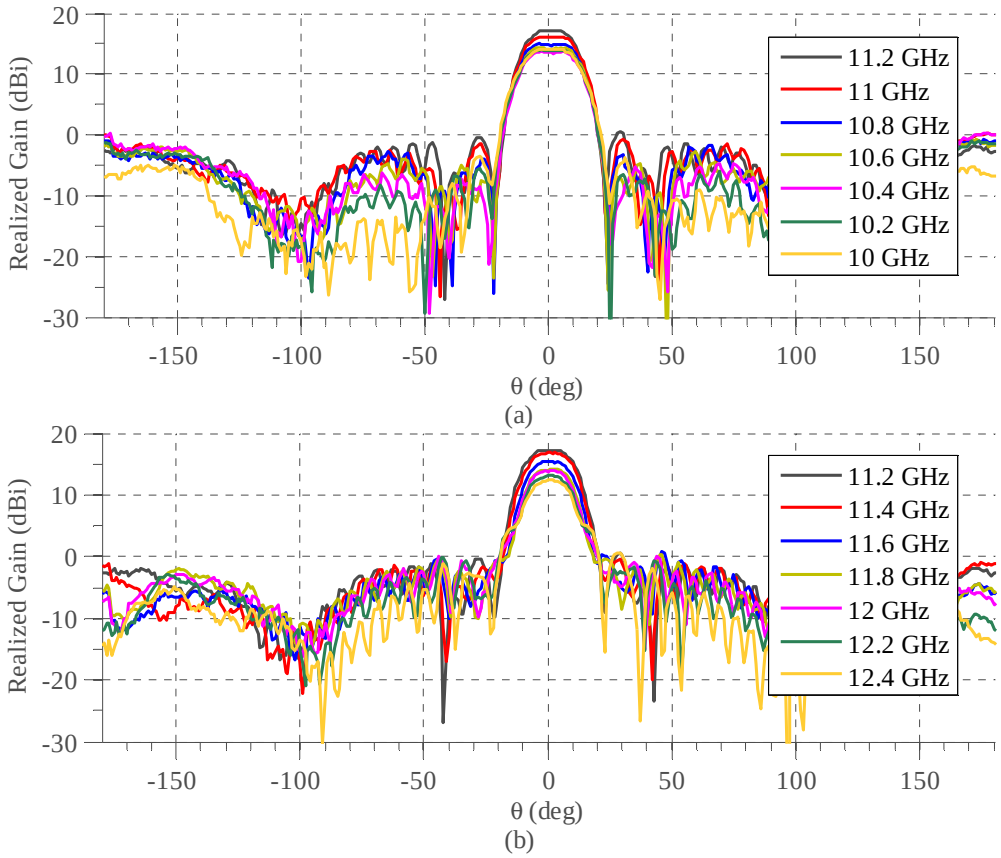

Figure 5.10. Measured radiation pattern for different frequencies (a) from 10 to 11.2 GHz and (b) from 11.2 to 12.4 GHz.

The measured radiation pattern over a frequency range is shown in Figure 5.10. At 10.6 and 11.6 GHz, the realized gain is 14.34 and 15.43 dBi, respectively. Moreover, the radiation pattern is almost uniform at the frequency band of interest (i.e. 10.7 – 11.5 GHz).

The co- and cross-polarized radiation patterns are also measured and shown in Figure 5.11(a) and (b), respectively. In figure (a), the uniformity of the measured radiation pattern for both $\varphi = 0^{\circ}$ and 90° is observed, which is also in a good agreement with the simulation. At $\theta \sim 100^{\circ}$ and -100°, the influence from the CPW line on the radiation pattern can be observed for both the simulation and measurement. In figure (b), the measured co-polarized pattern in the plane $\varphi = 90^{\circ}$ is compared with the cross-polarized patterns. A large magnitude difference between the co- and cross-polarized patterns indicates a linear-polarized radiation pattern of the antenna. In this case, it is a vertical linear polarization which has been specified in Chapter 2. The measured E-cross in the plane $\varphi = 0^{\circ}$ has a large difference with the simulation result (i.e. as large as 20 dB). This is because the received power for this cross-polarized measurement is close to the VNA's noise floor.

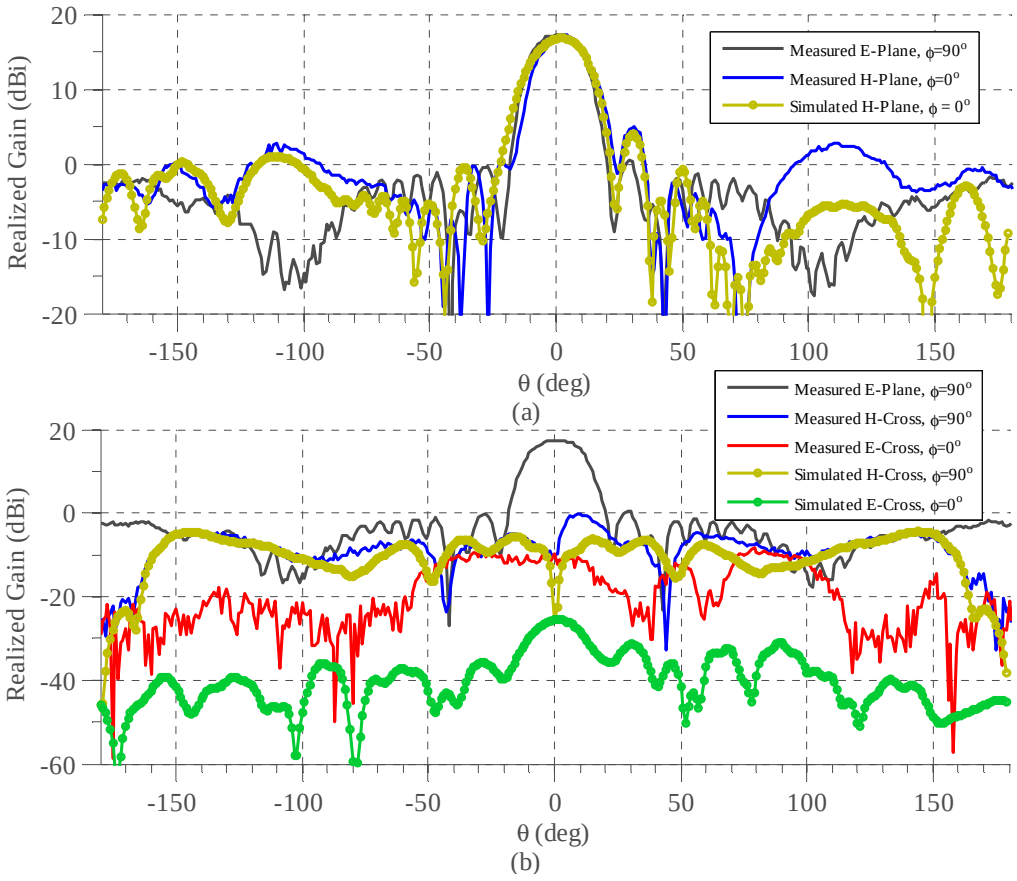

Figure 5.11. (a) Comparison of the co-polarized radiation pattern between the simulation and measurement, and (b) comparison of the cross-polarized radiation pattern between the simulation and measurement for $\varphi = 90^{\circ}$ and $\varphi = 0^{\circ}$. The measured E-plane for $\varphi = 90^{\circ}$ is also included for the comparison.

In Figure 5.12, the normalized radiation pattern for different measurement distances is depicted. The distance is increased from position 1 to 4. The position here corresponds to the position of the horn antenna. The corresponding received power is also mentioned in the figure. The ripple in sidelobes is observed to be shifted for different measurement positions. This is due to reflections from the wall in the measurement chamber. These reflections have a constructive and destructive behavior over the measurement angle, and its influence predominates in the sidelobe pattern.

Now the performance of the rod made from the PS and Teflon materials is compared. This Teflon rod has the optimal dimensions of the PS rod. The normalized radiation pattern of the PS rod is compared with the normalized radiation pattern of the Teflon rod in Figure 5.13. The rod made from the Teflon material, which has a lower relative dielectric permittivity than the PS material, produces a larger HPBW and SLL. This shows that for the same rod's dimensions, the PS rod can guide the wave better than the Teflon rod. The Teflon rod can have a similar performance as the PS rod if the dimensions are changed and optimized, e.g. the diameter is increased, as shown in equation (2.4).

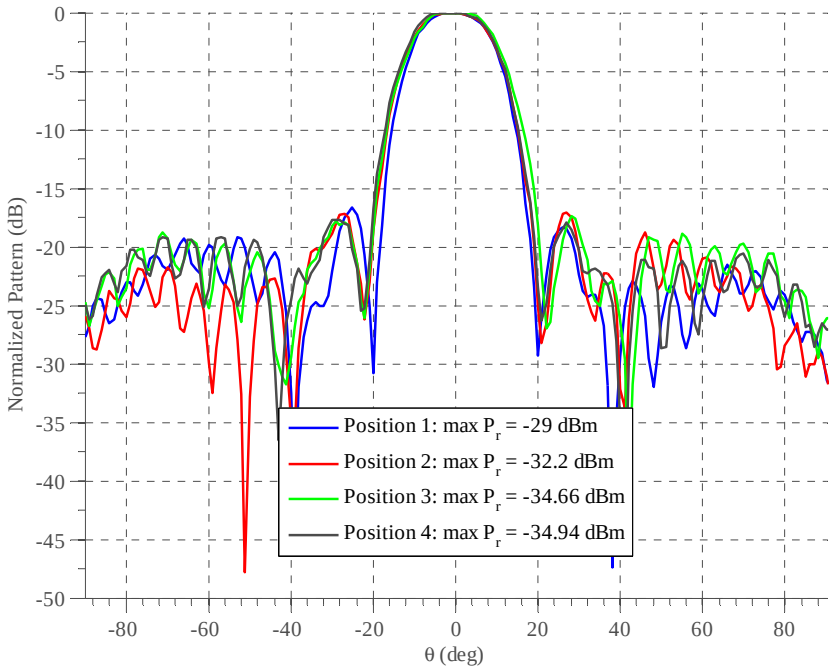

Figure 5.12. Sidelobe comparison for different measurement distances.

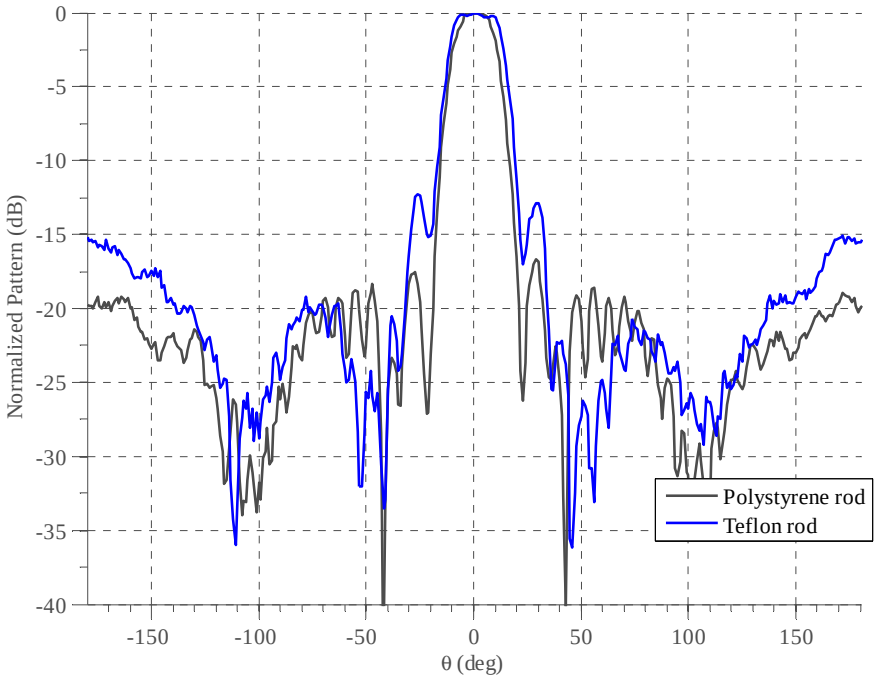

Figure 5.13. Comparison of the normalized radiation pattern for different rod materials (i.e. different ε_r).

5.5 Characterization of the antenna system

The combined antenna and RF MEMS switch will be characterized in this section. The measurement setup for this switched-beam operation is shown in Figure 5.14. A DC power supply is used to provide 5 V_{dc} to the DC-DC converter. This DC-DC converter is utilized to convert 5 to 90 V_{dc}, which is the required voltage to actuate the MEMS. The constructed DC-DC converter is shown in Figure 8.7 in the Appendices. The schematic and the list of the component for this circuit are shown in Figure 8.6(a) and (b) in the Appendices.

The radiation pattern is measured as in Figure 5.14(b). Note that all the metallic components inside the anechoic chamber have to be covered with the absorbing material for accurate measurement. These metallic components can be the DC power supply, the DC-DC converter, the MEMS, and the cabling.

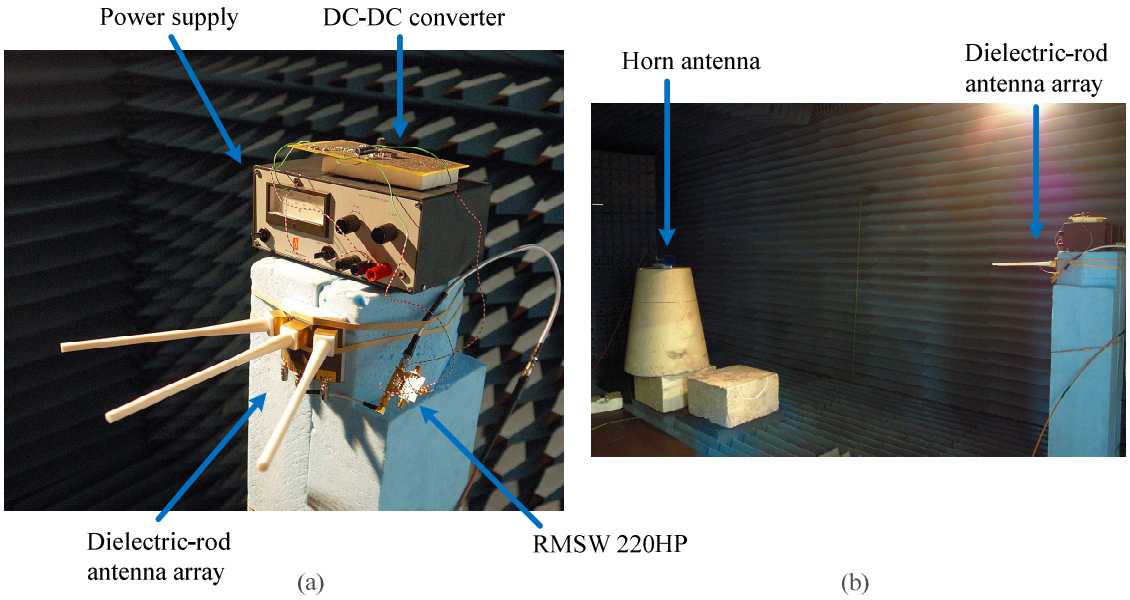

Figure 5.14. (a) Measurement setup for the switched-beam operation, and (b) radiation pattern measurement in the anechoic chamber.

5.5.1 Return loss

The measured return loss for the combined rod antenna array and RF MEMS switch is shown in Figure 5.15. It can be seen that in the bandwidth of interest, the return loss is lower than -10 dB. Note that this measured value includes the influence of the soldering and SMA connector.

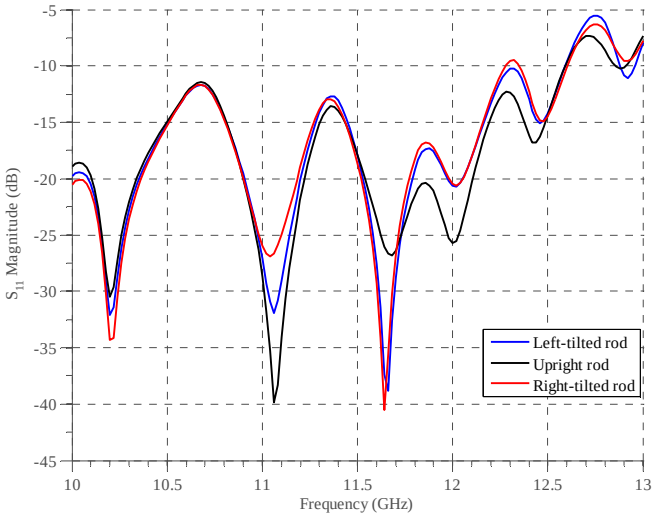

Figure 5.15. Measured return loss for the combined rod antenna array and RF MEMS switch (RMSW 220 HP)

5.5.2 HPBW, far-field pattern, and antenna gain

The measured radiation pattern of the combined antenna and MEMS switch is shown in Figure 5.16. The result without the MEMS switch is also shown for the comparison. It can be seen that a gain reduction of about 3 dB is observed. This reduction is because of the insertion loss of the MEMS switch as predicted in section 5.3. However, the radiation pattern of the antenna is not deteriorated by the presence of the switch, and the switched-beam operation is feasible by means of the MEMS switch. Also, the result for the other beams is similar to this.

For the designed 60-GHz SP3T, the insertion loss of the MEMS switch is lower than 1 dB (i.e. 0.76 and 0.99 dB) (see Table 3.4). Note that this value has been obtained for the whole MEMS structure including the packaging and via transition. Therefore, the designed switched-beam antenna array in the 60 GHz is feasible and will give better performance using the designed RF MEMS.

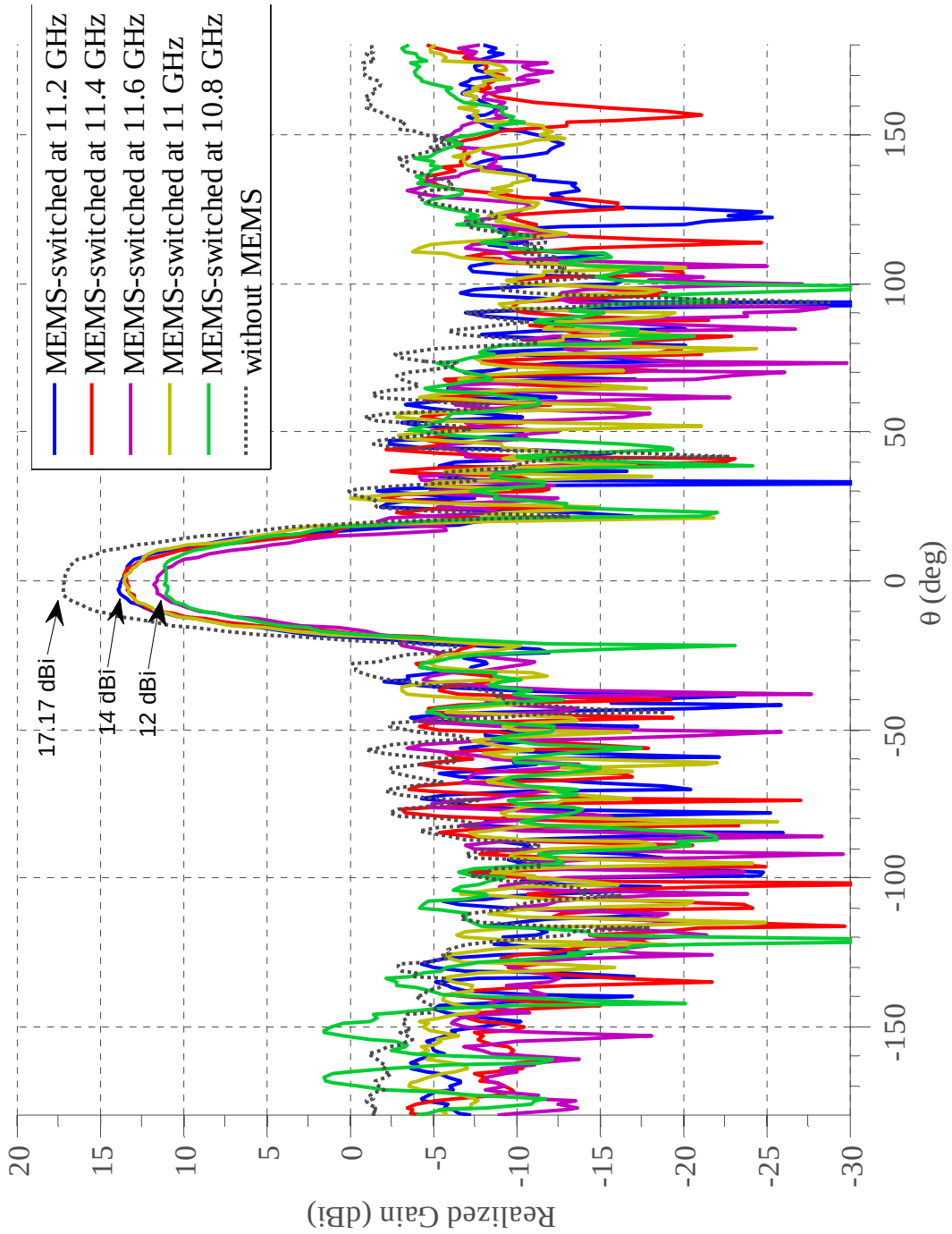

Figure 5.16. Measured radiation pattern for the combined rod antenna array and MEMS switch. The magnitude of the realized gain is also given for different frequencies.

CHAPTER 6

6 Conclusions and future works

6.1 Conclusions

The 60 GHz dielectric-rod antenna array and the RF MEMS switch have been designed. The prototype of the antenna design is suitable or can be adapted for applications in millimeter-wave frequency band. The array structure of the antenna is made conformal in a way that switched-beam antenna with a broad scan range can be realized. For the feeding type, the finite ground coplanar waveguide (FGCPW) is used. The dimension of the FGCPW feedline is designed with the transition section in such a way it can be conveniently connected to the structure of the RF MEMS switch with very less discontinuity.

The characterization of the antenna and the RF MEMS switch at 60 GHz is done by the simulation. Each antenna element has up to 18 dB realized gain, 20° beamwidth, and 6.7 % bandwidth around 60 GHz. This high-gain 60-GHz antenna can be realized in a small dimension. The coupling between adjacent antenna elements is as low as -40 dB for the array structure for both 20° and 40° angular distances between the elements. The antenna has a symmetrical radiation pattern and very low side-lobe levels in both E- and H-planes. From the simulation, it is also shown that the isolation between antenna element is more RF MEMS limited, which is around -30 dB. The insertion loss of the MEMS is lower than 1 dB, and its operation frequency is from 48 to 67 GHz.

For the implementation of this switched-beam antenna array, an antenna demonstrator with a frequency operation at 11.2 GHz is implemented and built. The antenna characterization through measurements has been done. The measured antenna pattern in the anechoic chamber is in good agreement with the simulated antenna structure at 11.2 GHz. Consequently, this also means that the radiation pattern of the fabricated antenna is in good agreement with the simulated antenna structure at 60 GHz. The measured antenna has ~17.2 dBi realized gain, 22° beamwidth, and 7.3% bandwidth (i.e 800 MHz). The measured coupling between adjacent antenna elements is -40 dB.

The switched-beam antenna array using dielectric rod element has shown that it can have high gain and narrow beamwidth. The high gain of the antenna is realized by using the tapered structure of the rod element and the low loss-tangent material for that rod element. Moreover in a typical narrow beamwidth antenna, the conformal structure with a broad scan range can then avoid the problem of the ray blockage. The other advantage of this antenna is its uniform performance for each element in the conformal structure. In this way, the beam at the largest angle of the scan range will not be severely degraded, like in the case of the planar patch array. It is definitely very advantageous to have a broad scan-range antenna with a uniform performance, remembering that the ITU criterion for an antenna's maximum allowed EIRP is determined from how large the maximum gain of an antenna can be during the operation.

Eventually, the designed antenna structure can be applied for a wide range of applications in millimeter-wave frequency, such as wireless high definition video/audio, ESB and firewire replacement, FMCW radar, passive and active imaging, radiometry, and home/office communication access point. Moreover, the emerging application in wireless inter-chip communication also uses the rod structure for its antenna element. The increase in popularity of the rod structure is because of its high gain that can solve the high attenuation problem in the millimeter-wave frequency band.

6.2 Recommendations and future works

The fabrication of the antena structure for millimeter-wave applications can be performed. This is because the antenna demonstrator at 11.2 GHz has shown a good performance. Moreover, it also has a similar performance as in the simulation. Therefore, the designed antenna in Chapter 2 can be fabricated as for the future work. Moreover, the designed MEMS switch in Chapter 3 can be realized at DIMES in TU Delft. However, the process flows for MEMS fabrication have to be investigated more, and the reliability (i.e. switching cycles) has to be tested.

The low-cost switched-beam antenna has a broad coverage and is suitable for the radiometric remote sensing and FMCW radar in the automotive area. The feasibility of the antenna structure can be tested for the radar application in the automotive area at 76 GHz, for

example for the detection of vulnerable road users. This detection in the blind spot of a vehicle can be realized by incorporating this high-gain rod antenna. A Dicke radiometer can also be used as the RF front-end system for this application.

The dual-dielectric rod structure can be designed for further development [12]. A lower relative permittivity (ε_r) of the dielectric material for the innermost material and gradually larger ε_r at the outer part of the rod can reduce the loss introduced by the dielectric material. For example, the foam, which is inherently a low loss material, to be the innermost material of the rod structure may improve the antenna efficiency. However, the efficiency will not be necessarily much larger than the current design, since the current rod material also exhibits very low loss tangent at the operating frequency. The promising benefit from a dual-dielectric rod structure is its low cross-polarization over a broad frequency band. This is due to the balanced hybrid condition inside the innermost dielectric material with the expense of a more difficult structure to machine. The balanced hybrid condition means a rotationally symmetrical field distribution (i.e. uniform amplitude and phase distribution) over the rod aperture. However, this characteristic is more suitable for the satellite application which fortunately is less constrained with regards to its cost requirement to manufacture. The reason for this is that the satellite communication often exploits the polarization feature (i.e. both RHCP and LHCP at the same frequency) to increase the system capacity. In this case, the balanced hybrid mode is prefered for this particular application. For consumer product applications, the balance characteristic is of less importance and costs more for manufacturing the structure.

7 References

[1] IEEE Spectrum, July 2004.

[2] M. Al Henawy and M. Schneider, “Planar antenna arrays at 60 GHz realized on a new thermoplastic polymer substrate,” Antennas and Propagation (EuCAP), 2010 Proceedings of the Fourth European Conference, July 2010.

[3] K. C. Huang and Z. Wang, “V-Band patch-fed rod antennas for high data-rate wireless communication,” IEEE Transaction on Antennas and Propagation, Vol. 54, No. 1, Jan. 2006.

[4] K. C. Huang and D. J. Edwards, “60 GHz multibeam antenna array for gigabit wireless communication networks,” IEEE Transaction on Antennas and Propagation, Vol. 54, No. 12, Dec. 2006.

[5] T. Ando, I. Ohba, S. Numata, J. Yamauchi, and H. Nakano, “Linearly and curvilinearly tapered cylindrical-dielectric-rod antennas,” IEEE Transaction on Antennas and Propagation, Vol. 53, No. 9, Sept. 2005.

[6] S. Kobayashi, R. Mittra, and R. Lampe, “Dielectric tapered rod antenna for millimeter wave applications,” IEEE Transaction on Antennas and Propagation, Vol. 30, No. 1, Jan. 1982.

[7] J. Kraus and R. Marhefka, Antennas for all applications, 3rd edition, New York: McGraw Hill, 2002.

[8] R. L. Eisenhart, “A better microstrip connector,” IEEE-MTT-S International Microwave Symposium, 1978.

[9] E. Holzman, Essentials of RF and microwave grounding, Artech House, 2006.

[10] P. Newham, “A broadband polyrod fed conical horn,” Antennas and Propagation, ICAP 89, Sixth International Conference on (Conf. Publ. No.301), 1989.

[11] J.–Y. Chung, “Ultra-wideband dielectric-loaded horn antenna with dual-linear polarization capability,” Progress in Electromagnetic Research, PIER 102, 2010.

[12] E. Lier and A. Kishk, “A new class of dielectric-loaded hybrid-mode horn antennas with selective gain: Design and analysis by single mode model and method of moments,” IEEE Transaction on Antennas and Propagation, Vol. 53, No. 1, Jan. 2005.

[13] A. Ittipiboon, L. Shafai, and E. Bridges, “A dielectric rod antenna as a high efficiency feed for reflector antennas,” Can. J. Eng., vol. 6, no. 4, 1981.

[14] C. Kumar, V. V. Srinivasan, V. K. Lakshmeesha, and S. Pal, “Design of short axial length high gain dielectric rod antenna,” IEEE Transaction on Antennas and Propagation, Vol. 58, No. 12, Dec. 2010.

[15] J. Richter and L. P. Schmidt, “Dielectric rod antennas as optimized feed elements for focal plane arrays,” in Proc. IEEE Antennas and Propag. Society Int. Symp., vol 3A, Jul. 3 to 8, 2005.

[16] J. P. Pousi, D. V. Lioubtchenko, S. N. Dudorov, J. A. Mallat, and A. V. Räisänen, “High permittivity dielectric rod waveguide antenna for 110-150 GHz,” Antennas and Propagation, EuCAP, 2006.

[17] K. C. Huang and D. J. Edwards, Millimetre wave antennas for gigabit wireless communications: A practical guide to design and analysis in a system context, 1st edition, Wiley, 2008.

[18] T. Weiland, “A discretization method for the solution of Maxwell's equations for six-component fields,” Electronics and Communication (AEÜ), Vol. 31, No. 3, 1977.

[19] T. Weiland, “RF & microwave simulators – From component to system design,” 33rd European Microwave Conference EUMA, 2003.

[20] C. C. Cutler, A. P. King, and W. E. Kock, “Microwave antenna measurements,” Proceeding of the IRE, Dec. 1947.

[21] C. Salema, C. Fernandes, and R. K. Jha, Solid dielectric horn antennas, Artech House Inc., 1998.

[22] W. L. Stutzman and G. A. Thiele, Antenna theory and design, 2nd ed., John Wiley & Sons, Inc, 1998.

[23] K. Sato, T. Manabe, T. Ihara, H. Saito, S. Ito, T. Tanaka, K. Sugai, N. Ohmi, Y. Murakami, M. Shibayama, Y. Konishi, and T. Kimura, "Measurements of reflection and transmission characteristics of interior structures of office building in the 60-GHz band,” IEEE Transactions on Antennas and Propagation, 45(12), December 1997.

[24] P. F. M. Smulders, “Exploiting the 60 GHz band for local wireless multimedia access: Prospects and future directions,” IEEE Communications Magazine, January 2002.

[25] P. van de Mortel, Multi sensor blind spot system, Graduation paper, Eindhoven University of Technology, The Netherlands, 2011.

[26] G. M. Rebeiz and J. B. Muldavin, “RF MEMS switches and switch circuits,” IEEE Microwave Magazine, December 2001.

[27] J. Rizk, G. L. Tan, J. B. Muldavin, and G. M. Rebeiz, “High-isolation W-band MEMS switches,” IEEE Microwave and Wireless Components Letters, Vol. 11, No. 1, January 2001.

[28] A. Enayati, X. Rottenberg, P. Ekkels, W. de Raedt, and G. A. E. Vandenbosch, “RF-MEMs-based millimeter-wave switch for integrated antenna applications,” Antennas and Propagation (EuCAP), Proceedings of the Fifth European Conference, 2011.

[29] D. Vasilache, M. Dragoman, G. Constantinidis, Y. Psychias, F. Vladoianu, T. Kostopoulos, C. Tibeica, L. Bary, A. Cismaru, D. Neculoiu, C. Buiculescu, I. Petrini, R. Plana, A. Muller, “60 GHz band RF MEMS switch,” International Semiconductor Conference, 2006.

[30] G. M. Rebeiz, RF MEMS Theory, Design, and Technology. NewYork:Wiley, 2003.

[31] W. C. Wu, L. H. Hsu, E. Y. Chang, J. P. Starski, and H. Zirath. “60 GHz broadband 0/1-level RF-via interconnect for RF-MEMS packaging,” IET Electronics Letters, Vol. 43, No. 22, October 2007.

[32] E. K. I. Hamad, G. E. Nadim, and A. S. Omar, “A proposed SP3T wideband RF MEMS switch,” IEEE Antennas and Propagation Society International Symposium, 2004.

[33] G. L. Tan, R. E. Mihailovich, J. B. Hacker, J. F. DeNatale, and G. M. Rebeiz, “Low-loss 2- and 4-bit TTD MEMS phase shifters based on SP4T switches,” IEEE Transactions on Microwave Theory and Techniques, Vol. 51, January 2003.

[34] K. van Caekenberghe, “RF MEMS on the radar,” IEEE Microwave Magazine, October 2009.

[35] R. Chadha & K. C. Gupta. “Compensation of discontinuities in planar transmission lines,” IEEE Trans. Microwave Theory Tech., vol. MTT-30, Dec. 1982.

[36] H. Eherenspeck, W. Gerbes, and F. Zucker, “Trapped wave antennas,” IRE International Convention Record, March 1954.

[37] Y. Shiau, “Dielectric rod antennas for millimeter-wave integrated circuits,” IEEE Transactions on Microwave Theory and Techniques, Nov. 1976.

[38] G. E. Mueller and W. A. Tyrrell, “Polyrod antennas,” Bell System Tech. J., 837-851, Oct. 1947.

[39] S. Y. Stroobandt, “An X-band high-gain dielectric rod antenna,” Report, Katholieke Universiteit Leuven, August 1997.

[40] R. Ala, R. Sadeghzadeh, and R. Kazemi, “Two-layer dielectric rod antenna for far distance,” Antennas and Propagation Conference (LAPC), Loughborough, 2010.

[41] J. R. James, “Engineering approach to the design of tapered dielectric-rod and horn antennas,” Radio and Electronic Engineer, June 1972.

[42] R. B. Watson and C. W. Horton, “The radiation patterns of dielectric rods—experiment and theory,” Journal of Applied Physics, July 1948.

[43] T. Tatsukawa, A. Doi, M. Teranaka, H. Takashima, F. Goda, T. Idehara, T. Kanemaki, S. Nishizawa, and T. Namba, “Characteristics of a teflon rod antenna for millimeter- and submillimeter-wave irradiation on living bodies,” Japanese Journal of Applied Physics, Volume 42, Issue 11, pp. 7147, 2003.

[44] A. C. Studd, “Towards a better dielectric rod antenna,” ICAP 91., Seventh International Conference on (IEE) Antennas and Propagation, 1991.

[45] E. Niver, “Tapered dielectric rod antenna,” Complex Computing-Networks: Springer Proceedings in Physics, Volume 104, Part I, 113-121, 2006.

[46] H. Chen, “Fast methods for millimeter-wave dielectric resonator and antenna analysis and design,” M.Sc. thesis, University of Waterloo, Canada, 2009.

[47] J.–Y. Chung and C. C. Chen, “Ultra-wide bandwidth two-layer dielectric rod antenna,” IEEE Transactions on Antennas and Propagation, June 2008.

[48] J.–Y. Chung and C. C. Chen, “Two-layer dielectric rod antenna,” IEEE Transactions on Antennas and Propagation, June 2008.

[49] A. Elsherbini, C. Zhang, S. Lin, M. Kuhn, A. Kamel, A. E. Fathy, and H. Elhennawy, “UWB antipodal vivaldi antennas with protruded dielectric rods for higher gain, symmetric patterns and minimal phase center variations,” IEEE Antennas and Propagation Society International Symposium, 2007.

[50] J. A. G. Akkermans, “Planar beam-forming antenna array for 60-GHz broadband communication,” Ph.D. dissertation, Eindhoven University of Technology, 2009.

[51] CST Computer Simulation Technology, Darmstadt, Germany, *CST Microwave Studio.* http://www.cst.com.

[52] P. F. M. Smulders, “Impact of regulations on feasible distance between 60 GHz devices,” 4th European Conference on Antennas and Propagation, EuCAP, April 2010.

[53] P. F. M. Smulders, “Statistical characterization of 60-GHz indoor radio channels,” IEEE Transactions on Antennas and Propagation, Oct. 2009.

[54] M. D. Huang, M. H. A. J. Herben, and M. I. Kazim , “Design of cylindrically bent antenna array on LCP substrate with large coverage at 60 GHz,” 5th European Conference on Antennas and Propagation EuCAP, April 2011.

[55] M. D. Huang and M. H. A. J. Herben, ” Effects of bending a planar antenna array on its scan performance,” 4th European Conference on Antennas and Propagation EuCAP, April 2010.

[56] B. A. Smolders, "Integration of antennas at microwave/mm-wave frequencies,” in Proceedings of the URSI/NERG winter meeting "High-Frequency Wireless (MM-SUBMM),” January 2010.

[57] Sapphire (Al_2O_3), http://www.mt-berlin.com/frames_cryst/descriptions/sapphire.htm.

[58] Silicon Nitride, Si_3N_4 Material Properties, http://accuratus.com/silinit.html.

[59] M. D. Huang, M. I. Kazim, and M. H. A. J. Herben, “Characterization of the relative permittivity and homogeneity of Liquid Crystal Polymer (LCP) in the 60 GHz band,” EURO-COST 2100, November 23-25, 2010.

[60] D. C. Thompson, O. Tantot, H. Jallageas, G. E. Ponchak, M. M. Tentzeris, and J. Papapolymerou, “Characterization of liquid crystal polymer (LCP) material and transmission lines on LCP substrates from 30 to 110 GHz,” IEEE Trans. Microwave Theory Tech., vol. 52, no. 4, pp. 1343–1352, April 2004.

[61] X. Zhang, “Design, fabrication and characterization of microwave passive devices on liquid crystal polymer substrates,” Ph.D. dissertation, Chalmers University of Technology, 2009.

[62] D. Pozar, Microwave Engineering, Chicester: Wiley, 3rd ed., 2005.

[63] N. K. Das, S. M. Voda, and D. M. Pozar, “Two methods for the measurement of substrate dielectric constant,” IEEE Trans. Microwave Theory Tech., vol. 35, no. 7, pp. 636-642, July 1987.

[64] J. A. G. Akkermans, R. van Dijk, and M. H. A. J. Herben, “Millimeter-wave antenna measurement,” in European Microwave Conf. (EuMC07), Munich, October 2007.

[65] E. Rius, J. P. Coupez, S. Toutain, C. Person, and P. Legaud, “Theoretical and experimental study of various types of compensated dielectric bridges for millimeter-wave coplanar applications,” IEEE Trans. Microwave Theory Tech., vol. 48, no. 1, Jan. 2000.

[66] I. Wolff, Coplanar Microwave Integrated Circuits, Wiley, 2006.

[67] B. C. Wadell, Transmission Line Design Handbook, Artech House, Inc, 1991.

[68] X. Wang, L.-H. Lu, and C. Liu, “Micromachining techniques for liquid crystal polymer,” The 14th IEEE International Conference on Micro Electro Mechanical Systems (MEMS), 2001.

[69] X. Wang, J. Engel, and C. Liu, “Liquid crystal polymer (LCP) for MEMS: Processes and applications,” Journal of Micromech. Microeng. 13, pp. 628-633, 2003.

[70] J.–F. Zürcher, “A meander-line polarizer covering the full E-band (60-90 GHz),” Microwave and Optical Technology Letters, vol. 18, no. 5, Aug. 1998.

[71] C. A. Balanis, “Measurements of dielectric constants and loss tangents at E-band using a Fabry-Perot interferometer,” NASA technical note, NASA TN D-5583, Dec. 1969.

[72] J. Richter, J. Garbas, and L. Schmidt, "Mean and differential phase centers of rectangular dielectric rod antennas," 34th European Microwave Conference, 2004.

[73] S. Hanham, T. Bird, and B. Johnston, "A ring slot excited dielectric rod antenna for terahertz imaging," IEEE Antennas and Propagation Society International Symposium, 2007.

[74] J. Richter, M. Muller, L.-P. Schmidt, “Measurement of phase centers of rectangular dielectric rod antennas,” IEEE Antennas and Propagation Society International Symposium, 2004.

[75] W.-G. Kim, J. P. Thakur, and Y.-H. Kim, "Efficient DRW antenna for quasi-optics feed in W-band imaging radiometer system," Microwave and Optical Technology Letters, vol. 52, no. 5, May 2010.

[76] J. B. Andersen, "Radiation from surface-wave antennas," IEEE Electronics Letters, June 1967.

[77] J. R. James, "Comment: Radiation from surface-wave antennas ," IEEE Electronics Letters, July 1967.

[78] S. M. Hanham, T. S. Bird, A. D. Hellicar, and R. A. Minasian, "Optimized dielectric rod antennas for terahertz applications," 34th International Conference on Infrared, Millimeter, and Terahertz Waves (IRMMW-THz), 2009.

[79] T. P. Nguyen, C. Pichot, C. Migliaccio, and W. Menzel, "Study of folded reflector multibeam antenna with dielectric rods as primary source," IEEE Antennas and Wireless Propagation Letters, 2009.

[80] S. M. Hanham, T. S. bird, B. F. Johnston, A. D. Hellicar, and R. A. Minasian, "A 600 GHz dielectric rod antenna," 3rd European Conference on Antennas and Propagation (EuCAP), 2009.

[81] S.-S. Qian, L. Xing-guo, and W. Ben-qing, "Ka band Cassegrain monopulse antenna fed by tapered rod antennas," 8th International Symposium on Antennas, Propagation and EM Theory (ISAPE) 2008.

[82] S. M. Hanham and T. S. Bird, "High efficiency excitation of dielectric rods using a magnetic ring current," IEEE Transactions on Antennas and Propagation, June 2008.

[83] I. L. Morrow, P. S. Hall, and J. S. Dahele, "The contribution of J.R. James to dielectric rod and other novel antennas," The Second European Conference on Antennas and Propagation (EuCAP), 2007.

[84] P. J. B. Clarricoats and K. B. Chan, “Propagation behaviour of cylindrical-dielectric-rod waveguides,” Proceedings of the IEE, vol. 120, no. 11, pp. 1371 – 1378, 1973.

[85] K. Okamoto. Fundamentals of Optical Waveguides. Academic Press, 2000.

[86] N. Skou and D. L. Vine, Microwave Radiometer Systems: Design and Analysis. 2ed., Artech House, 2006.

[87] P. Bhartia, I. Bahl, R. Garg, and A. Ittipiboon, Microstrip Antenna Design Handbook, Artech House, 2000.

[88] H,-M. Chen, Y.-F. Lin, P.-S. Cheng, H.-H. Lin, C. T. P. Song, and P.S. Hall, "Parametric study on the characteristics of planar inverted-F antenna," IEE Proceedings - Microwaves, Antennas and Propagation, Dec. 2005.

[89] http://www.qpigroup.com/resources/images/HDI%20lay-out.png.

[90] C. A. Balanis, Antenna Theory: Analysis and Design, Wiley, 3ed., 2005.

[91] J. R. James and P. S. Hall, Handbook of Microstrip Antennas, Peter Peregrinus Ltd., 1989.

[92] T. H. Lee, Planar Microwave Engineering: A Practical Guide to Theory, Measurement, and Circuits, Cambridge University Press, 2004.

[93] G. Kompa, Practical Microstrip Design and Applications, Artech House, 2005.

[94] A. P. de Hek. Akkermans, “Design, realization and test of GaAs-based monolithic integrated X-band high-power amplifiers,” Ph.D. dissertation, Eindhoven University of Technology, 2002.

[95] R. Chadha and K. C. Gupta, "Compensation of discontinuities in planar transmission lines," IEEE Transactions on Microwave Theory and Techniques, Dec. 1982.

[96] J. H. Lee, S. Hong, W. K. Kim, J. W.An, and M. Y. Park, “A switched array antenna modul for millimeter-wave wireless communications,” IEEE Global Symposium on Millimeter Waves (GSMM), April 2008.

[97] M. Steer and W. D. Palmer, Multifunctional Adaptive Microwave Circuits and Systems, SciTech Publishing, Inc., 2009.

[98] http://www.radantmems.com/radantmems/index.html.

[99] D. Leenaerts, J. van der Tang, and C. Vaucher, Circuit Design for RF Transceivers, Kluwer Academic Publishers, 2001.

[100] C. M. Ta, E. Skafidas, R. J. Evans, and C. D. Hoang, "A 60-GHz variable delay line on CMOS for steerable antennae in wireless communication systems," Canadian Conference on Electrical and Computer Engineering (CCECE), July 2008.

[101] P. Osterberg, H. Yie, X. Cai, J. White, and S. Senturia, “Self-consistent simulation and modeling of electrostatically deformed diaphragms,” IEEE Workshop on Micro Electro Mechanical Systems, Jan. 1994.

[102] T. Röttgers, Humidity Tests on Rohacell HF – Dielectric Properties, P62-BI Rgr/Rke, Röhm GmbH, April 1992.

8 Appendices

8.1 Project based management

8.1.1 Introduction

The Detection of Vulnerable Road User (DEVURO) project is financed by the Dutch funding agency for university research (STW). The main contribution to this project is to design and manufacture switched-beam antenna array that can work at millimeter-wave frequency, particularly at 60 GHz. Therefore, the resulting design can be used for consumer product applications at the 60-GHz frequency band.

This antenna has to have high gain and broad scan range and low-cost production. To support a very broad scan range with constant performances, a novel conformal structure of the rod antenna is designed in this project. The switched-beam capability of this antenna is supported by the designed RF MEMS switch. This antenna system can be integrated to the MMIC front-end system. Moreover, it can be applied for various applications in the millimeter-wave frequency band, e.g. 24- and 76-GHz radar applications, 60-GHz indoor communication, and radiometry application. Also, the antenna can be used for detecting vulnerable road users (i.e. radar) in a vehicle's blind spot. In addition to radar, the antenna prototype can also be used for other consumer applications such as wireless home video server, real-time HD audio delivery, or home backbone. Therefore, the resulting prototype is not application-specific.

The project has been successfully finalized. The measurement, test, and characterization of the antenna system have been done in the anechoic chamber of Electromagnetics (EM) Group at TU/e.

8.1.2 Problem description

The limited coverage of wireless communication at the millimeter-wave frequency band due to large free-space path loss, i.e. large signal attenuation, has been a major problem. Furthermore, shadowing and small scale fading may reduce the received signal even more. Moreover, the number of owned wireless devices per user has been ever increasing. Not only will the wireless devices connect people to people, but also people to machines and machines to machines. Thus, the limited bandwidth around 2.4 GHz (ISM-band) cannot support the higher data rate if the band has to be shared among many potential users. The availability of 7 GHz around 60 GHz (ISM-band) is able to accommodate high data rate communication. Furthermore, the propagation condition in the 60-GHz wireless channel enables frequency reuse. This frequency reuse is mainly enabled due to the large amount of path losses experienced by the propagating electromagnetic waves. Therefore, the electromagnetic wave does not interfere with other waves generated by the neighboring 60-GHz wireless systems.

However, this interesting property comes not only with this advantage. In this frequency band, the wave is highly attenuated so that the front-end devices of the receiver end have to be very sensitive, otherwise the wave will be effectively undetected. This situation thus limits the communication distance or range of 60-GHz and other millimeter-wave applications.

A high gain antenna with a broad scan range is proposed in this project as a solution to the aforesaid problem. Furthermore, its performance should be uniform over the scan range.

8.1.3 Goal and results

The ultimate goal of this project is to design an antenna system for millimeter-wave application. The designed antenna prototype has to have high gain and broad scan range. The manufacturing cost is one of the considerations to realize a competitive product in the market of millimeter-wave application. In the following, the deliverables for this project are listed.

The deliverables of the project will be:

1. Definition of the design specification.
2. Simulation result.
3. Measurement result.
4. A manufactured prototype of the antenna.

5. Test and measurement results of the antenna system (antenna & RF MEMS switch).
6. Report on the design and the result.
7. Final presentation.

Moreover, the reports include:

1. Study of the several antenna structures that can meet the requirements and specifications (in a separated report).
2. The design flow and the necessary analysis of the antenna and RF MEMS.
3. Simulation methodology, verification, and results of the antenna and RF MEMS.
4. Fabrication process of the antenna demonstrator.
5. Test and measurement result of the manufactured antenna demonstrator.

The final presentation is outlined in the following:

1. Introduction.
2. System overview.
3. Simulation result.
    a. 60-GHz antenna design;
    b. Integration of the 60-GHz RF MEMS and antenna;
    c. 11-GHz antenna demonstrator.
4. Measurement result.
    a. Switched-beam antenna array at 11 GHz.
5. Conclusions.

8.1.4 Delimitation

It is not part of the project to design the whole block of communication system. Some off-the shelf components already exist. Thereby, the whole RF front-end part needs not to be built.

For this project, the demonstrator of the rod antenna is then prepared for 11-GHz operating frequency, because of the commercial availability of the RF MEMS switch at that frequency and the availability of the measurement equipment at TU/e at the time this project is performed. In addition, the size of the antenna demonstrator has to be accounted as well. However, the design of the antenna and the RF MEMS has been completed successfully at 60 GHz. Also, the delimitation of this project is that a fabrication of this MEMS will take a long technology flow and time. Hence, in this project, the MEMS design is finalized through the working simulation, with considerations for the fabrication process.

8.1.5 Project phases

The phasing plans include several steps which are needed in the project. Those are listed as follows:

1. Initialization phase
    - Kick-off meeting with the project owner and member of the project.
    - Familiarize with the working environment by attending regular formal meeting and informal discussion.
    - Set the project goal and desired result.
    - Anticipate the project risk and delimitation.
    - Make concept or initial project plan.

2. Definition phase
    - Study and research available materials for suitable antenna and RF MEMS switch design and its feasibility for intended applications.
    - Familiarize with the available simulators and the software tools.
    - Attend related tutorial or workshop for the use of the equipment.
    - Specify the antenna and the RF MEMS switch for defined applications.

3. Design phase
    - Choose the appropriate antenna and RF MEMS switch from available design.
    - Propose criteria for improvement.
    - Design and simulate the antenna and the RF MEMS switch structure.
    - Analyze and investigate the antenna and the RF MEMS switch design.
    - Define and choose the necessary equipment or device to buy or to make.

4. Preparation phase
    - Prepare the measurement setup.
    - Verify the simulation results.
    - Prepare the layout of the antenna design.
    - Anticipate for the iteration of the antenna design.

5. Realization & testing phases
    - Fabricate the antenna.
    - Test and measure the antenna and the RF MEMS switch.
    - Iteration.
    - Integrate the antenna and the RF MEMS switch.
    - Test and measure the antenna system.
    - Write the final report and prepare the final presentation.

8.1.6 Capacity and time plan

Table 8.1. Time plan: DEVURO project – Switched-beam antenna array design for millimeter-wave applications

Phases	Duration	Description	Outcomes
Initialization	4 Weeks	Literature study	Project plan v1.0
Definition	6 Weeks	Specification, literature study	Documents (introduction), simulation files
Design	8 Weeks	Simulation, optimization, analysis, report	Documents (design and analysis), simulation files
Preparation	12 Weeks	Simulation verification, measurement calibration, report	Designed prototype, simulation files, documents (simulation)
Realization & Testing	~15.8 Weeks	Fabrication, iteration, measurement setup, measurement report	Measurement files, final document (results and conclusions), demonstrator, presentation
Holiday	2 Weeks	-	-
Total	47.8 Weeks		

Table 8.2. Gantt chart for project phases and involved capacity.

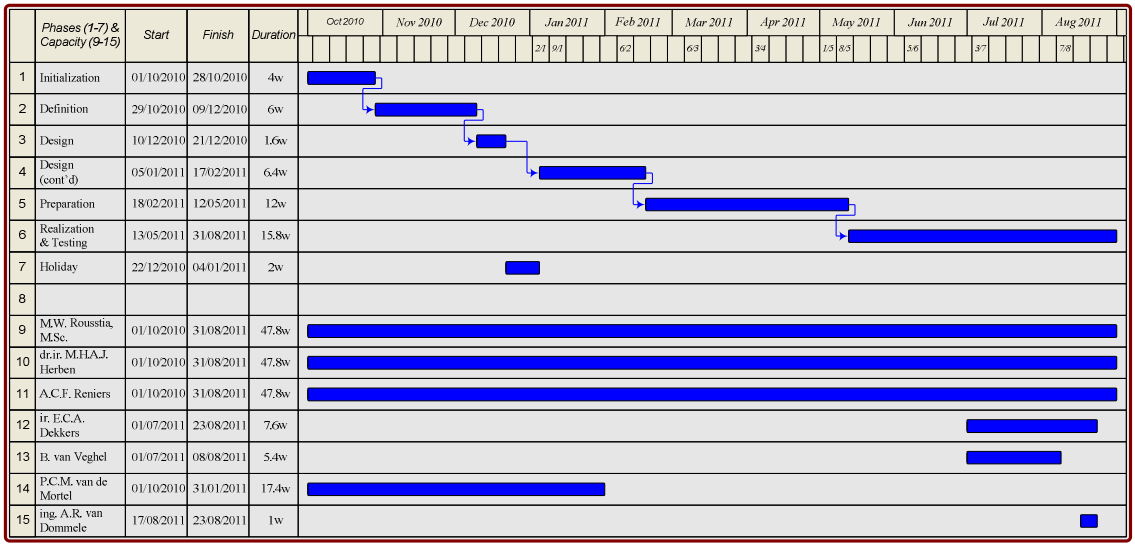

8.1.7 Organization

The people and company who are involved in this project are as follows (see Figure 8.1):

1. M. W. Rousstia, MSc: designer from TU/e Electromagnetics Group;
2. Prof. Dr.-Ing. L. M. F. Kaufmann: director of SAI-ICT program at TU/e;
3. dr. ir. M. H. A. J. Herben: scientific researcher and supervisor from TU/e Electromagnetics Group;
4. A. C. F. Reniers: supervisor and lab expert from TU/e Electromagnetics Group;
5. ing. A. R. van Dommele: technical staff and measurement expert at TU/e Electromagnetics Group;
6. P. C. M. A. van de Mortel: MSc-student at TU/e Electromagnetics Group;
7. ir. E. C. A. Dekkers: designer and manufacturer from GTD; and
8. B. van Veghel: manufacturer from QPI Group in Helmond.

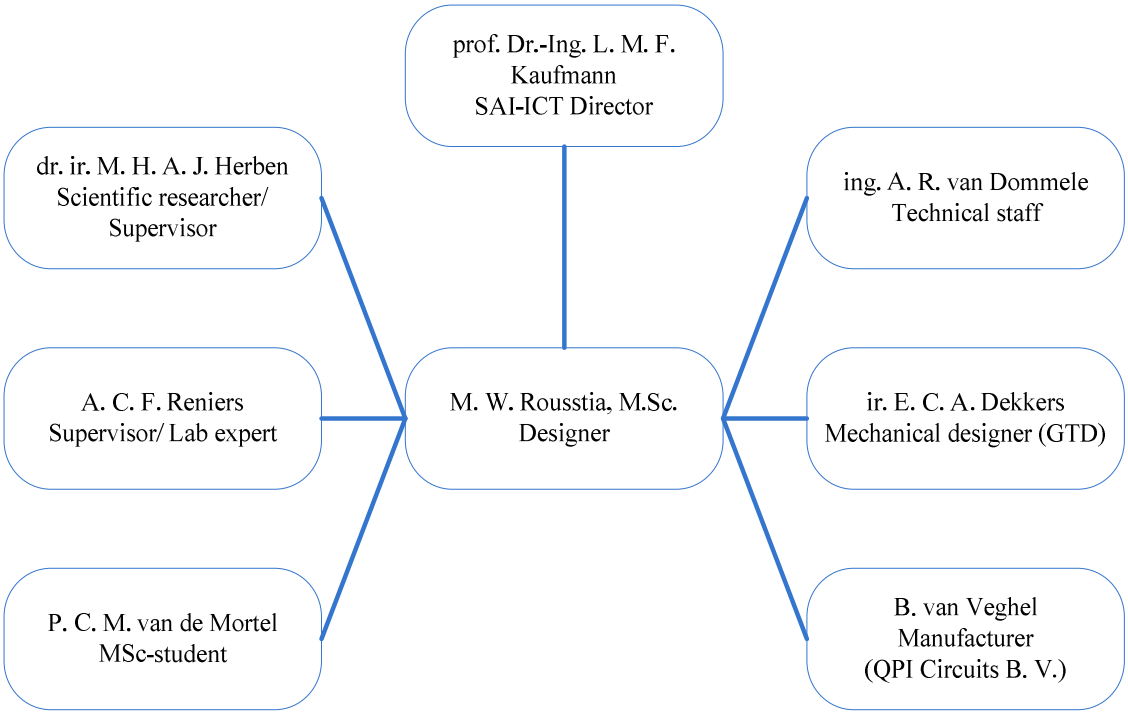

Figure 8.1. Project organization.

8.1.8 Money

1. Salary of the designer: 1681 €/month (gross).
2. Salary of the involved experts in the project: Professor: 6k €/month (gross).
3. Overhead cost: office room, office equipment, electricity, maintenance, etc (~200 €/month).
4. Shared license of a simulation software (~10k €/year).
5. Cost of the computer to perform simulation (> 2k €).
6. Cost of used equipments and devices (RF MEMS evaluation board: 550 US$, electronic components as shown in Figure 8.6(b): 93.2 €, connectors: 9 x 3.76 € = 33.8 €).
7. Fabrication and manufacturing expenses (planar fabrication: 800 €, drawing: 16 hours x 35 € = 560 €, launchers: 120 €, holders+stand+rods= 200 €).
8. Travel expense (< 10 €).

The PDEng traineeship is cofinanced by the Dutch Ministry of Education and Electromagnetics Group at TU/e (i.e. the second year project). The total estimate of the traineeship is in the amount of 120k €.

The earlier paragraph summarizes the involved cost for fabrication of the antenna demonstrator. For the 60-GHz design, some expenses for the initial development can be estimated:

- MEMS fabrication (e.g. at DIMES, TU Delft) (including process flows + development + test) is ~ 5k-30k €.
- Antenna fabrication is comparable to the cost for the demonstrator (see remarks in the following paragraph).
- The new measurement setup: VNA/network analyzer: ~200k US$; anechoic chamber: 60k €; cables, motor, etc: 10k €.

For the antenna fabrication, the used materials play an important role in determining its cost. Basically, the LCP material is a low cost material (~5 US$/ft^2), but its yield product can be as low as 10% due to the blistering. This blistering may dramatically increase its cost, if stacked LCP panels are used without care. In the design, only 2 stacked panels are needed, and the panel area is 4x5 mm^2 per element. A small area can decrease the probability that blistering may occur. Although the cost of the LCP material is not yet competitive with very low cost FR-4 material, it is expected that its cost will drop as the production level grows. Moreover, the cost of the 3D-structure in the antenna part is reported to be in the order of few cents for a large-scale production. The PS material for the rod has a low cost as well.

Probably, the cost from the MEMS part is the main determinant for manufacturing a low-cost switched-beam antenna. While MEMS switches have the potential for very low cost manufacturing in a large scale production, one must add the cost of packaging. In this design, the hermetic cavity sealing (single-chip packaging) is used. With this technique, achieving cost efficiency and high productivity are recently reported to be possible. An additional cost

comes from the high-voltage drive chip. Only one inductor is used for this chip as seen in Figure 8.6(b), and this inductor requires a large area in a chip production. Since the cost of a chip is determined by the used area in a particular technology e.g. 65 nm (6 cents € / 2.5mm^2), the use of the inductor has to be minimized. Although, all those efforts, it is still hard to beat a US$0.3-0.6 diode switch (tested, packaged, and delivered).

Despite its broadband characteristic, the flip-chip technology used for attaching the MEMS to the antenna board costs 1.5 to 5 times more than the counterpart bondwire. However, the production of this MEMS can be done altogether with the other RF front-end devices to reduce its production cost. Finally, the target market determines the profit of a product. As this antenna is designed for applications in the consumer product, a low-cost product is necessary.

8.1.9 Quality

To meet the quality of the designed prototype, several activities are performed:

1. The results and the delimitations are clearly mentioned in the baseline document and have been approved by the supervisors and project owner;
2. A sufficient amount of time has to be reserved for iterations of the design;
3. The prototype's specification has to be verified or maintained during the design steps;
4. The prototype has to be tested in an anechoic chamber and with the pre-calibrated measurement devices.

8.1.10 Progress control

1. Internal reports and presentations are delivered every progress meeting with dr. ir. M. H. A. J. Herben and A. C. F. Reniers. The progress meeting is performed, at least, once per month.
2. The informal meeting and discussion are performed with the lab expert during the measurement or per email.
3. The baseline document is evaluated by the Project Based Management coach.
4. The final report will be evaluated by the supervisors and the SAI-ICT director.

8.1.11 Risk list and risk management

Table 8.3. Possible risks and their priorities.

Possible Risks	Effect	Occurrence	Priority
Room/equipment unavailable	3	1	3
Inaccuracy simulation	3	2	6
Inaccuracy in measurement result	3	3	9
Simulator unavailable	2	1	2
Supervisor unavailable	3	2	6

Priority= Severity * Occurrence

whereby:

Effect: 1-low; 2-medium; 3-high

Occurrence: 1-rare; 2-sometimes; 3-frequently

Table 8.4. Risk management plan.

Possible Risks	Management Plan	Is it done?
Room/equipment unavailable	Discussion and early arrangement	Yes
Inaccuracy in simulation	Comparing with other available simulation approaches, using high accuracy simulation criteria	Yes
Inaccuracy in measurement result	Reserving time for iteration, performing calibration	Yes
Simulator unavailable	Consulting with experts in the field, looking into other available simulators	Yes
Supervisor unavailable	Anticipation of the supervisors' leaving and holiday plan	Yes

8.2 Antenna demonstrator

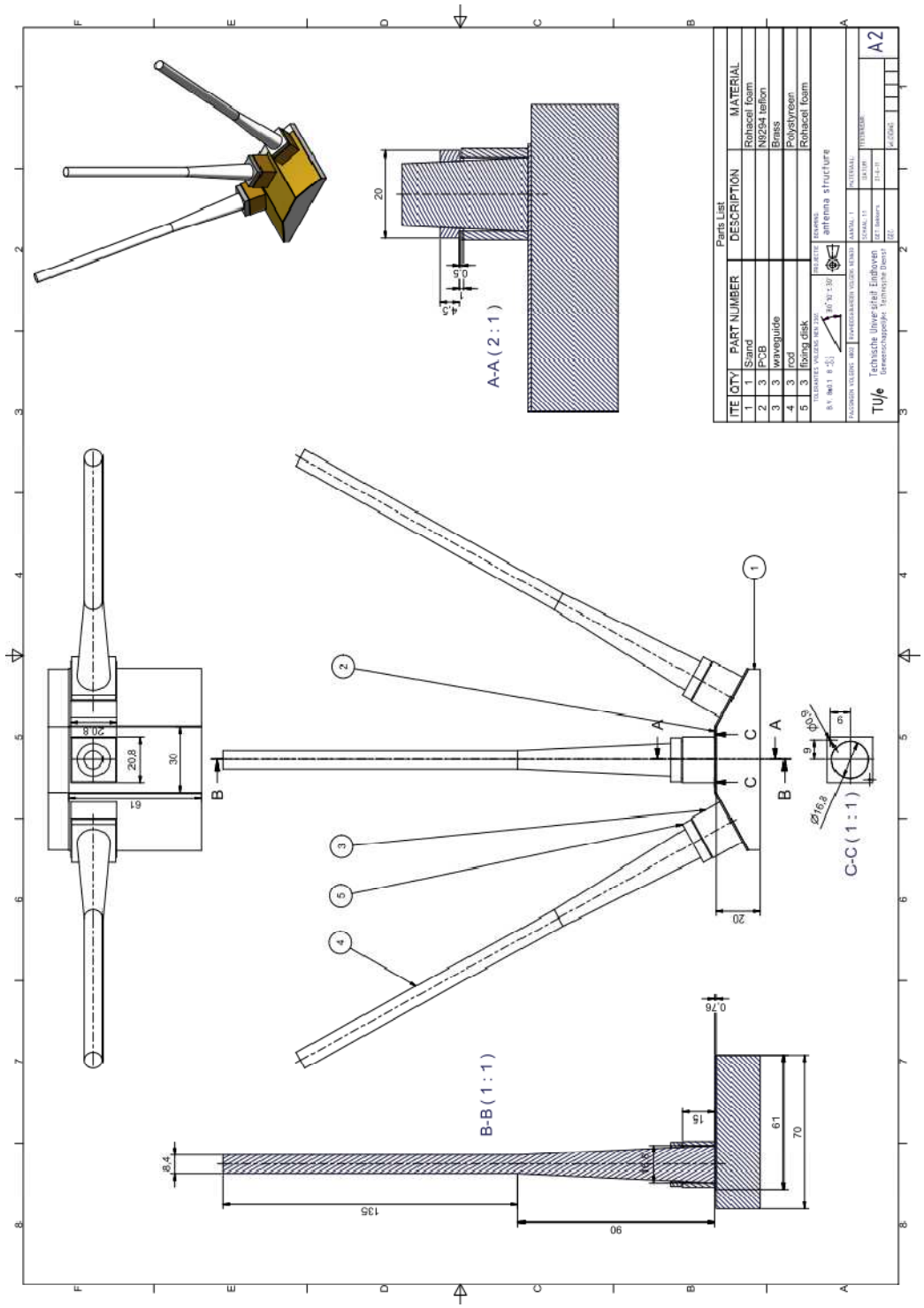

Figure 8.2. Structure of the 11-GHz antenna demonstrator.

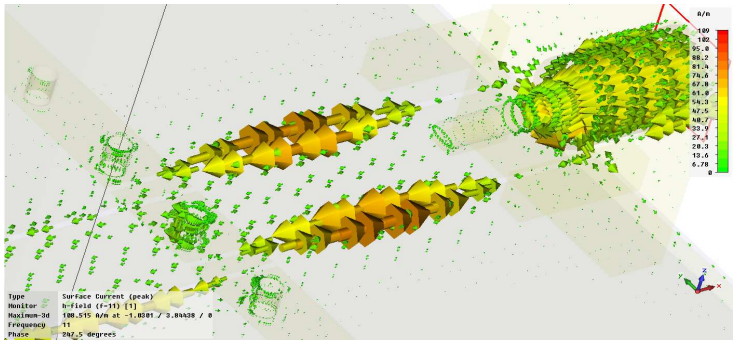

Figure 8.3. Surface current of the transition using the SMA connector

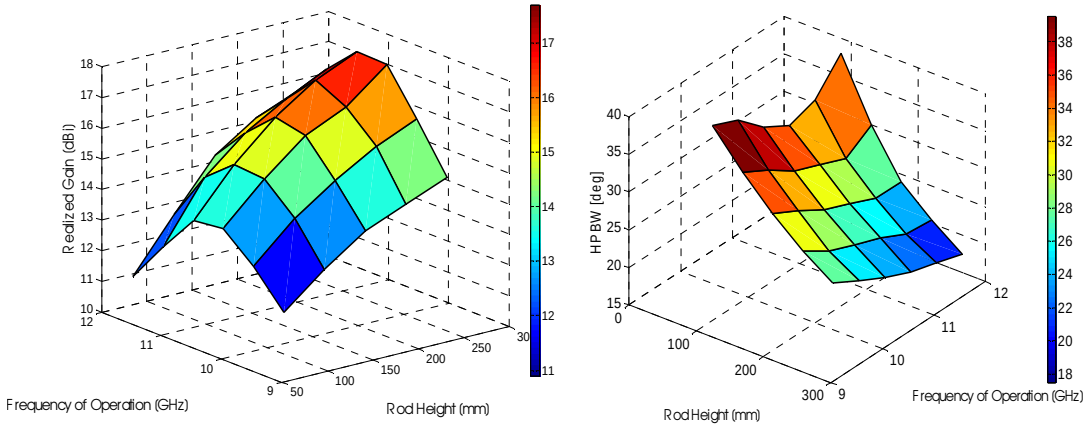

(a) (b)

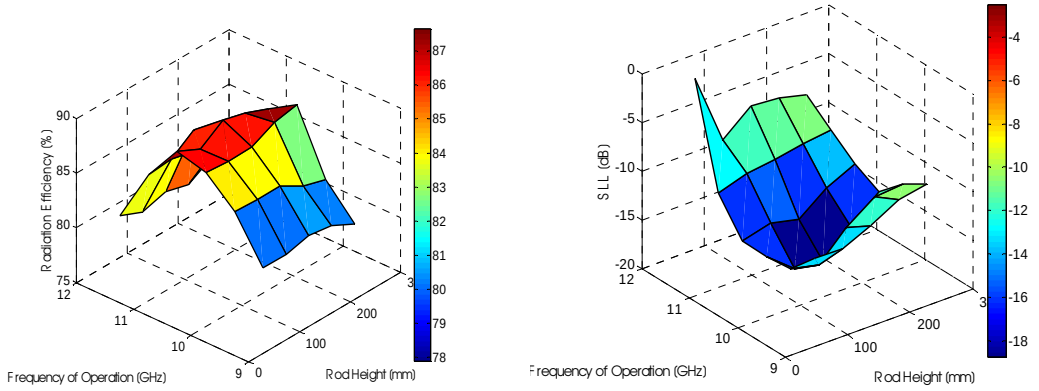

(c) (d)

Figure 8.4. Design template for various heights of the cylindrical rod (h_{cr}) in the frequency range from 9.5 to 12 GHz: (a) the realized gain (at θ = 0°) for φ = 90°, (b) the half power beamwidth for φ = 90°, (c) the radiation efficiency, and (d) the sidelobe level for φ = 90°. The rod height in figures is h_{cr} for the antenna demonstrator (f_o = 11 GHz).

Figure 8.2 shows the detailed structure of the antenna demonstrator including its dimensions and materials. Points 1 to 5 are the stand, the PCB, the launcher, the rod, and the holder, respectively. Figure 8.3 shows the surface current during the transition from the SMA connector to the CPW. The surface current tends to have larger magnitude in the outer part of the conductors. Figure 8.4 provides the design template for the antenna demonstrator.

8.3 DC-DC converter for actuating the MEMS

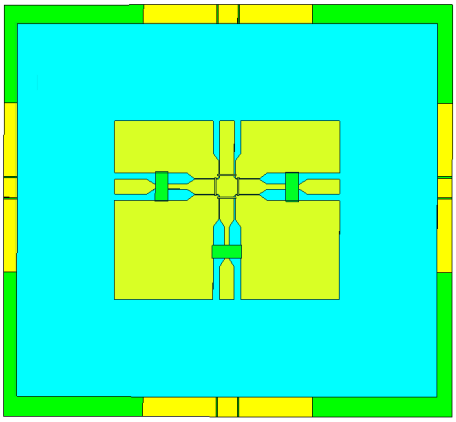

Figure 8.5. Bird's-eye view of the SP3T.

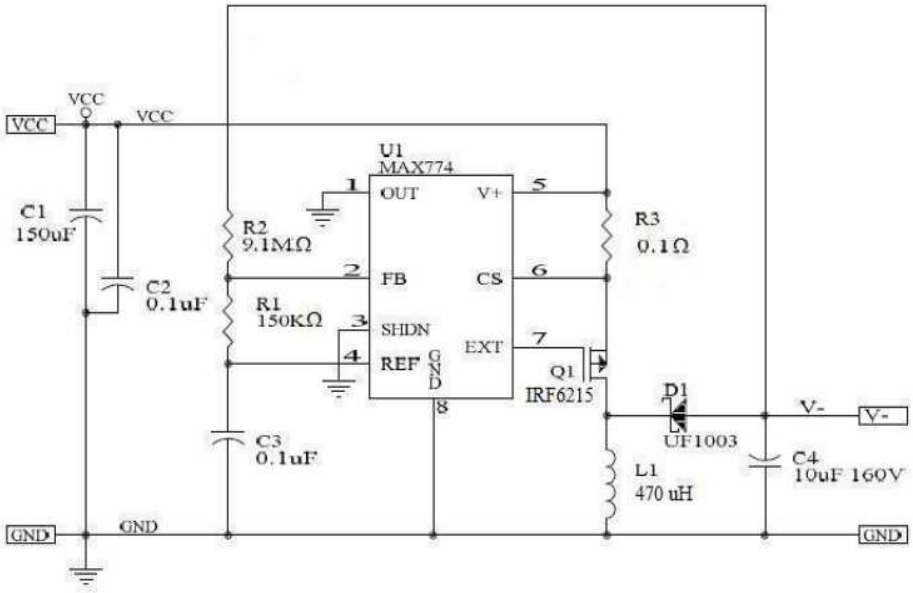

(a)

Item	Ref. Des.	Description	Part Number	Manufacturer	Quantity	Package
1	U_1	Adjustable DC-to-DC controller	MAX774CSA	Maxim IC	1	SMD8A
2	Q_1	P-Channel MOSFET, 150V, 13A	IRF6215LPBF	International Rectifier	1	TO-262
3	D_1	Ultra-fast rectifier diode, 1A	UF1003-T	Diodes, Inc.	1	DO-41
4	R_1	150 kΩ, 0.25W resistor	N/A	Generic	1	1206
5	R_2	9.1 MΩ, 0.25W resistor	N/A	Generic	1	1206
6	R_3	0.1Ω, 1W, 5% current sense resistor	RW1S0BAR100JE	Ohmite	1	2512
7	C_1	150 µF, 10V, 100mΩ ESR tantalum capacitor	495-1531-1	Kemet	1	2917
8	C_2, C_3	0.1 µF, 50V, polyethylene capacitor	PCF1148CT	Panasonic ECG	2	1913
9	C_4	10 µF, 160V, aluminum electrolytic capacitor	AEB106V10	Cornell Dubilier Electronics	1	6767P
10	L_1	470 µH, 580 mA, 690 mΩ shielded inductor	ELL-CTV471M	Panasonic Electronic Components	1	12 mm W X 12 mm L X 4.2 mm T

(b)

Figure 8.6. (a) Schematic of the MAX774 DC-to-DC converter, and (b) the list of its components.

The RF MEMS switch (SP3T) in Figure 8.5 requires a DC-DC converter to actuate the MEMS. Figure 8.6(a) shows the schematic of that converter. It is based on Maxim IC MAX774, which takes a +5 V_{dc} input and converts it to a -90 V_{dc} output. Figure 8.6(b) lists all the components to build the converter for a demonstration (see Figure 8.7). To build a commercialized MEMS, this converter is integrated into a chip together with the MEMS structure.

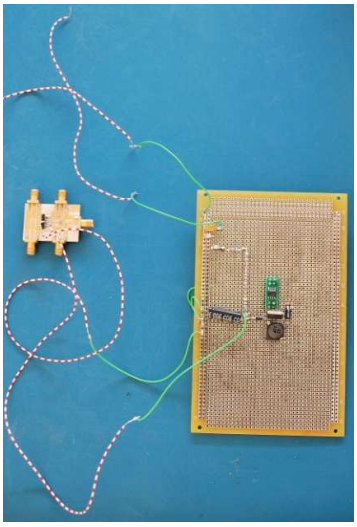

Figure 8.7. MAX774 DC-to-DC converter (the right board) used in the measurement setup for actuating the MEMS switch (the left board).

8.4 System overview of the 60-GHz wireless communication

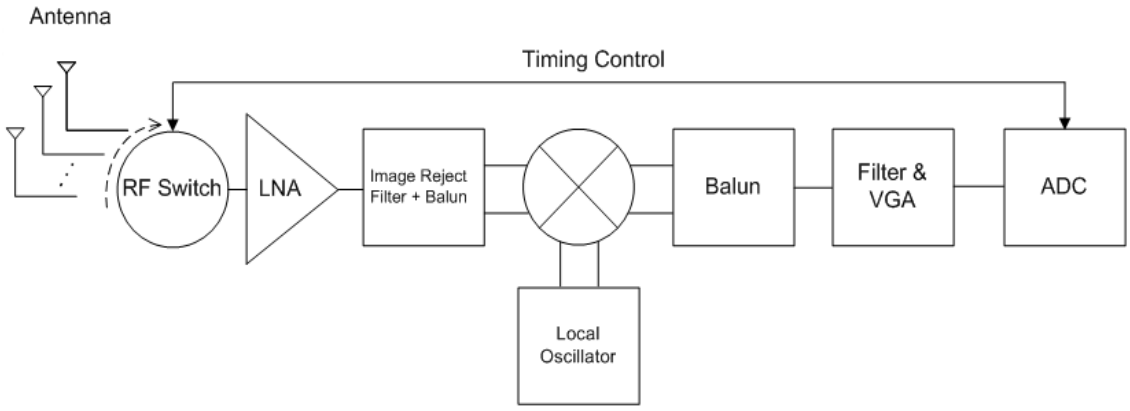

Figure 8.8. Antenna and RF MEMS switch along with the RF front-end system

Figure 8.8 gives a overview of the 60-GHz communication front-end system. The antenna and RF MEMS switch can be found as a part of the whole system. Every block in this system contributes to the typical value of the noise figure (*NF*) used in the link budget analysis in section 1.5. In addition to that, the indoor propagation model is used between two communicating 60-GHz devices. The power loss coefficient value (*N*) is shown in Table 8.5.

Table 8.5. Power loss coefficient values, *N*, for the ITU site-general indoor propagation model.

Frequency	Residential	Office	Commercial
900 MHz	-	33	20
1.2 – 1.3 GHz	-	32	22
1.8 – 2 GHz	28	30	22
4 GHz	-	28	22
5.2 GHz	-	31	-
60 GHz*	-	22	17

*: 60 GHz is assumed to be in the same room